Enhancing Histotripsy Focused Ultrasound Therapy for Treatment of Fibrous Tissues

Yashwanth Nanda Kumar

A dissertation

submitted in partial fulfillment of the

requirements for the degree of

Doctor of Philosophy

University of Washington

2025

Reading Committee:

Adam D. Maxwell, Chair

Michael Bailey

Jonathan T. C. Liu

Program Authorized to Offer Degree:

Mechanical Engineering

University of Washington

Abstract

Enhancing Histotripsy Focused Ultrasound Therapy for Treatment of Fibrous Tissues

Yashwanth Nanda Kumar

Chair of the Supervisory Committee:
Adam D. Maxwell
Department of Urology, University of Washington

Histotripsy is a pulsed focused ultrasound therapy that ablates tissue through the rapid expansion and collapse of nanoscale endogenous bubbles due to cavitation, imparting strain that leads to mechanical disintegration. While histotripsy has been highly effective in treating various kinds of tissues, its efficacy in ablating tough, fibrous tissues—such as those found in benign prostatic hyperplasia and uterine fibroids—is limited. Treating these tissues often requires an impractically high dose, making clinical application challenging.

One reason for inefficacy is inappropriate parameters used in treating fibrous tissue leading to greater memory effects than anticipated. This leads to the repeated growth of bubbles in a single location rather than their formation across multiple locations. This results in inefficient tissue disruption instead of a continuous liquefied lesion. Furthermore, many optimization studies have been conducted in viscoelastic phantom models, such as agarose, which do not adequately mimic the properties of fibrous tissue.

Histotripsy has several modalities, including intrinsic threshold histotripsy, shock scattering histotripsy, and boiling histotripsy, each with distinct ablation mechanisms, making the parameter space for optimization extensive. To address the challenges of treating fibrous tissue, this dissertation focuses on hardware development to enhance histotripsy treatment, creating phantom models that closely mimic fibrous tissue properties, and the identification of alternative parameters that improve the liquefaction of tough fibrous tissue. Additionally, it aims to study bubble mechanics in fibrous tissue-mimicking phantoms to explain the treatment outcomes better and establish quantitative metrics for determining effective doses across different parameters. By optimizing histotripsy for fibrous tissue ablation, this research seeks to expand its clinical applicability and improve treatment efficacy for conditions involving tough, fibrous tissues.

TABLE OF CONTENTS

LIST OF FIGURES

LIST OF TABLES

ACKNOWLEDGEMENTS

I extend my heartfelt gratitude to my advisor, Dr. Adam D. Maxwell, for taking me under his wing and allowing me to grow. His patience and guidance over the years have been invaluable, and I am fortunate to have gained essential skills in the field of ultrasound through my exposure to multiple projects. A sincere thank you to my committee members, Drs. Michael Bailey, George R. Schade, Mike Averkiou, and Jonathan Liu, for their feedback and support throughout this journey.

I am deeply grateful to the Center for Industrial and Medical Ultrasound (CIMU), both past and present members—who have contributed immensely to my learning and development. Special thanks to Drs. Yak-Nam Wang, Wayne Kreider, Tatiana Khokhlova, Vera Khokhlova, Oleg Sapozhnikov, Gilles Thomas, Pavel Rosnitsky, Mohamed Ghanem, and Matt Bruce. I would also like to acknowledge other members of CIMU, including Kaizer Contreras, David Giraud, Stephanie Tottem, Ga Won (Jenny) Kim, Ekaterina Kuznetsova, Elizabeth Lynch and Barbrina Purington. A special thank you to Dr. Thomas Matula, whose guidance in 2019 led me to CIMU. I am also grateful to my mentors Dr. Eli Vlaisavljevich from Virginia Tech for his guidance on my projects, Dr. Inder Makin, who introduced me to CIMU, Dr Charles D. Emery, who gave me my first break at Ulthera and Dr. Bruce Towe, my Master's advisor who introduced me to the world of Ultrasound. Additionally, I want to thank Dr. Stephen Hsu, and Uma Maheshwar Uppara kanuku, from Ulthera (MERZ) who continuously mentored me and encouraged me to pursue a PhD.

To my lab friends, Dr. Minho Song, Pratik Ambekar, and Gerald Lee—thank you for standing by me through the highs and lows. I will always cherish our attempts to form a book club and journal club while managing our lab work. Rob Serafin, Ava Obenaus, Sayem Bin Abdullah and Bishwambhar Sengupta, thank you for making my early days at UW memorable. A special thank you to my graduate advisor, Wanwisa Kisalang, for always helping me stay calm and consistently reassuring me of her support.

Finally, none of this would have been possible without the unwavering support of my family and friends. To my parents, Madhuri Nanda Kumar and Nanda Kumar Balakrishnan, thank you for enabling me to succeed and pursue my dreams despite the hardships we had. To my wife, Swarnima Pandey, thank you for believing in me and standing by my side through this journey. Managing our son, Arjun, along with everything else was no small task, and I am forever indebted to you. I also extend my gratitude to my in-laws, Dr. J.S. Pandey and Manju Pandey, Drs Swapnil and Mayuri Jain Pandey, for stepping in and supporting us when we needed it most. A special mention and thanks to my aunts, Niveditha Sangeneni and her family, Sundara Yadam and her family, who provided unconditional support when I first arrived in the United States.

Thank you to my grandmom Lakshmikanthamma, and to my grandparents in heaven — Balakrishnan Govindaswamy Naidu, Penukonda Venkata Chalapathi, and Penukonda Venkata Sarojamma — for always looking out for me and blessing me.

To my friends who have become family over the years— Ranjani Sampath Kumaran, Sneha Shenoy, Tanay Chafekar, Prabath “Babai” Vemulapalli, Surekha Achanta, Shruti Narayan Reddy, Swetha Varadharajan, Ramya Ramesh and Sridhar Sadasivam, —thank you for standing by our side.

This list is far from complete. To my extended family in India, and to the friends and colleagues from my days at DAV, REC, Arizona State University, Ulthera, and SGSITS — each of you have left a lasting imprint on my life. I am deeply, deeply grateful.

DEDICATION

Dedicated to my family—without whom I would not be where I am today.

CHAPTER 1. INTRODUCTION

This dissertation explores a variety of topics, including the design and fabrication of hardware, the creation of a fibrous tissue-mimicking phantom model, and the identification and systematic comparison of parameters and doses capable of liquefying both fibrous tissue and its phantom mimics. In the following sections, we introduce key concepts related to the use of ultrasound as a therapeutic modality, discuss the clinical conditions relevant to this dissertation, and review the current state of research in the field.

1.1 FOCUSED ULTRASOUND THERAPY

High-Intensity Focused Ultrasound (HIFU) is a non-ionizing modality that directs focused sound waves to a narrow region known as the treatment zone. Within this zone, the therapeutic effects are realized, while the surrounding regions—both before and beyond the focal point—remain relatively unaffected, thereby minimizing collateral damage as shown in Figure 1.1 below. The effects of focused ultrasound can broadly be categorized into two modalities, based on (1) thermal effects and (2) mechanical effects.

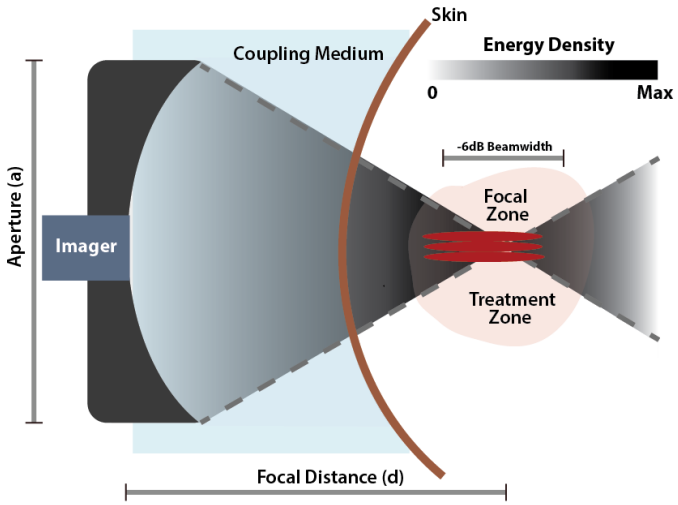

Figure 1.1. Mechanism of Focused ultrasound ablation.

Thermal effects:

HIFU works by the absorption of ultrasound energy, which is then converted into heat within the targeted tissue. This heating raises the temperature rapidly to 60°C – 80°C, and if the temperature is held at above 55°C for 1s or longer, it can lead to protein denaturation and coagulative necrosis, effectively destroying the targeted cells[1]. However, thermal HIFU has several limitations, including imprecise and inconsistent treatment due to perfusion effects, where blood flow dissipates heat and reduces treatment efficacy. It also can cause additional fibrosis, that is antithetical to the outcome expected. Additionally, heat diffusion from the targeted area can cause thermal stress and unintended damage to nearby tissues[1]. Thermal HIFU is typically performed at higher frequencies (>4 MHz), which can lead to increased attenuation, reducing treatment efficiency and sacrificing depth penetration, limiting its effectiveness for deeper tissue targets.

Mechanical effects:

Histotripsy is a non-invasive focused ultrasound modality that mechanically ablates tissue by generating cavitation bubbles[2,3]. The rapid expansion and collapse of these bubbles impart strain on the surrounding tissue, thus disintegrating it to a subcellular level, effectively homogenizing tissue, which can then be reabsorbed by the body with minimal scarring. There is a clear demarcation between treated and untreated areas[4] ensuring precise and targeted ablation [2]. This process is purely mechanical, with minimal thermal effects, as the duty cycle is typically too low compared to traditional thermal HIFU procedures. Currently, multiple modalities of histotripsy have been developed.

(a) **Shock-scattering histotripsy** utilizes multi-cycle pulses ranging from a few microseconds to 25 μs. In this modality, the initial cycles of the pulse train where the peak negative

pressure was closer to the intrinsic threshold, cause nanosized intrinsic nuclei to expand[5]. Once these bubbles reach a critical size, they reflect later parts of the pulse train, effectively inverting polarity. This interaction leads to the formation of a dense bubble cloud that grows toward the transducer face and it's interaction with the tissue causes mechanical disintegration[6].

(b) **Boiling histotripsy** uses millisecond-long pulses (1ms and above) to generate millimeter-sized boiling bubbles[7–9]. This occurs due to the absorption of high-amplitude shocks by tissue, leading to a rapid temperature increase and reduction in the intrinsic threshold required for bubble nucleation. The presence of vapor and dissolved gases causes rectified bubble growth[10,11], and the subsequent interaction with the pulse train results in the formation of shock-scattered clouds that expand toward the transducer. Additionally, secondary boiling bubbles appear distal to the primary boiling bubble, collectively contributing to the liquefaction process. Although these pulses last several milliseconds and involve the formation of a boiling bubble, the process remains predominantly mechanical due to the higher duty cycles (>1%) used.

(c) **Intrinsic threshold histotripsy** uses single-cycle or few-cycle pulses and primarily relies on extremely high peak negative pressures to generate a dense bubble cloud[12,13]. It is often employed to create precise lesions, as shock-scattering histotripsy tends to be more stochastic in nature. Lastly other forms of histotripsy have been explored mainly with pulse durations between shock scattering and boiling histotripsy, (≥100 μs, but less than 800μs)[14,15].

Histotripsy have been demonstrated in ex-vivo and preclinical studies to treat a variety of tissues, such as thrombus, heart, pancreas, brain, liver, kidney, hematomas, abscesses, and prostate [16–27]. While most studies listed here focus on soft tissue, excluding the prostate, several have shown that histotripsy can have tissue selective outcomes, like sparing blood vessels[28], bile ducts[29],

fibrous tissue[30], or induce complete disintegration, in cases such as peyronie's plaque[31], ureteroceles[32], cholangiocarcinoma[33], uterine fibroids[34].

Depending on the mechanical characteristics of tissue, the dose for liquefaction can also vary as shown in the study by Vlaisavljevich et al[35]. The earliest canine prostate studies[36] utilized a 750 kHz frequency, 300 Hz pulse repetition frequency (PRF), and a pulse duration of 3 cycles. Treatment required 270,000 pulses/cm³ for periurethral tissue, which is rich in collagen, while 28,000 pulses/cm³ were used for glandular tissue, demonstrating varied outcomes depending on pulse parameters and dose.

Treatment outcomes were primarily assessed by examining cellular structures using Masson's trichrome stains or Hematoxylin and Eosin (H&E) stains, focusing on cellular signatures such as count and intactness to qualitatively evaluate the effects. However, little is understood about the outcomes when treating fibrous tissue or the extracellular matrix. Currently, no quantitative metrics also exist for evaluating the efficacy of histotripsy treatment in these tissue types.

1.2 CONNECTIVE TISSUE

Connective tissue is a type of tissue primarily responsible for providing strength, flexibility, and structural support, while also assisting in nutrient transport, storing fat, and repairing damaged tissues. It is classified into two main subsets: loose connective tissue and dense connective tissue. Loose connective tissue consists mainly of an extracellular matrix with sparse collagen fibers and large spaces, allowing for flexibility and cushioning. In contrast, dense connective tissue has a higher density of collagen fibers, with some types also incorporating elastin fibers, making it stronger and more resistant to stretching[37,38]. However, excessive growth of fibrous tissue in organs can impair organ function and lead to various health issues which would need medical intervention.

BPH is among several fibrous tissues, such as uterine fibroids[39] and ureteroceles[40], where histotripsy is actively being explored as a potential treatment. While much of the work in this dissertation focuses on the human prostate, specifically addressing benign prostatic hyperplasia as an example tissue, the findings from these studies have broader clinical relevance and may also be applicable to other fibrous tissue conditions such as uterine fibroids, prostate cancer, ureteroceles tendon abnormalities, chronic thrombi, atherosclerosis, certain types of cancer such as sarcoids, and keloid scars.

1.3 Benign Prostatic Hyperplasia

Benign Prostatic Hyperplasia (BPH) is a condition that affects approximately 94 million people worldwide[41] with an annual cost of $1.5 billion[42] in outpatient services and treatment. It is a non-cancerous enlargement of the prostate, characterized by the proliferation of glandular epithelium and stromal cells[43]. The prostate is one of the few organs in men that continues to grow proportionally with age throughout life[44]. While many individuals with BPH experience no significant complications, some develop lower urinary tract symptoms (LUTS), including weak urine stream, urgency, urinary retention (incontinence), increased frequency, and other issues that can significantly impact their quality of life. If left untreated, it can cause additional complications, even ultimately leading to kidney failure.

Several interventions are available for treating benign prostatic hyperplasia (BPH), including pharmacological and surgical options. Pharmacological treatments include alpha blockers, 5-alpha reductase inhibitors, and phosphodiesterase type 5 (PDE5) inhibitors. Alpha blockers relax the smooth muscles associated with the urinary bladder and 5-alpha reductase inhibitors reduce prostate volume by inhibiting synthesis of the more potent dihydrotestosterone[45] to facilitate urinary voiding. However, these interventions are not always effective due to a variety

of factors. One study revealed that approximately 30% of men stop medication within 2 years[46]. Drug-associated side effects such as dizziness, fatigue, and asthenia discourage medication use when the prostate size is too large to be effective[42,47]. While these medications can provide symptom relief, they are generally less effective than surgery for larger prostates. Additionally, they come with side effects such as dizziness, fatigue, and asthenia. Surgical interventions, including simple prostatectomy and transurethral surgery, are often recommended for severe cases or larger prostates[48,49]. However, the presence of comorbidities increases mortality risk, particularly due to anesthesia-related complications. The gold standard procedure, transurethral resection of the prostate (TURP), is effective but carries potential complications such as urethral and bladder outlet narrowing, urinary tract infections (UTIs), erectile dysfunction, and anesthetic risks. Additionally, TURP can lead to TUR syndrome, a condition characterized by low blood sodium levels (hyponatremia) caused by excessive flushing during the procedure[50]. While several minimally invasive therapies are available, focused ultrasound therapy, specifically histotripsy is one alternative approach for treating this condition.

We previously introduced histotripsy precursor studies demonstrating the treatment's efficacy in completely liquefying the canine prostate. Following the success of these studies, a clinical system (Vortx) was developed, and a preclinical trial was conducted to treat benign prostatic hyperplasia (BPH) using the cavitation histotripsy (CH) modality. Preclinical optimization studies once again demonstrated good ablation and safety using high-frequency platelet (PRF) (500 Hz) short pulse (3 cycles) parameters[51] and eventually led to a clinical trial of this treatment[52]. This clinical trial demonstrated the safety of the treatment, reporting minimal adverse events (AE). Some of the AE's reported were urinary retention, bladder spasms, urinary retention, microhematuria and catheter site-related reactions. There was an increase in the International

Prostate Symptom Score (IPSS) from baseline, along with statistically significant changes in ejaculatory function (MSHQ), urinary incontinence (ISI), and chronic pelvic pain symptoms (quality of life scores). However, it did not show objective quantitative improvements in symptoms as measured by the uroflow Q_{max} score, PVR (prostate volume change) and PSA (prostate-specific antigen).

Several factors contributed to the discrepancy in histotripsy outcomes between preclinical canine and clinical human study:

- Anatomical Differences – The human prostate is more fibromuscular[53,54], containing a higher density of collagen and muscular components, whereas the canine prostate is more glandular. As a result, the human prostate exhibits greater toughness compared to canine models, making it more resistant to histotripsy treatment.
- Pulse Repetition Frequency (PRF) – The clinical study parameter used a higher PRF, which has been reported to cause the cavitation memory effect, where bubbles take longer to dissolve and may be re-excited in the same region, reducing treatment efficacy.
- Acoustic Window Limitations – The anatomical positioning of the prostate influenced the available acoustic window, and the deep seated prostate, affected treatment efficiency due to lack of ultrasonic power.[52]

Based on these results, it is evident that the parameters used in the preclinical study were ineffective for the human prostate. Additionally, to overcome acoustic window limitations, a transrectal approach will be explored which will include a transducer redesign. Given the vast parameter space across different modalities, there is a significant opportunity to explore a broader range of parameters, which will be examined in this dissertation.

Additionally, some of the commonly used phantoms in ultrasound histotripsy research, such as agarose, polyacrylamide, and alginate standalone phantoms, are viscoelastic but do not adequately represent the fibromuscular structures of BPH or its response to treatment. While agarose phantoms can be stiff, they lack toughness, making them brittle and prone to fracturing. Their low fracture energy, as indicated by a small area under the stress-strain curve, causes them to break under relatively low strain compared to tougher materials. As a result, many optimization experiments and bubble mechanics studies[55–62] conducted using red blood cell (RBC) agarose phantoms do not accurately replicate the effects of sonication on tissue-mimicking phantoms specifically designed for fibrous tissues. We will explore potential alternative phantoms that can closely mimic human fibrous tissue.

Visual feedback was primarily provided by B-mode ultrasound, where cavitation clouds appeared hyperechoic, aiding in focal placement. Once treatment was complete, fully liquefied volumes appeared hypoechoic; however, this served only as a qualitative metric. Shear wave elastography (SWE), on the other hand, offers a quantitative assessment of tissue stiffness. It utilizes an acoustic radiation force push pulse to generate shear waves, which propagate perpendicular to the ultrasound beam. The shear wave velocities, tracked at the pixel level, are then used to compute the shear modulus map and the elastic modulus, providing a stiffness measurement of the tissue. In this dissertation we will explore SWE extensively as a more robust quantitative metric to assess treatment completion and measure outcomes.

1.4 ORGANIZATION OF THE DISSERTATION

In Chapter 2, we evaluate performance, efficiency and operational limits of some of the most commonly used transducer types to determine the most suitable options for further development. Chapter 3 details the design and fabrication of a clinically used histotripsy

transducer, along with methodologies for developing a transrectal histotripsy transducer. Chapter 4 focuses on the development of a fibrous tissue-mimicking model, its mechanical and acoustic characterization, and a comparison with ex vivo human prostate tissue. An initial alternative parameter set is introduced, along with the identification of doses required to liquefy both the phantom and tissue using the clinical and alternative parameter sets.

In Chapter 5, the results from Chapter 4 are applied to *ex vivo* human prostate treatments, where three sets of parameters across two modalities are tested. Quantitative metrics for dose completion are established, and an automated lesion quantification algorithm is introduced and validated. Chapter 6 presents a systematic comparison of five parameters across different doses in a fibrous tissue-mimicking double-network phantom, with outcome evaluation using shear wave elastography and phase-contrast microscopy. A bubble dynamics study provides further insight into treatment outcomes. Additionally, we explore the novel use of an open-top light sheet microscope to estimate true treatment volumes. Finally, Chapter 7 summarizes the findings of this dissertation and discusses potential future research directions.

CHAPTER 2. EVALUATION OF PIEZOELECTRIC TRANSDUCER VIBRATION AND MECHANICAL FAILURE UNDER HIGH POWER PULSED OUTPUT

2.1 INTRODUCTION

Histotripsy transducers produce extremely high ultrasound intensities at the focal point, often exceeding 30 kW/cm² I_{SPPA}, while maintaining a duty cycle of less than 2%[63]. There are three primary modalities of histotripsy: intrinsic threshold histotripsy, shock scattering histotripsy, and boiling histotripsy. Intrinsic threshold and Shock scattering histotripsy utilizes transducers with an f# between 0.6-0.9, Boiling histotripsy involves transducers with an f# between 0.75-1.

Each histotripsy modality requires transducers specifically designed for their application, considering factors such as geometry, element positioning, f-number (focal distance, aperture), element area, and ceramic type. However, some transducers are designed to be versatile, capable of performing more than one type of histotripsy[20,64]. The different types currently being used are single element lensed [65,66], single element bare ceramic,[8] multi element spherically focused by a lens[51,64,67] and piezo composites [68], as shown in Figure 2.1a.

In addition to these design considerations, transducer performance and durability are influenced by driving voltage, attenuation through media (including lens effects), affecting its overall efficiency. High-power histotripsy transducers are prone to several types of failures, including mechanical, electrical, and material-related defects. Mechanical failures often present as cracks at locations of maximum stress or delamination due to thermal effects caused by heating of the polymer within the matching layer. Electrical failures can occur due to damage to the driving electronics caused by the high power drawn by the transducer, and loss of poling resulting from the electrical breakdown and excessive thermal heating of piezoelectric materials[69]. Additionally,

material and manufacturing defects, such as impurities in the crystal structure, can further degrade transducer performance.

This study aims to evaluate three different transducer configurations (Figure 2.1b) by characterizing their power limits, comparing their output capabilities for histotripsy applications, and measuring their overall efficiency before breakdown. A comprehensive understanding of the mechanical and electrical limitations of histotripsy transducers is essential for enhancing their durability and performance. By assessing various configurations and identifying failure points, more robust and efficient transducers can be developed for optimized histotripsy applications.

Furthermore, this knowledge is critical for developing alternative therapy delivery approaches, such as transrectal applications, which require miniaturization. Miniaturized transducers must endure extreme driving powers to generate higher pressures, making durability and efficiency essential factors in their design.

2.2 METHODS

2.2.1 *Hardware*

Three groups of transducers with each of the 3 configurations were tested (n=4 per group). Group 1 consisted of flat PZT-8 piezoceramic discs, procured from Steiner and Martins (Davenport, FL, USA), coupled to a rapid-prototyped elliptical focused lens made from Accura 60 (3D Systems, Rock Hill, SC, USA), a transparent polycarbonate-like material (cured) with a speed of sound (C) of 2540 m/s and density (ρ) of 1210 kg/m³. A quarter-wavelength matching layer composed of aluminum oxide and epoxy (INF-212, West System, Gougeon Brothers, Bay City, MI, USA) with C = 2905.1 m/s and ρ = 2151.1 kg/m³, was used to bond the PZT elements to the lens. Group 2 consisted of bare spherically curved focused PZT ceramic elements housed in a structure made from Accura 60. Both Group 1 and Group 2 transducers were air-backed, with

individual RG-174 coaxial cables (~2 m in length) soldered directly to each element. The cables were routed through the back housing, and all potential openings were sealed with marine epoxy glue to ensure waterproofing. Group 3 consisted of a commercially provided spherically focused piezocomposite from Imasonic (Voray-sur-l'Ognon, France), which was made of multiple piezoceramic micro-rods embedded in a proprietary polymer matrix made of resin.

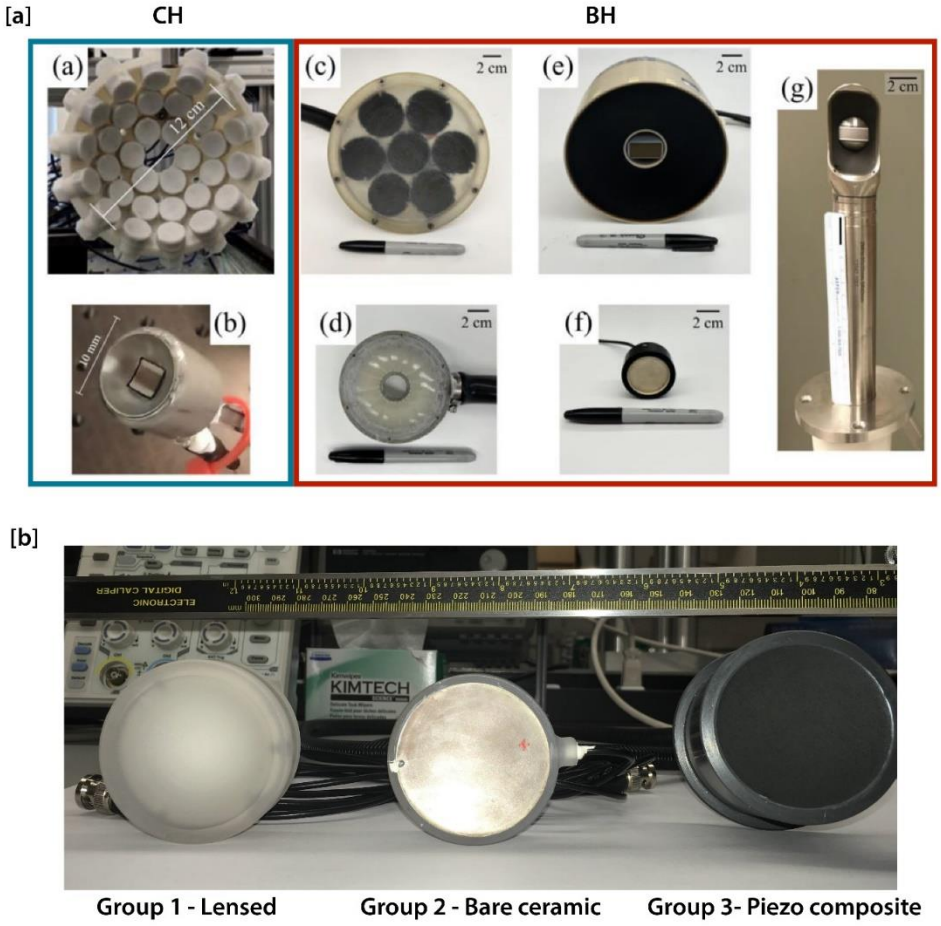

Figure 2.1. (a) Different types of transducers currently being used for histotripsy therapy delivery (b) Transducers used in this study

(Image source: Figure 2.1 (a) from Williams et al [69]) subfigures [a](a) and [a] (b) are from [56,70] respectively and are licensed under a creative commons attribution license (CC by 4.0).

Table 2.1. Transducer configuration used in this study.

	Group 1: Lensed	**Group 2: Bare ceramic**	**Group 3: Piezocomposite**
Focal length(mm)	45	45	50
Aperture (mm)	90	90	100
Matched Impedance (Ω)	2	5	2
Driving Frequency (MHz)	1	1.095	1

Each transducer had a center frequency of 1MHz, focal length of 90-100mm and aperture = 45-50mm. The impedances of the transducers were measured using an impedance analyzer (AIM4300, Array Solutions, Sunnyvale, TX, USA). They were electrically matched using lowpass Low-Hi matching network to 2-5 Ω per element, operating at 1-1.095 MHz. The description of the builds are summarized in Table 2.1 for easy reference. The system was driven by a custom-built Class D amplifier, powered by a high-voltage source (TDK Lambda GENH600-1.3) and controlled using an FPGA board (Altera DE0-Nano, Terasic Technology, Dover, DE, USA).

2.2.2 *Holography*

Transient source holograms were captured by placing the transducers in a tank filled with degassed and deionized water and mounting them on a 3-axis positioner, as shown in Figure 2.2. A PVDF-based hydrophone, HGL-0200 (ONDA Corporation, Sunnyvale, CA, USA), was used to capture the pressure waveforms at a distance of 40 mm proximal to the pressure maximum. The transducers were excited by a tone burst signal of 10 cycles, with a center frequency close to 1 MHz. Each scan covered an aperture of 52.5 mm with a step size of 0.75 mm. The hydrophone was connected to a preamplifier and to a digitizer (GaGe, Dynamic Signals LLC, Lockport, IL, USA) to record all waveforms. The transient holograms were backpropagated using a Rayleigh-integral kernel based on the technique described in [71] to reconstruct the normal velocity on the transducer surface.

One processing consideration was that the bowl diameter was chosen to exceed the true diameter to avoid slope discontinuities.

The surface velocities were integrated to obtain the normal displacement, and a 2D strain state was calculated based on two measurements: (1) The average normal strain in thickness mode was determined by dividing the observed displacement by the element thickness (2.1 mm) and multiplying by a factor of 2, as the elements were air-backed. (2) Shear strain was calculated from the displacement gradients across the surface using the 'imgradient' function and the 'Sobel' method. From these two strain components, the maximum principal strain was estimated and plotted as a function of time. The final strain map was normalized with reference to a single value for comparison within individual groups. Holography aimed to identify locations of high mechanical strain, where failures were most likely to occur. A second set of holograms were taken of the transducers that had failure to identify potential regions of failure.

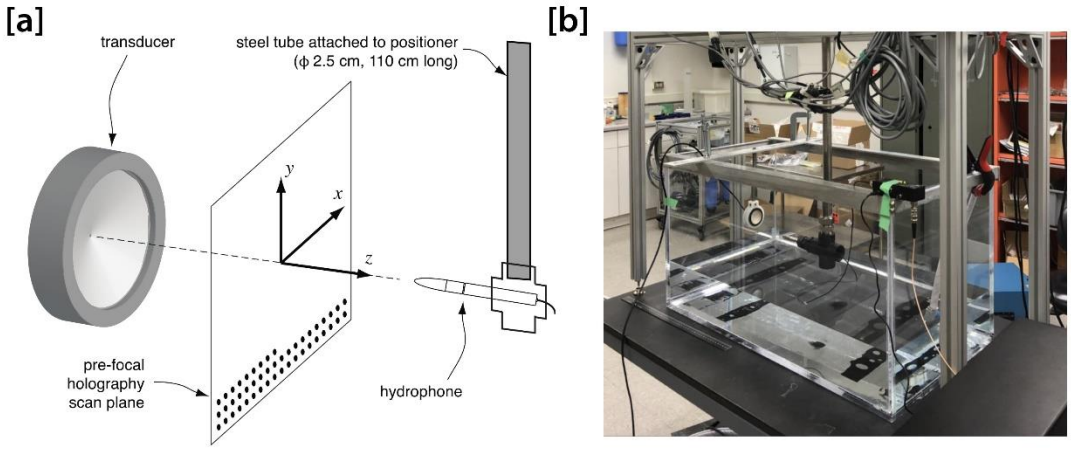

Figure 2.2. (a) Illustration showing holography acquisition process and (b) showing the actual tank setup.

2.2.3 *Computed Tomography scan:*

All transducers were scanned using a Feinfocus FXE x-ray machine coupled with a Perkin Elmer detector from YXLON (Essener Bogen Hamburg Germany). A total of 2880 images were collected at a resolution of 200µm. The purpose of these scans was to evaluate the transducers structurally for potential pre-existing defects. A second set of scans were taken after the treatment for transducers that failed, to determine if there was a mechanical failure that can be identified by CT.

2.2.4 *Acoustic Radiation Force Balance (ARFB) testing:*

An acoustic absorber, kept soaked (>1 week) in water, was suspended in a tank filled with degassed and deionized water and coupled to a Sartorius Entris 6231 weighing scale (Göttingen, Germany) using a rapid-prototyped fixture. Each transducer was submerged in the tank and secured in place using optical rods (Thorlabs, Newton, NJ), positioned a few centimeters above the absorber. The focus of the transducer was aligned within the absorber to measure the radiation force, recorded as a change in weight. The scale was interfaced to a PC through an RS232 communication port to record the values directly onto the system. This measured force (in weight) was then converted to acoustic power (W) using a conversion factor, which was roughly calculated to be 14.5 mW per mg of weight [72] measured on the scale, assuming water temperature to be around 20ºC. The whole setup is shown in Figure 2.3.

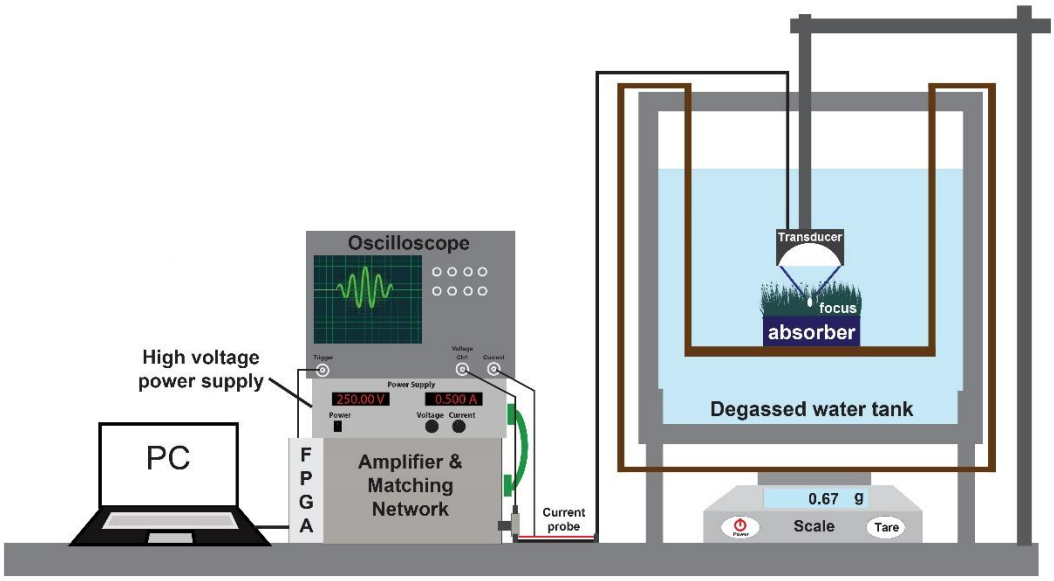

Figure 2.3. Acoustic force balance setup along with the driving electronics.

The transducer was driven by a custom Class D amplifier with up to 16 channels bridged to deliver increased power. Pulse parameters were programmed via an FPGA board, which was interfaced with a PC for control. To measure electrical power, a high-power voltage probe (B&K Precision PR 200B, Yorba Linda, CA, USA) was connected in parallel to the transducer after the matching network interface. Additionally, a current probe AP015 (Teledyne LeCroy, Chestnut Ridge, NY) was placed around the RG-174 cable supplying power to the transducer. Both probes were connected to a LeCroy 9304 CM oscilloscope, which interfaced with a PC to record voltage and pressure waveforms, synchronized with the scale's acoustic power measurements.

The transducers were driven with a pulse repetition frequency (PRF) of 100 Hz, using 10-cycle pulses at a baseline input DC voltage of 100V for approximately 10 seconds. During this period, baseline scale measurements and voltage and current waveforms were recorded. From these measurements, pulse-averaged acoustic power (W) and pulse-averaged electrical power (W) were calculated. The input DC voltage was then systematically increased in 10V increments, and

the excitation was applied for 1 minute while continuously recording electrical and acoustic measurements across systems. After each test, a baseline recording was taken again to detect any deviations from the original values, indicating potential changes in transducer properties. This process continued until the maximum amplifier voltage of 400 Vdc was reached or until an irreversible change occurred, indicated by a drop in acoustic power, signaling transducer failure.

Both the pulse averaged electrical power and pulse averaged acoustic power values were converted into intensities by dividing by the transducer surface area. The efficiency of the transducer was calculated using the equation below.

$$Efficiency = \frac{Pulse\ averaged\ acoustic\ power(W)}{Pulse\ averaged\ electrical\ power(W)} \qquad (2.1)$$

2.3 RESULTS

2.3.1 *Holography and Computed Tomography*

Qualitative strain map assessments revealed that in bare ceramic transducers, lateral waves converged at the center, forming distinct rings of higher strain. Some lateral waves were also observed in the lensed transducer. In terms of vibration pattern uniformity, bare ceramic transducers showed the highest variability, followed by the lensed transducer. Piezocomposite transducers exhibited high uniformity, though strain maps also highlighted solder joints as points of stress and concentric focusing of elements. Pre-experiment scans showed no visible cracks or surface damage. However, a correlation between strain maps and CT maps indicated that solder point regions (Fig. 2.4) in all transducer groups exhibited a higher strain component, suggesting localized mechanical stress in these areas.

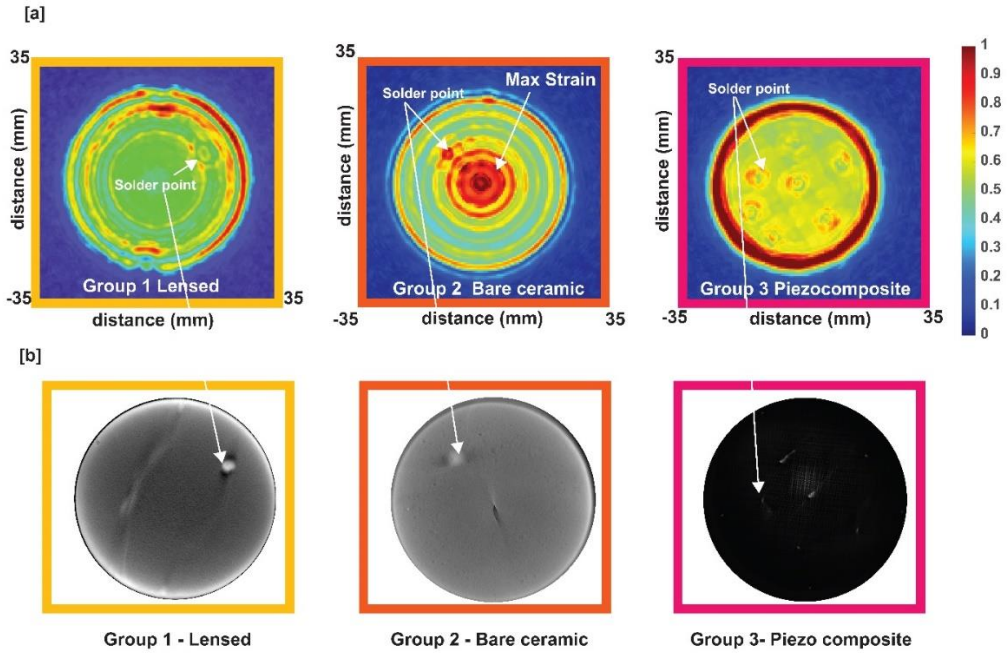

Figure 2.4. (a) Holography scans showing strain pattern across the surface of the transducer and corresponding Computed tomography scan.

2.3.2 *Acoustic Radiation Force Balance (ARFB) testing*

The maximum pulse-averaged electric power per unit transducer surface area (intensity) was highest for Group 3 at 592.23 ± 20.88 W/cm², followed by Group 1 at 535.29 ± 11.83 W/cm². Group 2 reached a maximum intensity of 352.61 ± 34.81 W/cm² (Figure 2.5b), at which point it experienced a drop in acoustic power and confirmed by the change in the baseline measurements post failure. Group 3 transducers generated the highest acoustic output per unit transducer surface area, reaching 527.80 ± 3.56 W/cm² at an efficiency of 89.20 ± 2.89%. The lensed transducer (Group 1) produced 270.91 ± 17.79 W/cm² at an efficiency of 50.58 ± 2.49%. For both Group 1 and Group 3, these values were obtained at the maximum available input source voltage of 400V (Figure 2.5).

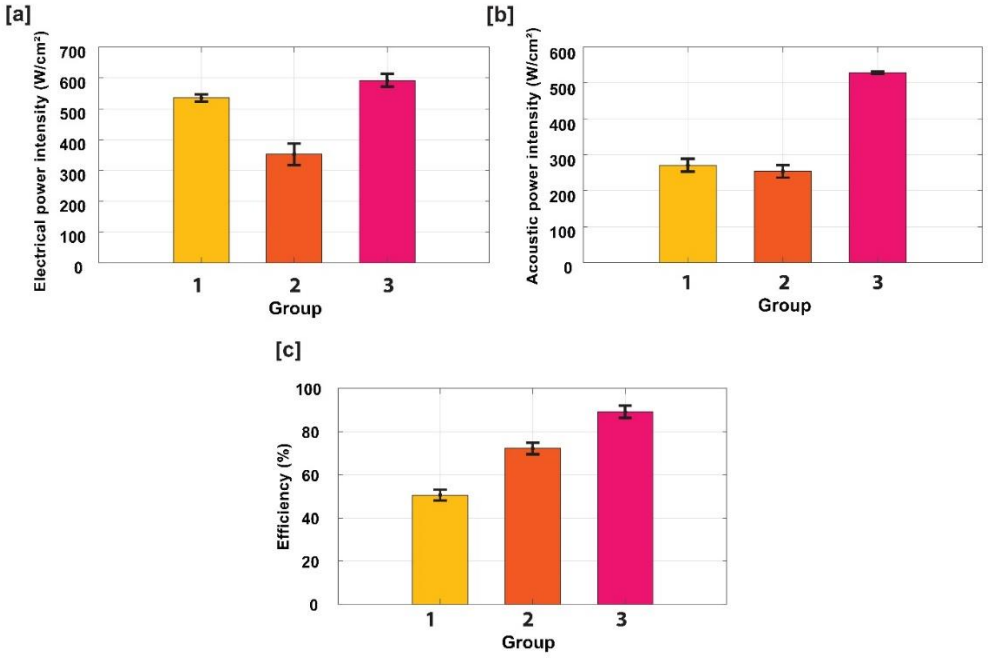

Figure 2.5. Pulse averaged electric power intensity, pulse averaged acoustic power intensity and efficiency for each group

The bare ceramic transducers (Group 2) generated a maximum acoustic output of 254.04 ± 17.61 W/cm² at an efficiency of 72.22 ± 2.66% before experiencing failure. The failure occurred at different voltages and times for the four different samples. The efficiency maps over time are shown in Figure 2.6, where for Group 2, the efficiency initially measured 72.22 ± 2.66% but later dropped to 33.6 ± 13.2%.

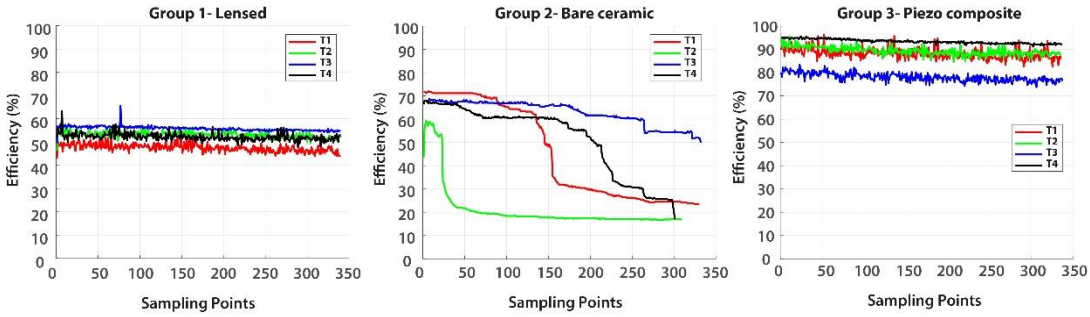

Figure 2.6. Efficiency measurements tracked along the entire duration (1 Minute) of the treatment for every group

Post-treatment CT scans did not reveal any mechanical failure at the scanned resolution. However, a second set of holograms for Group 2 transducers showed strain maps that differed from earlier scans (Figure 2.7). Unlike the initial scans, there was no congregation of lateral waves toward the center. Instead, a more diffuse strain pattern was observed throughout the transducer. An impedance measurement of the Group 2 transducers revealed a median drop of -24% (IQR: -42% to -11%) compared to pre-experiment measurements.

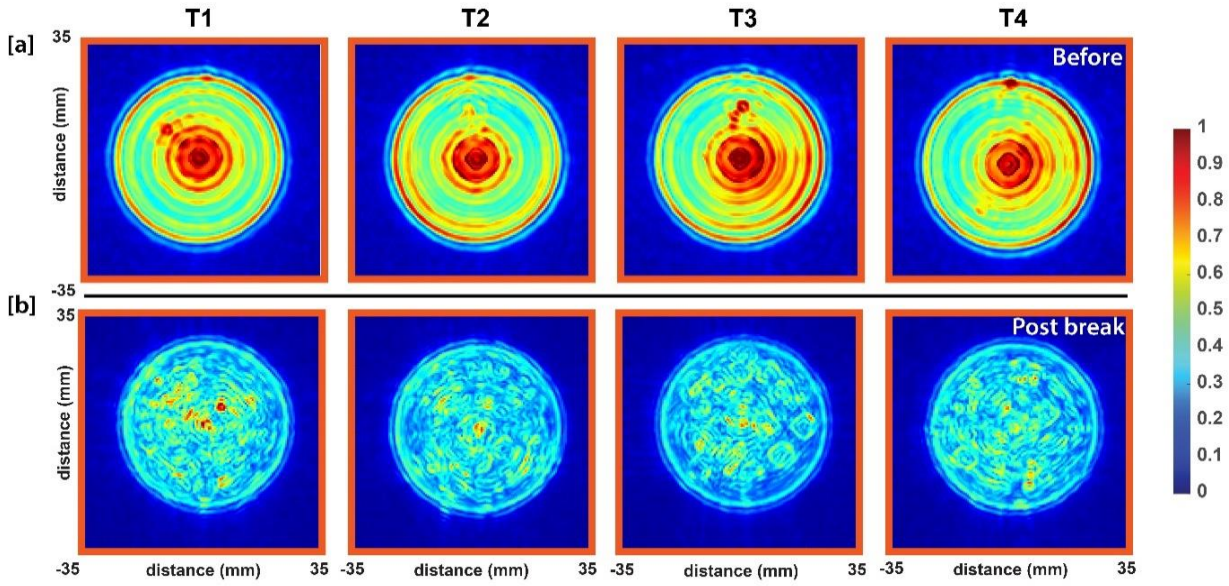

Figure 2.7. Holography scan of Group 2 transducers (T1 to T4) before and after the study protocol.

2.4 Discussion and Conclusion

In this study we tested three commonly used transducer types for histotripsy, (i) Spherically focused flat piezoceramic transducers with a rapid prototyped lens (ii) naturally focused- bare ceramic, (iii) Piezocomposite transducers that were procured from a manufacturer. The performance was evaluated by holographic scans and acoustic power measurements. Additionally, CT scans taken of the transducer to correlate with the holographic scan to determine the potential mechanisms of failure, one which could be both electrical or mechanical. As such, this study aimed to better understanding the ways these transducers behave at high driving power necessary for histotripsy applications and potentially influence the ways we can design better, efficient and durable transducers in the future.

Both Group 1 lensed transducers and Group 3 piezocomposites were driven to the maximum available electrical power 8.3±0.15 kW and 9.4±0.57 kW without experiencing

mechanical or electrical failure. In contrast, Group 2 transducers underwent an irreversible change at relatively low electrical power levels (5.5±0.65 kW). Post-treatment scans revealed that, unlike pre-treatment conditions, lateral waves no longer converged centrally, instead forming a diffuse strain distribution across the transducer surface. This shift, combined with a drop in acoustic power and a reduction in efficiency from 72.22 ± 2.66% to 33.6 ± 13.2%, indicating irreversible transducer failure.

While failure was expected at maximum strain points, the diffuse strain pattern indicates potential internal structural degradation, possibly occurring across the thickness mode, which was not visible in CT scans. This highlights the value of holography in detecting such anomalous transducer behavior. Further investigation is needed to precisely determine the pattern of failure and assess whether it was strictly mechanical or involved additional electrical factors.

The lower efficiency of Group 1 lensed transducers compared to Group 2 and Group 3 was expected, as the lens material has attenuation similar to a comparable tested material, Formlabs Clear. This material has a sound speed and density comparable to Accura 60, with an attenuation value of approximately 2.92 dB/MHz·cm.[73]. However, despite this attenuation, Group 1 transducers were driven at higher power levels than Group 2 bare ceramic transducers, which had a similar surface area. The matching layer helps distribute mechanical stress across the transducer surface by preventing lateral wave buildup and high-amplitude reverberation. It also protects against mechanical damage at higher pressures and the lens improves isolation from water, reducing degradation over time. Additionally, Group 3 transducers demonstrated efficiency values consistent with manufacturer specifications. However, due to amplifier limitations, which restricted the ability to drive piezocomposite and lensed transducers at even higher power levels,

we were unable to determine which of these two configurations can produce the greatest power density without failure.

Holography is a valuable tool for analyzing transducer vibration patterns and detecting structural changes that may not be visible on CT scans. When used alongside other characterization methods, it enhances the ability to predict transducer performance and identify potential failure modes. However, certain assumptions were made in this study. There may be in-plane normal strains and nonuniform displacements through the element thickness, which could influence the holography output. Additionally, the curved transducer surface may have introduced distortions in holographic reconstruction.

High strain values were observed near the edges of each transducer, particularly in Group 3, which is possibly an anomaly occurring at the boundary between the element and its housing. Furthermore, the holographic reconstruction of Group 1 transducers may scale differently due to the added lens in front of the PZT, affecting direct comparisons across groups. While post-treatment scans of Group 2 were conducted, additional work, including holographic analysis of other undamaged transducers, would provide a more comprehensive comparison.

Bare ceramic transducers, while highly efficient, failed at relatively low driving power, making them less suitable for applications requiring high-pressure generation. However, they may still be useful for applications such as endocavity probes[74] or studies involving small animal models[65,75]. Piezocomposite transducers were the most efficient and did not experience catastrophic failure, making them the ideal candidate for histotripsy applications. However, their higher cost and specialized manufacturing requirements limit accessibility and slow down the rapid iterative design process. Lensed transducers present a promising alternative, balancing cost and manufacturability. While they experience efficiency losses due to attenuation through the lens,

this issue can be mitigated by selecting lens materials with better acoustic properties and using thin lenses.

CHAPTER 3. APPROACHES TO THERAPY DELIVERY: DEVELOPMENT OF TRANSPERINEAL AND TRANSRECTAL TRANSDUCER FOR THE TREATMENT OF BENIGN PROSTATIC HYPERPLASIA.

3.1 INTRODUCTION

Benign Prostatic Hyperplasia (BPH) is a clinical condition that affects older men, where prostate enlargement leads to urethral constriction and causes lower urinary tract symptoms, impacting quality of life. While transurethral resection of the prostate (TURP) remains the gold standard treatment, it is associated with complications such as erectile dysfunction, hematuria, and urethral strictures. Additionally, TURP is not recommended for patients with comorbidities[76,77]. Histotripsy, a focused ultrasound modality, uses cavitation bubbles to mechanically disintegrate tissue using cavitation bubbles that strain the tissue due to the expansion and collapse of these bubbles[2]. A preclinical study evaluating its efficacy in canine models via a transperineal approach successfully treated BPH [51]. However, clinical studies did not yield the same objective improvements[52].

In this chapter, we will discuss the design and development process of a clinical transducer, using reported transducer characterization values to create a reference model for optimization studies. Additionally, we will explore the design and development of a miniaturized transducer capable of delivering histotripsy treatments transrectally. This approach aims to overcome the challenges associated with the limited acoustic window available in transabdominal and transperineal methods[51]. Also, a transrectal approach is the most feasible method for delivering boiling histotripsy (BH) at higher frequencies, as a transperineal approach would present

significant challenges for BH application. A single-element 2 MHz boiling histotripsy (BH) transducer has already been developed by other members of the lab [66] and has successfully treated ex vivo prostate tissue. Our goal is to develop a multi-element version capable of performing both cavitation cloud and boiling histotripsy treatments.

3.2 METHODS

3.2.1 *Design Specifications*

Transperineal transducer: The motivation for the design of this transducer was based on the need to mimic the original transducer used in the prior clinical study by Roberts et al [51,52]. This transducer would provide a baseline for previously observed effects related to treatment of fibrous BPH tissue. The transducer was intended to have the following requirements:

- An operating frequency of 700 kHz, with a 11cm focal distance and an aperture of 13cm.
- The beam width should be close to 3mm x 10mm (lateral x axial).
- A central opening to coaxially host an imaging transducer, which differed from the transrectal imaging approach of the original clinical transducer.
- Sufficient gain (>30) to create cavitation clouds at the focus [64,78,79]

Transrectal transducer: The requirements for this transducer were as follows:

- A maximum width of 35mm and height 30-35mm in height including a coaxial mounted imager to successfully use in in-vivo canine studies
- A focal distance of at least 4cm to sufficiently target the prostate.
- Sufficient gain (>30) for cavitation at the focus [64,78,79]
- Ability to perform both cavitation and boiling histotripsy regimes

3.2.2 *Transducer fabrication*

Transperineal transducer: A Rayleigh-Sommerfeld simulation was conducted using MATLAB (MathWorks, Natick, MA) to achieve beam parameters close to 3 × 3 × 10 mm. Various factors, including the number of elements and their spacing, were optimized to ensure sufficient gain (about 45 with the configuration chosen). The final design consisted of 18 elements, with 6 elements arranged in the inner ring and 12 in the outer ring, leaving a ~4 × 3 cm inner cutout to accommodate an imaging transducer, as shown in Figure 3.1. Each element, made of PZT-8 and procured from APC international (Mackeyville, PA, USA), had a diameter of 27 mm and a thickness of 0.078 mm. The simulation resulted in a beam with a Full Width at Half Maximum (FWHM) of 2.5 × 2.5 × 14 mm. The transducer housing, including the outer lid and elliptical lens (with minor radius = 0.0564 m and major radius = 0.0694 m), was designed in SolidWorks (Waltham, MA, USA) and manufactured using rapid prototyping by Protolabs (Plymouth, MN, USA). KLM modeling, based on the methods developed by Maxwell et al.[9], was instrumental in identifying efficient ceramic and matching layer combinations. This approach helped optimize material selection by evaluating readily available materials, ensuring both performance efficiency and practical manufacturability. The lens material used, Accura 60 (3D Systems, Rock Hill, SC, USA), which is a transparent polycarbonate-like material(cured) with a speed of sound (C) of 2540 m/s and density (ρ) of 1210 kg/m³.

To optimize acoustic impedance matching, the impedance of both the PZT elements and the lens was calculated. The matching layer impedance was selected close to 7.25 MRayls. A quarter-wavelength matching layer composite (thickness ~0.54 mm) was fabricated from a mixture of TAP Marine epoxy medium (C = 2393 m/s, ρ = 1130 kg/m³) and tungsten powder filler (C = 5200 m/s, ρ = 19,240 kg/m³) with a weight fraction of 0.18 and 0.82, respectively. The final

measured net effective parameters of this composite were C = 1500 m/s and ρ = 4849 kg/m³. The elements were air-backed and individual RG-174 coaxial cables about 2m in length were soldered directly onto them and the cables were routed through the back housing. All potential openings were filled with marine epoxy glue to make it waterproof. The central opening was designed such that it could accommodate an imaging transducer ATL P 4-2 connected to a Verasonics system (V-1 Ultrasound Acquisition Platform, Verasonics Inc., Kirkland, WA, USA) or an M5Sc ultrasound imaging probe of a GE Vivid E9 4D ultrasound system (GE Healthcare, Chicago, IL, USA). The final assembly is shown in Figure 3.2.

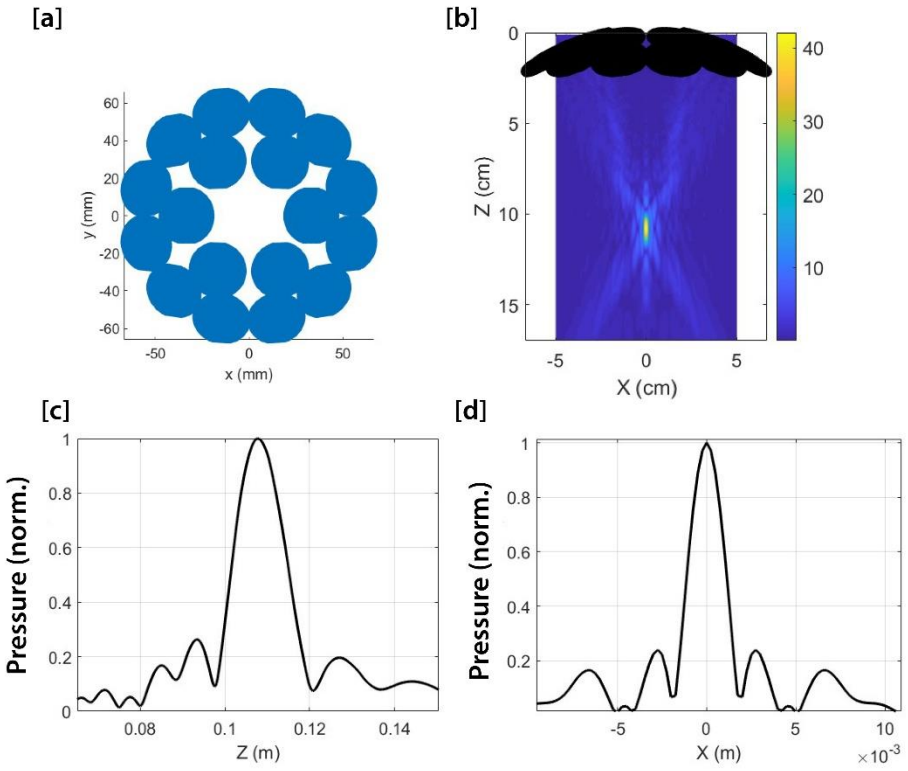

Figure 3.1. Transperineal transducer mimicking the clinical study transducer. (b) Rayleigh Sommerfeld simulation displaying maximum gain achieved at the focus. Simulated beam profiles (c) axial and (d) lateral

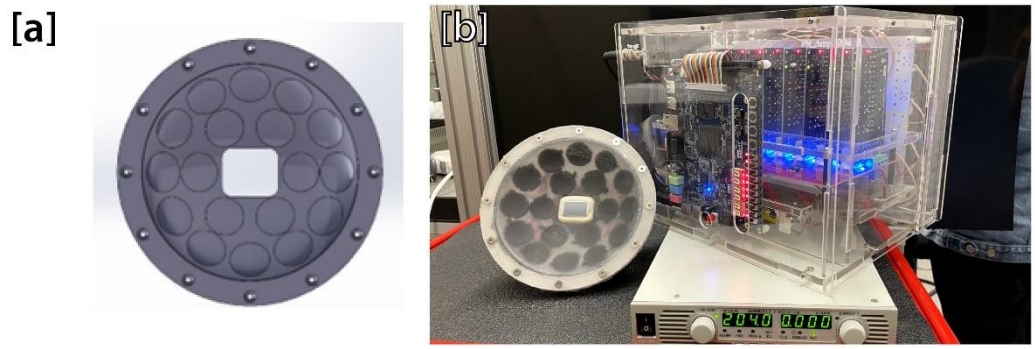

Figure 3.2. : (a) Solidworks model of the lens and (b) Assembled transducer, along with the DC input source and a class D amplifier with an FPGA board for pulse programming.

.

Transrectal transducer design: Two different designs (builds) were explored for administering histotripsy transrectally. The focal distance was set to 4cm, and Rayleigh Sommerfeld simulations were performed to identify the element size and arrangement so as to maximize the gain (37.5 in build 1, and 64 for build 2) and is shown in Figure 3.3. PZT-8 elements with a resonant frequency of 3MHz and the following dimensions 16x26mm and 0.7mm in thickness were procured from (Steiner and Martins, Davenport, FL, USA) and cut to size using a dicing saw.

Build 1 used a 4 PZT -8 elements cut to 10mm by 21mm with an overall footprint 35mm W x 37mm D x 55mm L which included an endocavity biplane transducer (E14CL4b, 14–4 MHz, 3–60 mm focal range) connected to a BK 3000 medical imaging platform (BK Medical, Quickborn, Germany).

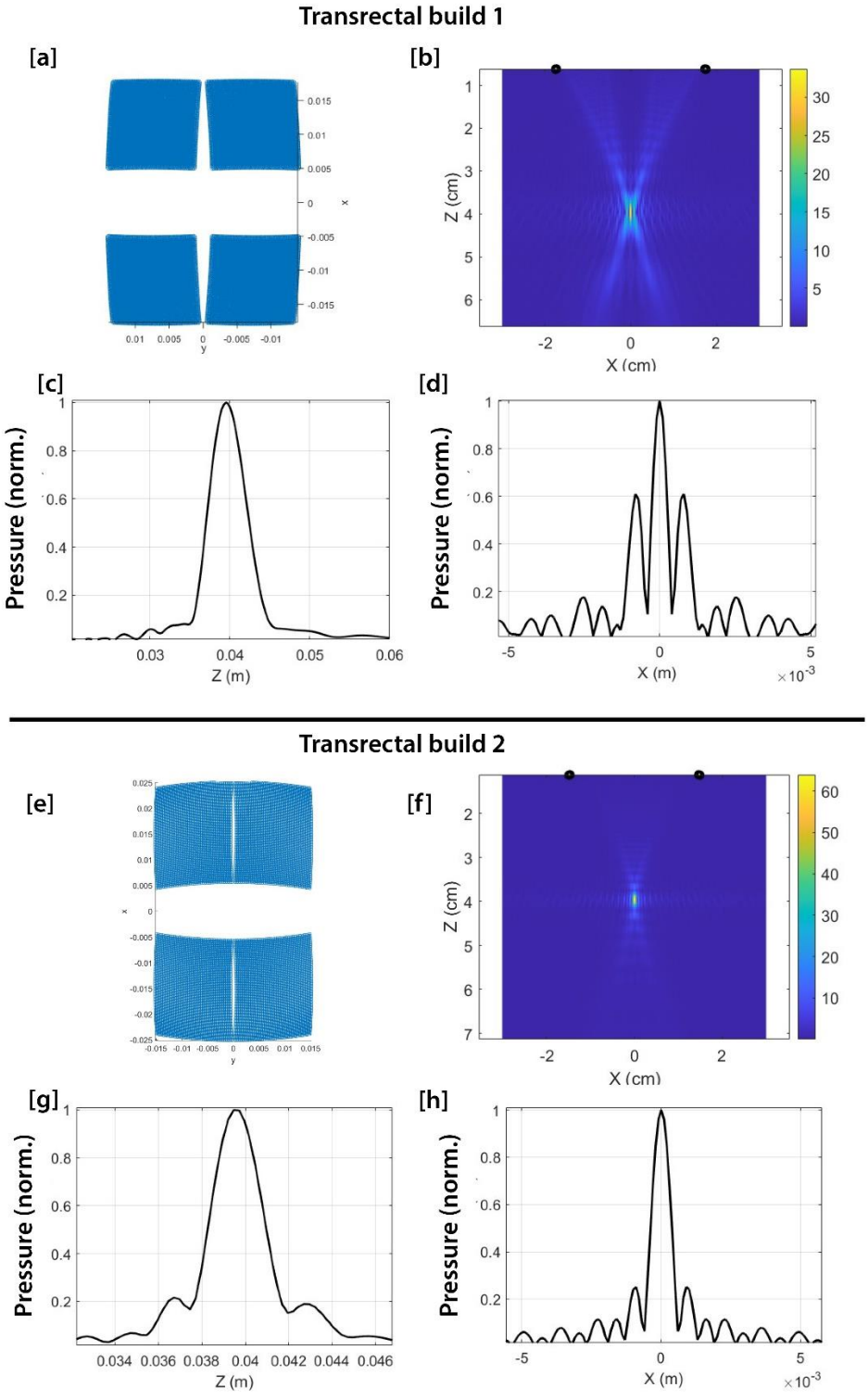

Figure 3.3. (a) and (e) show the element aperture (b) and (f) Rayleigh Sommerfeld simulation displaying maximum gain achieved at the focus for the two different builds. Simulated beam profiles (c),(g) axial and (g),(h) lateral.

For build 2 the PZT -8 elements were sized to 15mm by 21.5mm with an overall transducer footprint 33mm W x 27mm D x 74mm L. A custom 128 element imager from Vermon (Tours, France) was embedded with the therapy head. The imager has a target distance of 35mm operating at a center frequency of 7.5MHz.

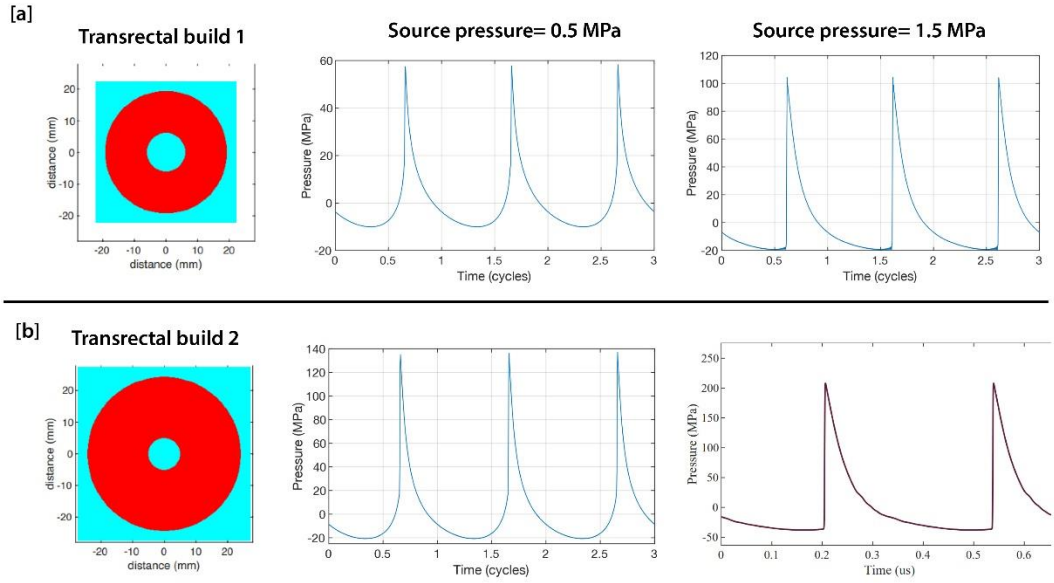

Figure 3.4. Nonlinear simulation using an equivalent source model showing shock formation at different source pressures indicated.

Additional nonlinear acoustic field simulations (Figure 3.4) were conducted for two axisymmetric equivalent sources (f-numbers 0.96 and 0.74) representing these two builds using the "WAPE" model in the HIFU beam software [80].

To select an appropriate matching layer and lens, various material combinations were tested in a single-element design to determine whether sufficient pressures could be generated. One combination tested included Ceramic-Like Advanced HighTemp (PerFORM) (C = 3510 m/s, $\rho = 1610$ kg/m³) and Borosilicate Glass (C = 5640 m/s, $\rho = 2240$ kg/m³, thickness = 0.5 mm).

Ultimately, the lens material selected for the transducer was SOMOS Watershed XC 11122 polymer from DSM and rapid prototyped from Protolabs (Plymouth, MN, USA) with a sound speed of 2397.8 m/s and density of 1120 kg/m³. A quarter-wavelength matching layer (~250 μm), composed of 66% aluminum oxide and 34% epoxy (INF-212, West System, Gougeon Brothers, Bay City, MI, USA), with C = 2905.1 m/s and ρ = 2151.1 kg/m³, was used to bond the PZT elements to the lens.

The elements were air-backed, and individual RG-174 coaxial cables (approximately 2 m in length) were soldered directly to each element. Provisions were made on the front face of the transducer to accommodate catheters for transporting water to the transducer's surface. Additionally, grooves were incorporated on the handle to hold O-rings, securing a transparent film or condom to retain water and ensure a clear ultrasound propagation path. The SolidWorks model and the full assembly are shown in Figure 3.5.

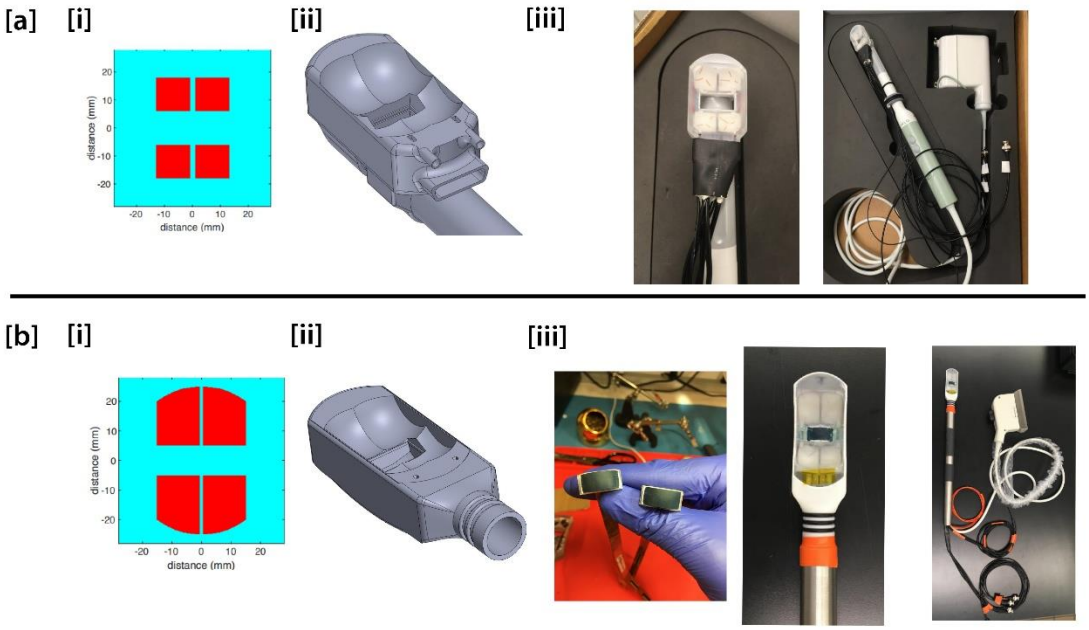

Figure 3.5. (a) (i) Element area, spacing and aperture for build 1 (ii) Solidworks render (iii) Fully assembled transducer with coaxial endocavity probe, water lines (b) (i) Element area, spacing and aperture for build 2 (ii) Solidworks render (iii) L-R Custom imaging transducers, transducer active area, full transducer assembly with coaxial imager and water lines.

3.2.3 *Transducer characterization*

The impedances of the transducers were measured using an impedance analyzer (AIM4300, Array Solutions, Sunnyvale, TX, USA). The transperineal transducer was impedance-matched using lowpass L-bridge matching network to 20 Ω per element, operating at 700 kHz. The transrectal transducers were matched to either 10 Ω or 5 Ω, operating at 3 or 3.175 MHz, to maximize voltage gain. The system was driven by a custom-built Class D amplifier, powered by a high-voltage source (TDK Lambda GENH600-1.3) and controlled using an FPGA board (Altera DE0-Nano, Terasic Technology, Dover, DE, USA).

Transducer characterization was performed by placing the transducers in a tank filled with degassed and deionized water, mounted on a 3-axis positioner.For linear beam width measurements, beam profiles were recorded at low pressures using an Onda HGL-0085 hydrophone (ONDA Corporation, Sunnyvale, CA, USA) connected to an AG2020 preamplifier or a needle hydrophone (Precision Acoustics, Dorset, UK) with a 75 μm active area, to estimate the -6 dB beamwidth. For focal pressure measurements, a fiber optic hydrophone (FOPH2000, RP Acoustics, Stuttgart, Germany) was used, to measure the focal pressure with increasing applied input DC voltage.

Focal pressure corrections were applied to both positive (P+) and negative (P-) pressure measurements obtained with the FOPH. These corrections were necessary when the beamwidth in the nonlinear regime was smaller than the fiber diameter, to mitigate averaging effects and prevent underreporting of pressure values. This was done based on the correction method mentioned in the following articles [81,82].

The performance of the transducers was tested by driving them with the amplifier using 3-15 cycles at 500-1000 Hz PRF with the aim to create cavitation clouds in degassed water and 1.5% agarose phantom. The phantom was prepared by combining 1.5% by weight UltraPureTM Agarose (Thermo Fisher Scientific, Waltham, MA, USA) and de-ionized water in a beaker and heating for 6 mins. Once the liquid-cooled below 40ºC, it was transferred into a cast container for gelation.

3.3 RESULTS

3.3.1 *Transducer output characteristics:*

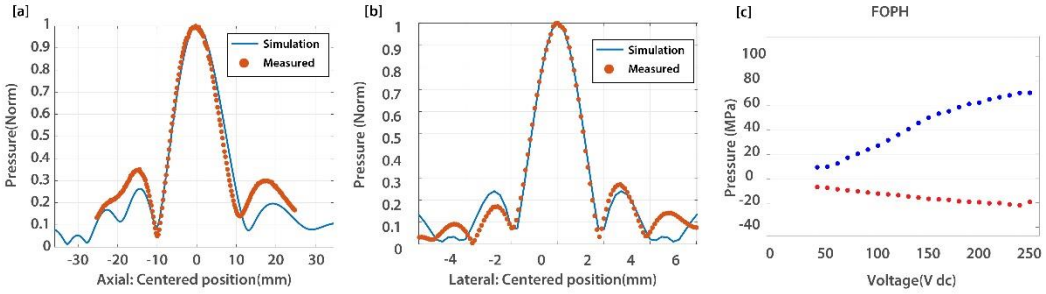

Figure 3.6. (a) Focal pressure measurements up until cavitation was observed at the tip. (b) Axial and (c) Lateral beam scans, overlapped with Rayleigh Sommerfeld beam simulation results for the transperineal transducer.

Transperineal transducer: The linear beamwidth scans (Figure 3.6(a), 3.6(b) were well-aligned with the simulation, with the -6dB measurements of 13.1 × 2.2 × 2.2 mm (axial (a) × lateral (l) × lateral (l)). The beamwidth volume (V) was calculated using the formula

$$V = \left(\frac{\pi}{6}\right).a * l^2 \qquad (3.2)$$

resulting in a volume of 33.19 mm³, which was within 30% of the reported beamwidth volume from the clinical study.

Focal pressure waveforms show the transducer producing P+ close to 70MPa and P- of 20MPa, before cavitation appeared at the tip of the hydrophone, precluding measurements at higher output levels.

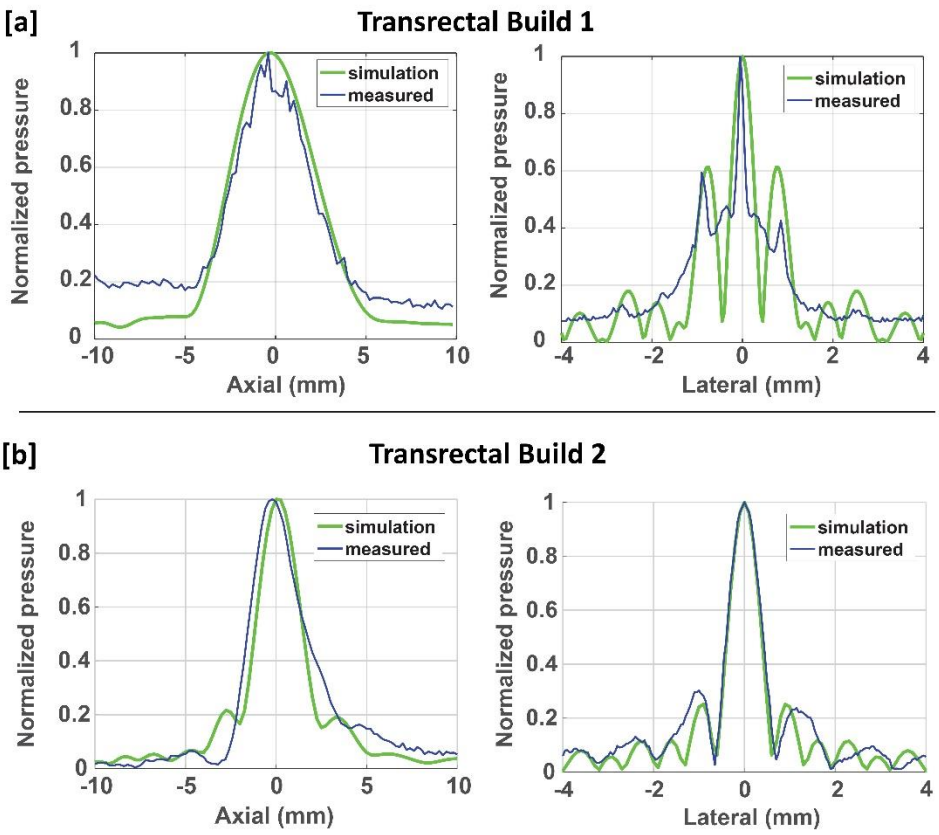

Figure 3.7. Axial and lateral beam scans, overlapped with Rayleigh Sommerfeld beam simulation results for the transrectal transducer builds.

Transrectal transducer: The linear beamwidth scans for both builds showed agreement with the simulation (Figure 3.7). The -6 dB measurements for Build 1 were approximately 4.6 mm axial, 0.5 mm lateral, and 1.8 mm lateral including sidelobes. Build 2 exhibited minimal sidelobes, consistent with both the simulation and measured values, with beamwidth measurements of approximately 2.7 mm axial and 0.8 mm lateral.

Nonlinear simulations of Build 1 and Build 2 (Figure 3.8(a)) showed that the transducers generated focal pressures exceeding P+ 100 MPa and P- 20 MPa for Build 1, and P+ 170 MPa and P- 20 MPa for Build 2, at different source pressures. However, FOPH measurements recorded at a

maximum input source voltage of 350 V showed P+ 47 MPa and P- 15 MPa for Build 1, and P+ 59.5 MPa and P- 19.1 MPa for Build 2.

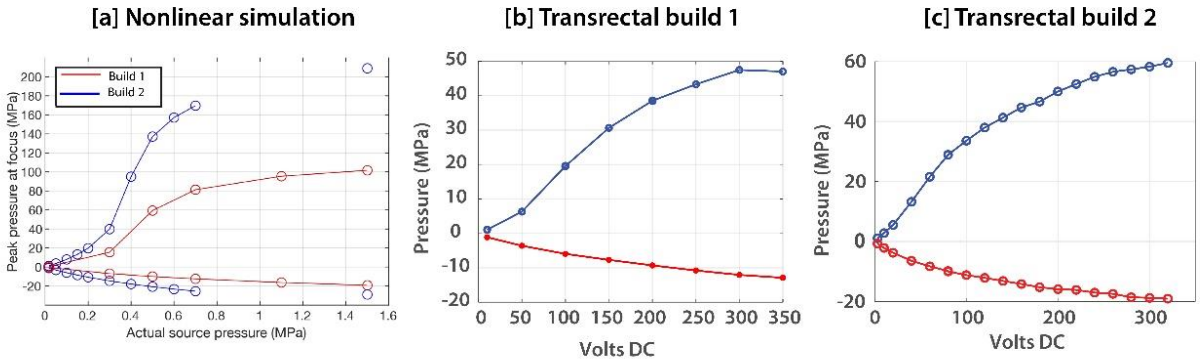

Figure 3.8. (a)Nonlinear simulation of the focal pressures and measured values (b) and (c) from FOPH

Build 2 was chosen for further analysis by analyzing the pressure waveforms beyond 80v of input source voltage. The waveforms appeared to be shocked (Figure 3.9(a)) and the time to boil estimated by the weak shock theory [83] was found to be <5ms at the pressure amplitudes produced by the transducer here.

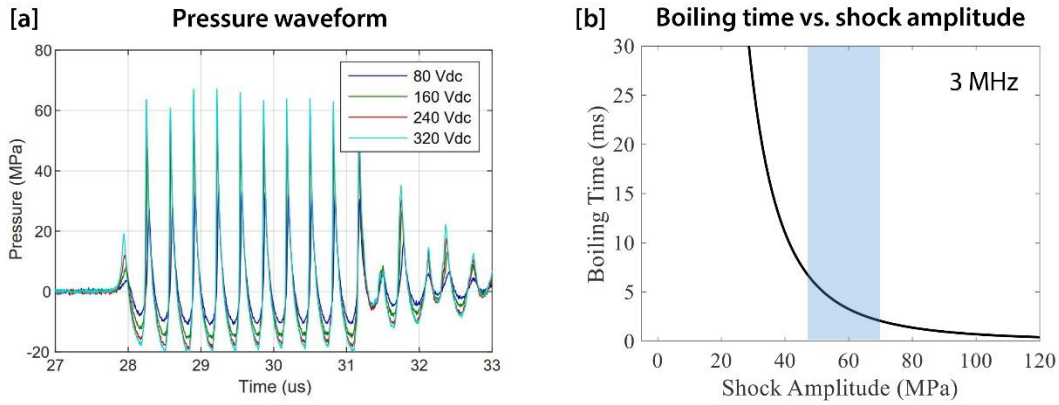

Figure 3.9. (a) Measured pressure waveforms at different input source voltages. (b) Time taken for boiling to occur at the focus at various shock amplitudes.

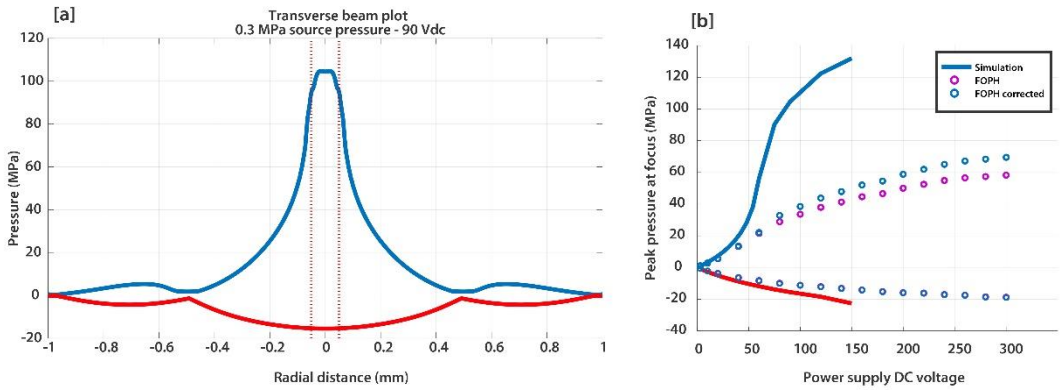

Figure 3.10. (a) Simulated transverse beamwidth for build 2 following shock formation with the red lines indicating the FOPH fiber tip width. (b) The corrections applied to the measured focal pressures are shown along with the non-corrected values and the simulated values for build 2.

Further corrections were applied to the FOPH measurements of Build 2, based on beamwidth simulations (Figure 3.10(a)), to account for averaging errors at the fiber tip. These corrections were necessary because the beam area was smaller than the fiber tip, leading to potential underestimation of the measured pressure values. A correction of up to 20% was applied to the P+ pressures measured, while the P- pressure correction was minimal and almost insignificant (Figure 3.10(b)).

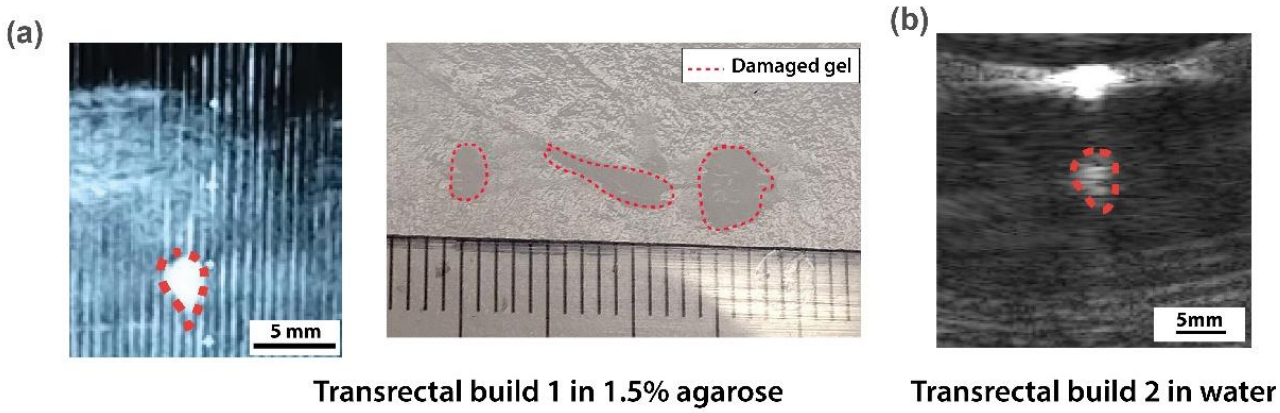

Figure 3.11. (a) Hyperechoic cavitation cloud seen in 1.5% agarose phantom on B-mode and (b) the gel visibly showing damage when treated with build 1 transrectal prototype (b) Hyperechoic clouds created in degassed water as seen on B-mode, generated by the inbuilt imager, when sonicating with the build 2 transducer.

The Build 1 transducer, operating at 3 MHz, 1000 Hz PRF, and a pulse duration of 15 cycles, successfully generated cavitation within a 1% agarose phantom, as indicated by the presence of a hyperechoic cloud on the B-mode image. A liquid pocket was also formed, as shown in Figure 3.11(b). Similarly, Build 2, operating at 3.175 MHz, 1000 Hz PRF, and a pulse duration of 15 cycles, generated cavitation clouds in degassed water, as seen in Figure 3.11(c).

3.4 Discussion and Conclusion.

Both the transperineal and transrectal transducers were developed based on the principles of rapid prototyping of ultrasound transducers [78], which significantly accelerated development and reduced costs for iterative design. The 18-element transperineal transducer closely matched the beamwidth volume of the clinical transducer[51] and performed as expected. It was successfully used

for benchtop experiments in tissue-mimicking phantoms and ex vivo benign prostatic hyperplasia tissue, which will be discussed in the following chapters.

Two different transrectal transducer designs were evaluated for cavitation cloud and boiling histotripsy treatments. Build 1 consistently generated cavitation clouds in both water and 1.5% agarose, while Build 2 successfully generated cavitation in water but failed in 1.5% agarose due to electrical limitations. This failure could be attributed to two primary factors. First, the poor linearity of the transducer at higher voltages, where an increase in input voltage did not necessarily translate to a proportional increase in output, potentially leading to heating effects instead. Second, design constraints on the transducer elements and amplifier limited the total output power that could be delivered. The mismatch between the simulation and the measured focal pressure also indicated more work that needs to be done in this space. A frequency of 3 MHz was chosen to maximize pressure gain for successfully generating cavitation clouds and operating in boiling histotripsy regimes. However, factors such as an increase in frequency, a higher F-number, and reduced linearity at higher amplitudes could result in bubbles with a smaller radius and also produce less dense clouds,[56,84] potentially limiting their ability to interact with a narrow shock focus. Consequently, this may reduce the shock scattering effect, diminishing the overall efficacy of cavitation treatments.

Further testing involved operating the transducers predominantly in boiling histotripsy regimes during in-vivo studies. However, both builds failed during the process owing to delamination and structural and amplifier failure, ultimately halting further testing. To improve performance, future design optimizations could involve reducing the element area by half, which would increase the net effective impedance, leading to better impedance matching and improved voltage gain to drive

the transducer more efficiently. Additionally, different matching layer combinations can be explored to avoid delamination issues.

The challenges associated with miniaturizing transducers for transrectal delivery remain a significant hurdle. This study represents a step toward developing histotripsy transducers that can overcome the limitations of transperineal and transabdominal approaches. The ultimate goal is to refine this technique to make prostate debulking more successful, addressing challenges that have persisted in current treatment methods.

CHAPTER 4. DEVELOPMENT OF TOUGH HYDROGEL PHANTOMS TO MIMIC FIBROUS TISSUE FOR FOCUSED ULTRASOUND THERAPIES

4.1 INTRODUCTION

Tissue mimicking phantoms are an important tool for the development, optimization, and performance testing of therapeutic ultrasound techniques [85,86]. These phantoms provide a cost-effective medium for direct feedback on optimal treatment strategies in a low-risk environment before continuing to pre-clinical in-vivo models and clinical trials. Tissue phantoms have been characterized and utilized in approximating both soft (*e.g.,* blood and liver) and hard (*e.g.,* whole bone and dental) tissue for therapeutic ultrasound [87]. Soft-tissue phantoms include agarose, gelatin, polyacrylamide, polyurethane and oil-based gels with hard tissue phantoms being epoxy or acrylic plastic, among others [88–94]. Certain nuanced phantoms made of polyvinyl alcohol, polyacrylamide or acrylic base and embedded with thermal markers like bovine serum albumin (BSA)[95], red blood cells (RBC)[96], thermochromic additives(inks, powders or liquid crystals)[97–99] have also been developed. In some cases, they offer reversibility of thermal HIFU effects for reuse, thus fast tracking the testing process [100].

Though there is a broad variety of phantoms available for mimicking tissues with different stiffnesses suitable for evaluating HIFU ultrasound therapies, for e.g., agarose based phantoms [35], there are few material substitutes which adequately represent fibrous tissue with high inherent toughness, a quality that may be especially important in mechanical cavitation-based ultrasound therapies. A typical stress-strain curve for a fibrous tissue is nonlinear with large deformations at lower loads, following which the material becomes stiffer at increasing loads and becomes linear at higher loads [101]. Fibrous tissue in general are very compliant and undergo large strains with load thus leading to an overall larger area under the stress-strain curve and greater total energy input to produce mechanical failure [101]. Some hybrid gel phantoms like Polyacrylamide-alginate also possess a larger area under the stress strain curve [102] and this attribute is referred to as inherent toughness or fracture toughness of the material.

Inherent toughness is found in many pathologic tissues, including benign prostatic hyperplasia (BPH), wherein the tissue can form fibromuscular (collagenous) components that toughen the tissue and play a role in producing BPH symptoms [103]. Ultrasound techniques have been developed to treat BPH, such as histotripsy, which is a non-invasive therapy that uses short, high-pressure ultrasound pulses to mechanically fractionate tissue[21]. Investigators found early success in treating *in-vivo* canine prostates using high pulse repetition frequencies (PRF), demonstrating histotripsy as a promising treatment modality for BPH [30,36,51,104]. However, during a subsequent clinical trial, histotripsy did not produce objective improvements in clinical symptoms or changes in prostatic volume [105]. A potential reason for the reduced efficacy is due to the differences in mechanical characteristics between non-BPH canine (as tested in the prior pre-clinical models) and human BPH tissue [106]. In contrast to non-BPH canine prostate, tough fibromuscular stromal hyperplasia tends to predominate in human BPH making it more resistant

to the effects of histotripsy [107]. This reasoning is further supported by multiple prior studies which have shown that fibrous tissues are, in general, more resistant to histotripsy-induced tissue damage [107],[108–111]. These biological differences highlight the importance of having preclinical models (*i.e.,* tissue phantoms + animal model) that adequately represent the target tissue.

The heterogeneous nature of prostatic tissue provides a unique challenge in creating an appropriate tissue phantom. Despite being considered a soft tissue, fibromuscular stromal hyperplasia (collagen remodeling) wherein fibrosis leads to an increase in elastic modulus due to collagen and elastin cross-linking [112] leave the prostate resistant to the treatment effects of histotripsy [113]. Traditionally, soft agarose, alginate and polyacrylamide gels have been used as tissue mimics for prostate. Although agarose gels can represent soft glandular elements of prostatic tissue [114]; they have low toughness and tend to break down easily at low stresses, and existing literature suggests that the fracture toughness for polyacrylamide and alginate gels are small and do not capture the mechanical characteristics of average and tough BPH tissue. Additionally, the phantom must be optically transparent to visualize histotripsy cavitation on high-speed photography. Thus, an ideal phantom would be one that:

1) Can approximate the mechanical and acoustic properties of fibrous tissues.

2) Is optically transparent.

3) Can be easily reformulated to approximate a range of tissue properties (*e.g.,* soft, average, and tough BPH tissue with stiffnesses ranging from 15-100 kPa).

4) Responds to histotripsy in a similar manner to tissue in terms of the fracture mechanics and the nucleation and evolution of bubble clouds that cause mechanical damage.

5) Allows histotripsy lesions to be easily detected (to measure lesion volume and size) and analyzed (in ability to cause complete ablation) for optimization of treatment parameters.

6) Is relatively simple and inexpensive to prepare [55].

Such a phantom would be valuable not only for investigation of BPH, but also for other inherently tough, treatment resistant, diseased tissues, including uterine fibroids, fibrous tumors such as cholangiocarcinoma and pancreatic ductal adenocarcinoma, and plaques caused by Peyronie's disease or atherosclerosis [115–118]. Like BPH, advancements in therapeutic ultrasound for these diseases will depend on identifying effective treatment strategies in accurate preclinical models.

Hydrogels are often used as scaffolds for tissue engineering and to model extracellular matrices for biological studies[119]. However, traditional hydrogels are limited by their poor mechanical properties and, as a result, double network hydrogel phantoms (with both covalent and ionic crosslinking) were created which have suitable elastic moduli and high mechanical strength [120].

In this paper, we fabricate and characterize the mechanical and acoustic properties of a novel three-dimensional polyacrylamide/alginate phantom hydrogel that can better represent tough fibrous tissue such as that found in patients with BPH. The phantoms were compared against ex-vivo human prostate tissue from BPH patients to determine their similarity in response to histotripsy. To evaluate treatment efficacy, B-mode ultrasound was employed along with shear wave elastography (SWE), and changes in cavitation bubble dynamics as seen under high-speed camera photography. In addition, a method utilizing phase contrast microscopy was introduced to visualize damage to the phantom structure. This work establishes the feasibility of using these phantoms to evaluate the efficacy of treatment parameters in ablating ex-vivo fibrous tissue.

4.2 MATERIALS AND METHODS

4.2.1 *Polyacrylamide Alginate Gel Preparation*

A modified polyacrylamide alginate hybrid gel formulation based on prior work reported by [102] was developed to mimic pathologic tough fibrous tissues. Several gel ratios (polyacrylamide: alginate) were explored and 3 weight ratios (85:15,90:10,95:5 w/w) were chosen to represent different tissue stiffness (15-100 kPa) and toughness[102]. The overall volume of the water in the gel was held constant at 86% by weight across all gel samples. Liquid acrylamide (40% solution by weight) was used for preparing the phantom. The photoinitiator ammonium persulphate (APS), the covalent crosslinker N,N-methylenebisacrylamide (MBAA) and the crosslinking accelerator N,N,N',N'- tetramethylethylenediamine (TEMED) were kept at ratios of 0.0017, 0.0006, 0.0028 respectively to the weight of acrylamide. As an additional step, 10 mL of 1% by weight of MBAA and APS were prepared to safely titrate the components into the mixing beaker, due to the minute quantities required for weighing and the resolution of the balance. The weights of these 3 components were in addition to the sum total. The recipe is summarized in Table 4.2. For the other gel ratios, the alginate weight was increased, and the ratio of acrylamide reduced accordingly, and the quantity of the other components adjusted. All required chemical ingredients were sourced from Sigma Aldrich Inc (St. Louis, Montana, USA).

Table 4.2. Sample weight and volume measurements for preparing 200 g of 85:15 Polyacrylamide Alginate gel.

Chemical Name	**Wt% from recipe**	**Final Quantities**
Deionized Water	86%	107.03 mL
Acrylamide	11.9%	59.5 mL
Alginate	2.1%	4.2 g
Sum	**100%**	
AP	0.17% of Acrylamide	From 1% AP - 4.046 mL
MBAA	0.06% of Acrylamide	From 1% MBAA - 1.428 mL
TEMED	0.28% of Acrylamide	0.086 mL

1M solution of $CaSO_4.2H_2O$ is prepared by mixing 136.14 g in 1 liter of deionized water

In a fume hood, the preparation was started by adding the required volume of deionized water into a beaker. Sodium alginate was weighed using a weigh scale (PB153-S, Mettler Toledo, Columbus, Ohio, USA) and transferred into the beaker which was then placed on a magnetic stirrer and mixed at an RPM of 300 until the alginate was completely dissolved to form a homogeneous solution. During this process, an ultrasonic processor (Vibra-Cell - VCX 500, Sonics & Materials Inc., Newtown, Connecticut, USA) was used at 25% amplitude to sonicate the sample for ~60 seconds to assist with the dissolution process for every 2-3 minutes of stirring. The required volume of acrylamide was then measured using a graduated beaker and poured into the alginate solution and stirred. The beaker was then covered with perforated aluminum foil and placed in a degassing chamber for an hour at 25 inHg vacuum. Alongside this, prepared 1% (by weight) solutions of MBAA and APS were also degassed along with an additional 500-1000 mL of deionized water. After degassing, the contents of AP, MBAA and TEMED were pipetted to the beaker and mixed using a magnetic stirrer at a low RPM of 60. The contents were transferred into multiple molding beakers to set the thickness of each gel to 20mm and a diameter of 30mm.

The gel was cured by UV light in a curing chamber (Form curing oven, Formlabs, Somerville Massachusetts, USA) at 60^{o}C for 3 hours. Post cure, the gel samples were removed from the molding beakers and thoroughly rinsed under running water to remove any residual chemicals. Further curing was performed by submerging the UV-cured gel in a crosslinking solution. Calcium sulfate dihydrate $CaSO_4.2H_2O$, the ionic crosslinker for the alginate, was prepared by mixing the powder into degassed and deionized water. A 1M solution was chosen to ensure enough calcium ions were present for complete diffusion with extended soaking times to enable complete crosslinking based on the work by [121].

The concentration proposed can be used for curing all the gel compositions, as it contains an excess of calcium ions. The gel phantoms were suspended in the solution for a period of 48 hours preferably in a desiccator held at 25 in Hg vacuum or in a sealed container. The time (t) was calculated based on the formula from [121]

$$t = \left(\frac{4}{\pi}\right).\frac{H^2}{D} \quad (4.3)$$

where H is the half thickness of the gel, D = 10^-5 cm^2 is the diffusion coefficient. Equation 4.3 determined the minimum time for submersion to be around 11.3 hours, however the samples were submerged for 48 hours to ensure complete diffusion. After 48 hours, the optically transparent gels were removed from the beaker, rinsed, and stored in an airtight container. Over the recorded storage period of 11 days, the maximum change in weight was found to be <7%. Storage of the gels in water is not recommended, as submergence led to swelling secondary to absorption. The summarized flowchart outlining the steps to pour the gel is shown in Figure 4.1.

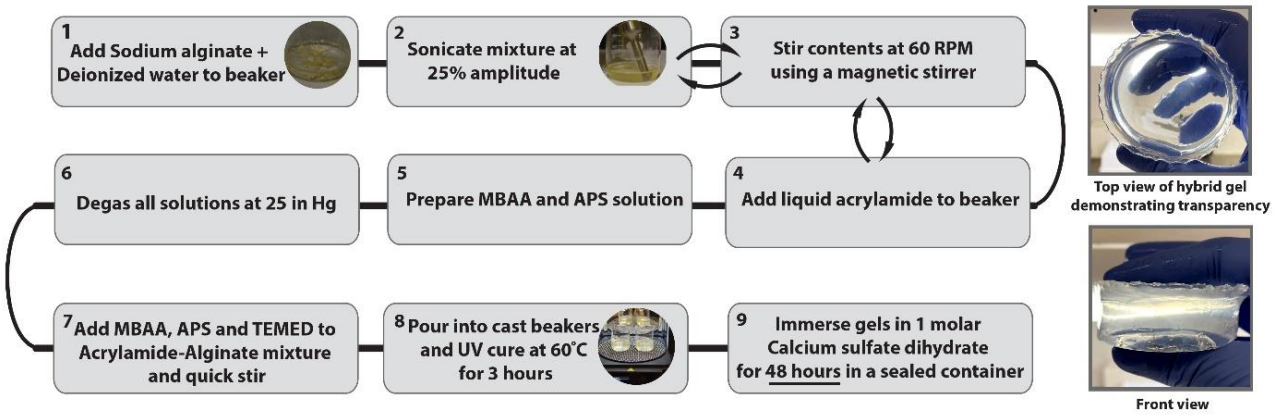

Figure 4.1. Flowchart summarizing the preparation for Polyacrylamide/Alginate hybrid gel phantoms. The righthand images show the appearance of the final hydrogel, which has high optical transparency.

Two additional points are worth noting regarding gel formulation. First, initial preparations mixed the ionic crosslinker calcium sulfate dihydrate directly into the liquid gel solution prior to UV cure, but this should be avoided as it led to a very heterogeneous gel phantom whose stiffness varied widely across the sample and made it opaque. Second, calcium chloride cannot be substituted as a crosslinker despite its high solubility and fast cross linking [122] [123]. It's use led to a stiff outer layer with the interior of the phantom at a lower stiffness and also made the phantom opaque.

4.2.2 *Agarose Gel Preparation*

Agarose gel was prepared as a 1.5% weight/volume combination of agarose and deionized water by mixing 3 g of agarose to 225 mL of water in a beaker and heated to a boiling temperature for 6 minutes. This yields a final volume equal to 200mL which constitutes 1.5% weight/volume gel. The gel was slowly cooled by placing it in a desiccator kept at 25 inHg to prevent any dissolution of air back into the gel, and once the mixture reached a temperature below 45ºC, the contents were

transferred into an acrylic container measuring 5cm x 5cm x 8cm. When agarose was used to embed hybrid gel phantoms and tissue, the same process was followed with the addition of submerging the target within agarose during the cooling process.

4.2.3 *Measurement of Physical and Acoustical Properties*

The weights of the gels were measured using a standard analytical laboratory balance and volume using a water displacement technique in a beaker, thus yielding the density measurements. The frequency dependent attenuation and the speed of sound were measured using a through-transmission water substitution method as described in [124]. Two ranges of frequency 500-800 kHz and 2.0-2.3MHz were utilized in the measurement process. A linear fit regression line with zero intercept was used to calculate the slope in dB/MHz. The slope was divided by the measured thickness of the gel to yield the attenuation coefficient in dB/cm/MHz.

To determine whether these samples could be used at elevated temperatures (such as boiling histotripsy), separate gel samples were vacuum sealed in food saver bags and submerged in a temperature-controlled water bath using an immersion circulator (Model No. 1112A, VWR, Randor, USA). The bath was maintained at 98^{o}C, and the gels were kept in place for an extended period to observe if the gels remained in a solid state or melted. After the submergence period, the gels were removed from the bags, blotted, and weighed to determine if there was any significant weight loss.

Two techniques were used to estimate the stiffness (Young's modulus) of the gels, one using shear wave elastography (SWE) with an Aixplorer ultrasound platform (Supersonic Imagine, Aix-en-Provence, France) and the other using a custom-made spherical indenter setup (indentometer).

For SWE, an SL15-4, a 256-element linear transducer (Supersonic Imagine, Aix-en-Provence, France) with a bandwidth of 4-15MHz was mounted on to a custom built manual linear positioning system, as illustrated in Figure 4.2. A set of 16-gauge copper wires were embedded into the hybrid gels to act as locational references. The pins were positioned so that each remained several cm from the actual measurement zone. The gel was then placed in a container of deionized water lined with rubber to absorb and reduce reverberations. Measurement zones were identified and marked at known distances away from the reference pins. Each frame captured provided a 2D image with shear wave data, and regions of interest were identified. The medium is assumed to be incompressible; therefore the shear modulus is multiplied by a factor of 3 by the system to obtain the Young's modulus taking into account normal density of tissue. The size of each region of analysis ranged from 2-5mm in diameter and the data was recorded for each slice. A 3-dimensional SWE stiffness map with the Young's modulus was recorded by moving the positioning system in intervals of 1mm and collectively stacking the data across all frames. The transducer setup was operated in phantom penetration mode to get the most complete B-mode image and SWE based stiffness data which were subsequently recorded.

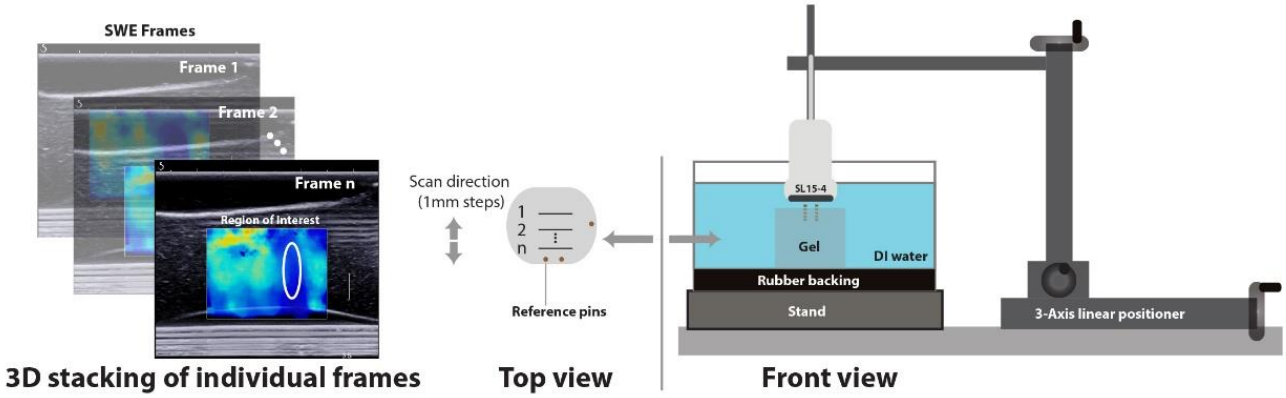

Figure 4.2. Experimental setup demonstrating the method for acquiring a 3-dimensional SWE map of hybrid gels. (Right) A SL15-4 imager is held above the gel in a water bath in cross-sections aligned by reference pins. (Left) Individual B-mode and SWE frames were acquired for each cross section to estimate uniformity and stiffness.

A custom indentometer was built using a spherical ball indenter (8 mm diameter) attached to a vertical linear positioning stage consisting of a linear slide drive driven by a lead screw and connected to a stepper motor. The 8mm ball diameter was chosen with relative to the size of the gels made which were ~20mm in thickness, to keep the contact radius and the displacement small compared with the sample size [125]. An Arduino Uno microcontroller board (Arduino, Somerville, MA) with a motor driver shield was used to control the displacement of the indenter via MATLAB (MathWorks., Inc, Natick, MA). The force corresponding to each displacement was measured by a laboratory balance (Acculab ALC-320-3; Sartorius Mechatronics Corp., Bohemia, NY, USA) as the change in effective weight of the gel sample. These components allowed programmatic control of displacement with a resolution of 2.5 μm along with force measurements with a resolution of 1 mg. A few drops of water were placed onto the sample. The weigh scale was tared and the indenter was brought into contact with the water droplet. The surface tension of the water pulling away

from the gel surface on the hemisphere resulted in a net negative weight displayed on the. As the indenter was bought close to the sample and nearly made contact, the net weight became net zero thus ensuring it was at a null position. The indenter was then lowered in small steps (step size- 0.2 mm) with a speed of (1 step/second) while recording the weight measured by the balance vs the indenter displacement. Previous works [124,126,127], have reported in detail the measurement technique. The shear modulus μ was then calculated from the following equation:

$$F^{\left(\frac{2}{3}\right)} = \left(\frac{16\mu}{3}\right)^{2/3} R^{\frac{1}{3}}.d \quad (4.4)$$

where F is the force acting on the balance, R is the radius of the indenter, and the d is the sample displacement. The net Poisson's ratio was reported to be close to 0.5[128] thus, the conversion to Young's modulus was to be done by multiplying the shear modulus by a factor of 3.

The indentometer setup was calibrated using Zerdine pucks with reported Young's modulus acquired from Computerized Imaging Reference Systems, Inc (Norfolk, Virginia, USA).

4.2.4 *Experimental Setup and Characterization of Histotripsy Exposures:*

An 18-element 700 kHz transducer with an aperture of 13 cm and focal distance of 11 cm was used to mimic the commercial transducer developed by HistoSonics, Inc [129]. The transducer was designed and fabricated with a central cavity to house coaxially a M5Sc ultrasound imaging probe of a GE Vivid E9 4D ultrasound system (GE Healthcare, Chicago, USA). A custom-built class D amplifier powered by a high voltage source (TDK Lambda GENH600-1.3) with an appropriate electrical matching network was used to drive the transducer. The beamwidth of this transducer's acoustic field at-6dB level was measured at low output level, under linear propagation conditions using a lipstick hydrophone (HGL-0085, ONDA Corporation, Sunnyvale, CA) and was 13.25mm axially and 2.3mm laterally. At higher output levels, the peak focal pressures produced

by the transducer were recorded using a fiber-optic probe hydrophone (FOPH2000, RP Acoustics, Stuttgart, Germany). The highest output levels used in the experiment corresponded to peak positive pressure of 103 MPa, and peak negative pressure of 20 MPa. Output levels were controlled by actively modifying the input DC voltage applied to the amplifier. After submergence into a tank filled with degassed deionized water, the position of the transducer relative to the gel was controlled using a three-axis motorized positioner with linear slides driven by lead screws and stepper motors (Velmex Bislides and VXM controller, Bloomfield, New York, USA). Agarose gels or hybrid gels (embedded in agarose) were placed into the tank using a fixture with an acoustic window that introduced minimal disruption to the acoustic pressure field. The fixture location was controlled by the motorized positioner.

4.2.5 *Treatment Parameters*

Previous work using histotripsy to treat BPH was used as a basis for parameter selection. From the prior work by [51] utilizing the commercial system, the following pulse parameters were used: the center frequency was set to 700 kHz with a pulse repetition frequency (PRF) of 500 Hz and pulse duration of 3 cycles (hereafter referred to as "high-PRF" settings). The dosage was established from the prior clinical study and estimated to be equivalent to a pulse count of 25000 per point [105]. A higher dose of 50000 pulses/point was also explored under the same parameters in a subset of phantoms.

Due to the limited efficacy of the high-PRF parameters in producing objective improvements in the prior clinical trial, a low-PRF (10 Hz) exposure was also tested, based on studies indicating that low-PRF, long pulse duration parameters resulted in more complete ablation due to the formation of larger bubble clouds [6,62]. The pulse count was determined from the dose response performed in hybrid gels (Table 4.3). The alternate parameter settings will be

referred to, hereafter, as “low-PRF” settings. These treatment parameters were tested in order to establish robust correlation of histotripsy response in hybrid gels to *ex-vivo* BPH tissue. The pressure levels for creating volumetric lesions in gels and prostate, as well as evaluating the dose response of the gel were determined at +10% of the pressure threshold observed by imaging for creating sustained cavitation clouds.

Table 4.3. Treatment Paradigms

Parameters	**Frequency (kHz)**	**Pulse Repetition Frequency (Hz)**	**Pulse Duration (cycles)**	**Mean Peak Positive Pressure (MPa)***	**Mean Peak Negative Pressure (MPa)***
High-PRF	700	500	3	54-108	14-20
low-PRF	700	10	20	95-108	16.6-20

***For dose response, volumetric treatment, and prostate tissue experiments*

4.2.6 *Hydrogel Histotripsy Response Experiments*

Four sets of experiments were conducted to determine how the hydrogel phantoms compared with existing tissue phantoms and ex-vivo tissue, as well as their response to histotripsy sonication. These experiments are delineated below. A detailed diagram of the bench top hybrid gel experimental test and visualization (high Speed camera, LED light source, focusing lens and power source) setup is presented in Figure 4.3. For treating tissues, a similar setup was used without the visualization.

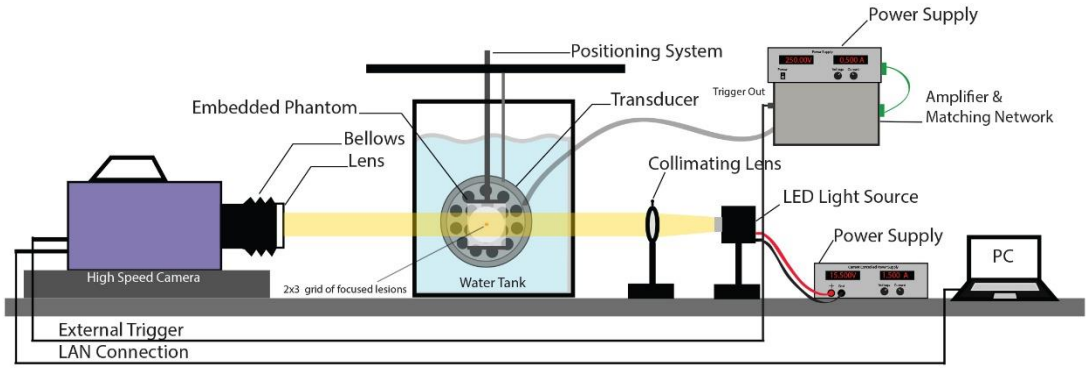

Figure 4.3. High speed camera setup for bench top bubble visualization experiments. An LED source is used for back illumination through the gel. The transducer is aligned orthogonally to the camera and focused into the gel in the field of view. An external PC is used to record the captured images from the camera.

1. ***Volumetric Treatment Experiments*:** The goal of these experiments was to determine the changes in the gel through B-mode imaging, SWE and visual inspection of lesion using phase contrast microscopy when creating volumetric histotripsy lesions. Phase contrast microscopy uses an optical mechanism that translates phase variations in the gel into light intensity changes that can be visualized as differences in contrast. Untreated regions have uniform, intensity, with treated regions having varying contrast. The gels were sectioned and visualized using a Nikon Eclipse 80i; Nikon at 4x magnification using a phase contrast filter. A series of images were taken and stitched through NIS elements (Nikon Instruments Inc, Melville, New York, USA) to visualize the complete set of lesions and qualitatively deduce the dose response. To create volumetric lesions, gels (n=3 per type) were first mounted on a fixture and placed into a tank of degassed and deionized water as shown in Figure 4.3. Volumetric treatment zones were then created by translating the gel sample with the motorized positioner in a raster fashion with 1.15mm steps within a 3X3 rectangular grid. At each step a certain number of pulses was applied: 25K or 50K per step

at the high-PRF setting, and 10k per step at the low-PRF setting. Post treatment, treatment efficacy was evaluated with B-mode US, looking for hypoechoic changes indicating complete liquefaction. [130]. For SWE, pre-treatment SWE measurements of the hybrid gels (of each formulation) were taken to establish stiffness. Post-treatment the stiffness of the gels was remeasured at the same designated sites from earlier using the SWE setup to evaluate the stiffness reduction, as would be expected from tissue treated with histotripsy [130]. A Wilcoxon signed rank test was utilized to measure the change in stiffness in each region, before and after treatment. The reason for choosing a Wilcoxon signed rank test was due to presence of right censored data observed with some of the shear wave measurements. The statistical significance was set at $P < 0.05$. The SWE and B-Mode data were analyzed over 3 frames for each sample where visual cues showed a change in B-mode and SWE. The frames were chosen such that it covered a frame at the beginning of lesion, at the middle and towards the end of the lesion, thereby including the edge cases.

2. ***Prostate Tissue Experiments*:** The purpose of this set of experiments was to compare changes in tissue with those observed in the gel phantoms. Deidentified ex-vivo human BPH prostate tissue samples (n = 3 for each test setting) acquired from simple prostatectomies from patients with symptomatic BPH and were sonicated to produce volumetric liquified regions. The tissue samples ranging from 5-10 cc were embedded in 1.5% agarose gels prepared as described above and the experiments were performed within 6-8 hours of collection. B-mode and SWE measurements were taken at designated locations prior to the treatment to establish baseline stiffness. The embedded sample was placed in a water tank filled with deionized and degassed water. The sample was visualized

with coaxial ultrasound imaging probe, and the transducer focus was positioned at 5mm depth within the sample. The pressure levels for prostate tissue experiments were determined at +10% of the threshold observed for creating sustained cavitation clouds in the range included in Table 4.3. Using a motorized positioner, treatments were performed in a grid (ranging from 3x3 to 6x6 points) spaced in a plane orthogonal to the propagation axis of the transducer at both high-PRF and low-PRF exposures with step size of 1.15 mm so the foci overlapped to create a volumetric lesion. Grid sizes were varied depending on size of respective prostate samples. A pulse count of 25K and 50K per point was used for the high-PRF exposure, which translated to 14.4 and 28.8 seconds treatment per step. For the low-PRF exposure, a pulse count of 5K and 10K was used, which translated to 144 and 288 seconds per point. Post treatment, the samples were reimaged using B-mode and SWE (data collected from 3 frames) and sections of the sample containing the treated lesion were fixed in formalin for histological analysis (Masson's trichrome & hematoxylin and eosin staining). A Wilcoxon signed rank test was utilized as done prior with the gels to measure the change in stiffness in each region, before and after treatment with the statistical significance set to $P < 0.05$.

3. ***Bubble Activity Experiments*:** The goal of this experiment was to compare the bubble cloud generated across different gels and treatment parameters based on the techniques described in [13]. The following steps outline the methodology for capturing bubble cloud activity. A current controlled source coupled with an LED light was used to illuminate the path of the treatment with the help of a collimating lens. The high-speed camera (Photron Fastrax APS-RX, Photron, San Diego, California, USA) with an 80-200 mm zoom lens

and bellows extension was used to capture bubble activity across different treatment paradigms. A delay of 80 µs was maintained between the input pulse sent to the transducer and the camera trigger, to enable the camera to capture the bubble cloud formed 8 µs after the wavefronts arrive at the focus. The shutter speed was set to 2 µs to capture a single frame for every pulse. The amplifier and the motorized setup were controlled via MATLAB using a custom-built program [62]. Both the agarose and hybrid gels (all 3 formulations, n=1) were sonicated with both parameter combinations at an acoustic pressure of 20 MPa P-, and the bubble cloud generated was captured using the high-speed camera over 2000 frames. Captured bubble cloud data was compared qualitatively to determine differences in bubble size and cloud dynamics (whether bubbles are dissolving between pulses).

4. ***Dose Response Experiments:*** The purpose for this set of experiments was to evaluate the dose response of the 85/15 hybrid gel to a fixed set of histotripsy parameters in comparison to the standard 1.5% agarose gel (n=1) of comparable stiffness. From this measurement, the lesion development in the gels as a function of pulse count was evaluated at a single acoustic focal site. Pressure amplitudes were set based on the threshold for sustained cavitation clouds and operated at +20% to form a single lesion. Pressure thresholds varied across both gel formulations and exposure settings but were within the range found in Table 4.3. The focus of the transducer was placed approximately 5mm beneath the surface of the gel. The pulse count was varied from 20-3000 pulses in the agarose gel and from 100-10000 pulses for the (85/15) hybrid gel.

4.3 RESULTS

4.3.1 *Measurement of Physical and Acoustical Properties*

To evaluate polyacrylamide/alginate gels that mimic ex-vivo human prostate tissue, we first established the mechanical properties inherent to prostate tissue. Using SWE, we determined the Young's modulus of ex-vivo human prostate specimens (n=17). As shown in Figure 4.4, the median Young's modulus of ex-vivo human prostate tissue was 55.4 kPa but varied over a large range of from 15.1kPa to 124.4 kPa. The gels increased in stiffness as the ratio of alginate was increased. On shear wave elastography, the gels had median Young's moduli of 90.1, 62.7, and 41.3 kPa for 85/15, 90/10 and 95/05 gels, respectively. Figure 4.4 illustrates that the different gel compositions approximate the Young's moduli of BPH tissue across its stiffness range, although do not necessarily reach the extremes. Table 4.4 captures the calculated means and percent deviation of the gels and the tissue and show the gels to be relatively homogeneous with the tissue showing more heterogeneity as expected.

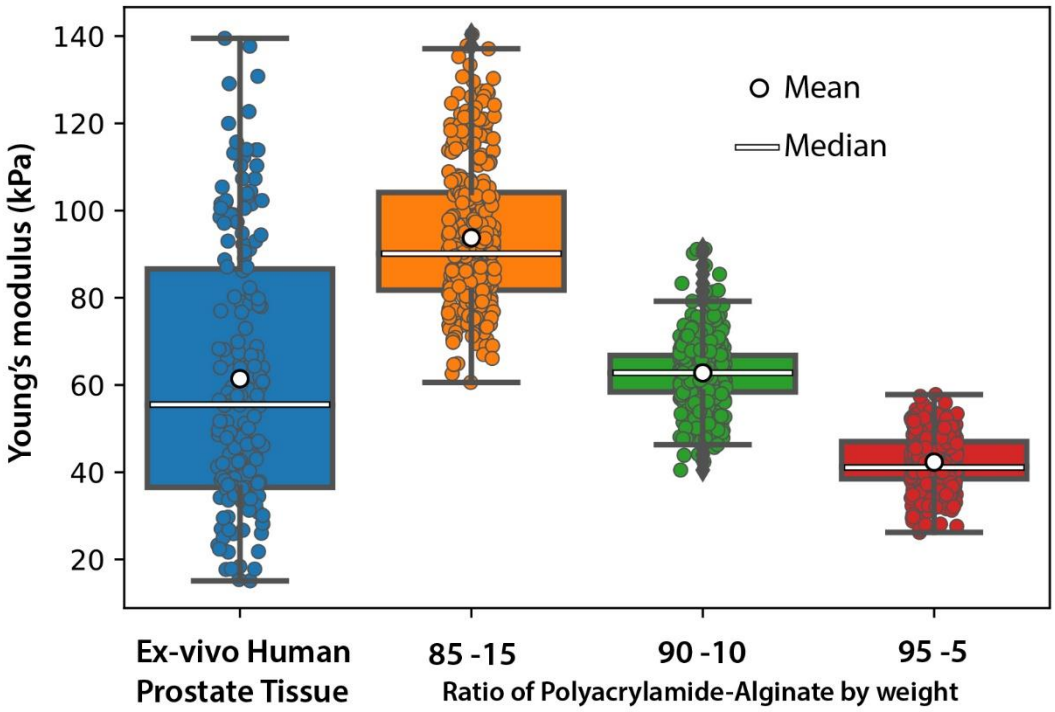

Figure 4.4. Measured Young's moduli for different compositions of polyacrylamide/alginate hybrid gels and ex-vivo human prostate tissue. Varying the ratio of acrylamide to alginate allows approximation of ex-vivo human prostate tissue across its stiffness range.

Table 4.4. Mean and percent deviation of the Youngs's modulus of the hybrid gels and tissue as measured using SWE.

Gel Type	Mean ± St. Dev. (kPa)	% Deviation
85/15	93.73±16.67	17.78
90/10	62.77±7.28	11.6
95/5	42.33±6.011	14.2
EVHP	61.44±29.77	48.45

Three hybrid gels from each configuration were measured using both shear wave elastography and indentometry and the results are summarized in Table 4.5 In general, the indentometer reported lower stiffness values with respect to SWE across all gel compositions by a similar margin. Additionally, the Young's moduli of the measured agarose gels (n=3) yielded a value of 109.2±3.3 kPa, by indentometry.

Table 4.5. Indentometry vs Shear Wave of Hybrid Gels

Gel Type	**Indentometry Measured Range (kPa)**	**SWE Measured Range (kPa)**	**% Difference from SWE**
85/15	48.25±12.06	63.62±21.51	24.15
90/10	25.41±3.97	37.51±8.56	32.25
95/5	7.87±8.80	11.72±0.10	32.81

Table 4.6 highlights the acoustic properties including density, speed of sound, impedance, and attenuation. The acoustic properties of the hybrid gels were in-line with other well-established hydrogels (agarose) and had values representative of prostate tissue, although the attenuation was somewhat lower and similar to other pure hydrogels. There were small variations in acoustic properties between different gel compositions across various ratios of polyacrylamide to alginate without clear trends. The values ranged from 1020 – 1056 kg/m^3, 1514 - 1528 m/s, 1.54 -1.61 MRayls and 0.06 to 0.14 dB/cm/MHz for density, speed of sound, acoustic impedance, and attenuation, respectively.

Table 4.6. Acoustic properties of polyacrylamide/alginate hybrid gels in comparison to agarose gels and prostate

Gel Type	Attenuation (dB/cm/MHz)	Speed of Sound (m/s)	Density (kg/m^3)	Impedance (MRayls)
85/15	-0.06 ± 0.01	1528 ±6	1024 ±18	1.57 ±.03
90/10	-0.07 ± 0.04	1514 ±5	1020 ±13	1.54 ±.03
95/05	-0.14± 0.06	1520 ±5	1056 ±24	1.61 ±.04
*Agarose [1]	-0.04 – -0.46 dB/cm/MHz	1503 – 1526 m/s	-	-
*Prostate [2]	-0.72 dB/cm/MHz	1530 m/s	-	-

*Values derived from literature [1] [114] [2] [131]

4.3.2 *Histotripsy Response Experiments*

Volumetric Treatment Experiment

We tested the functionality of the hydrogels as tissue phantoms for histotripsy. Two primary measurements for evaluating treatment effects in the hybrid gels were captured: echogenic changes on B-mode ultrasound imaging and Young's modulus changes on SWE. B-mode images in Figure 4.5a demonstrate hyperechoic changes in all three gel formulations treated with the high-PRF exposures. However, these hyperechoic changes on B-mode did not translate to a marked difference between Pre to Post treatment regions on the SWE color map when treated with the high-PRF histotripsy parameters. In comparison, the low-PRF parameters produced defined lesions in the hybrid gels as demonstrated by B-Mode images in Figure 4.5B where a hypoechoic center bordered by a hyperechoic rim is observed. These changes noted on B-mode corresponded to marked changes in the Young's moduli of the hypoechoic region as evidenced by the clear changes in the SWE color map for each gel formulation.

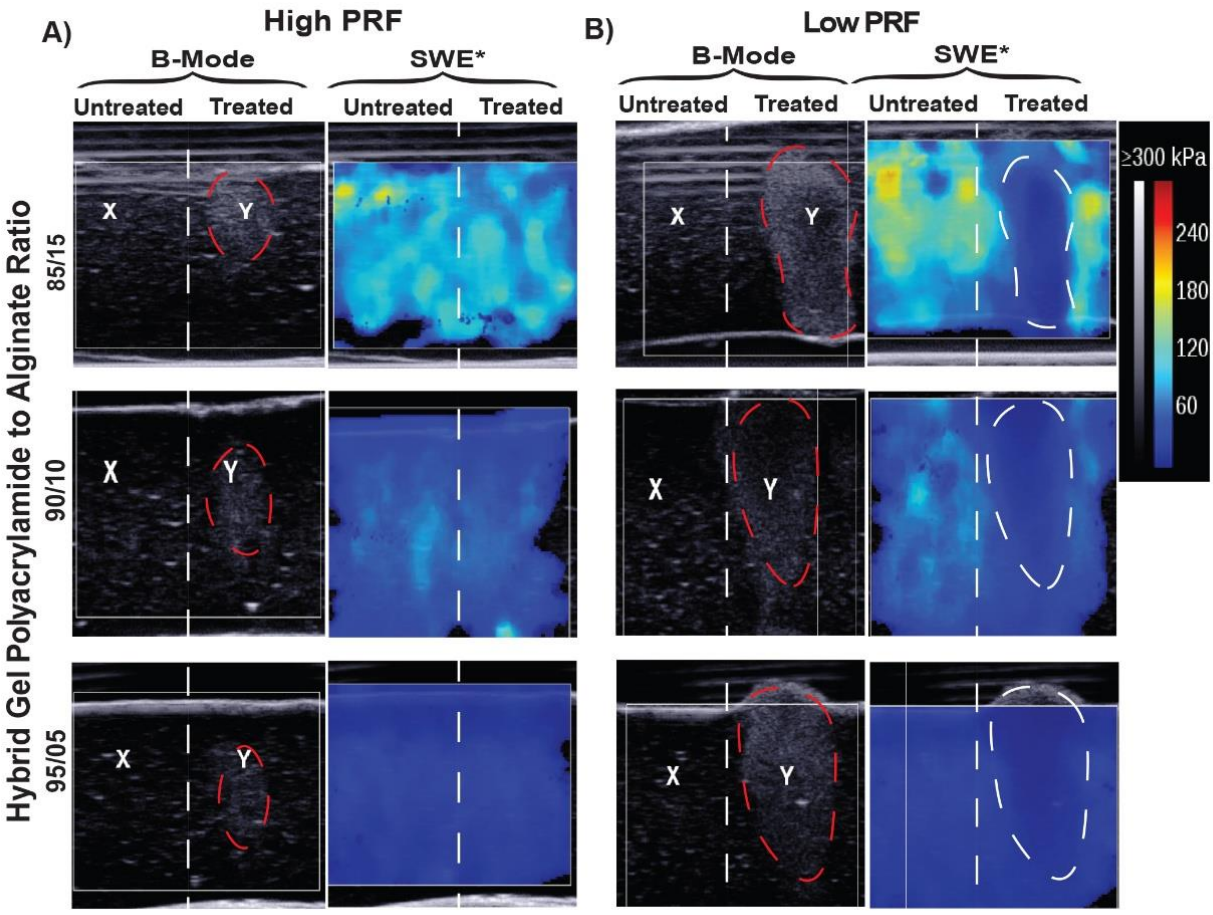

Figure 4.5. Evaluation of histotripsy induced damage in acrylamide/alginate hybrid gels with B-mode and shear wave elastography (SWE) A) B-mode and SWE evaluation of high-PRF parameter settings showing hyperechoic bubble formation on B-mode (highlighted in red) and failure of treatment to induce changes in SWE color map B) B-mode and SWE evaluation of low-PRF parameter settings showing hypo + hyperechoic changes on B-mode (highlighted in red) and corresponding distinct changes in the SWE color map (highlighter in white). The X on B-mode indicated an untreated region while the Y denotes treated region. Quantitative assessment of the change in Young's moduli (Table 4.7) further demonstrated the findings seen qualitatively in the SWE color map.

Table 4.7. Response of the hybrid gels and the tissue to different histotripsy parameters

Treatment Setting	Medium	Test Statistic S Post – Pre (kPa)	P Value
high-PRF – Low Dose	85/15	-13.5	0.129
	90/10	-6.5	0.496
	95/05	-22.5	<0.005*
	Prostate	-15.5	0.0742
high-PRF – High Dose	85/15	1.5	0.910
	90/10	-5.5	0.5703
	95/05	-22.5	<0.005*
	Prostate	-26.0	<0.05*
low-PRF	85/15	-20.5	<0.005*
	90/10	-22.5	<0.005*
	95/05	-22.5	<0.005*
	Prostate	-22.5	<0.005*

*Statistically significant.

Prostate Tissue Experiment

To determine the utility of hybrid gels in predicting efficacy of treatment parameters in prostate tissue samples, ex-vivo human prostatic tissue samples were treated with both high-PRF and low-PRF exposures, with Figure 4.6 highlighting the high-PRF-High dose and low-PRF sonication for a 90-10 gel and prostate tissue of similar stiffness. Histotripsy damage was visualized under phase contrast microscopy at different parameter settings within hybrid gels and treatment effects in prostate tissue were evaluated histologically with H&E and Masson's trichome stains. As shown in Figure 4.6A, phase contrast imaging of hybrid gels at the high-PRF parameter settings show sparse damage; whereas the low-PRF parameter settings produced higher overlap between lesions and the expected area of treatment. The histologic findings (Figure 4.6B) were consistent with findings seen in under phase contrast illumination for gels (Figure 4.6A).

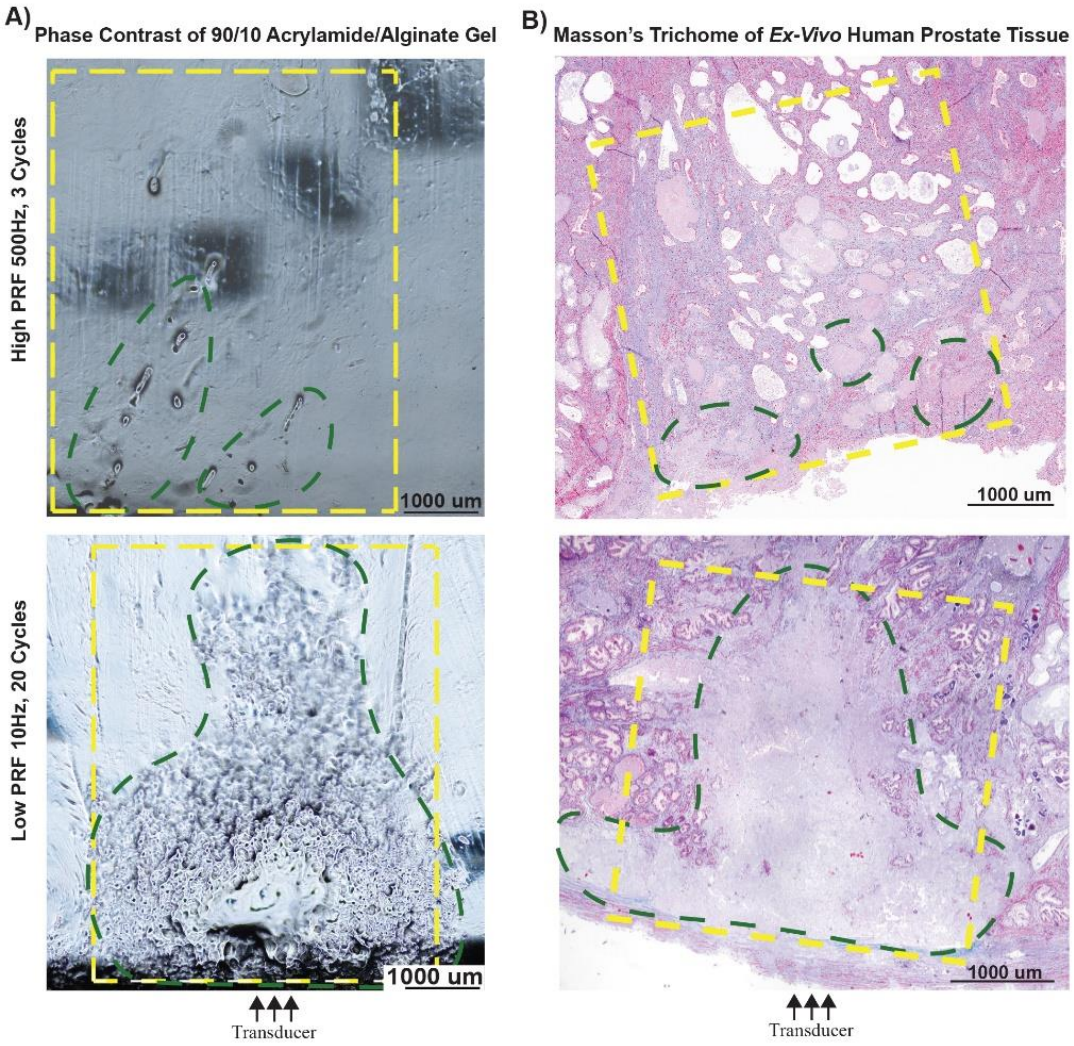

Figure 4.6. Correlating treatment effects in polyacrylamide/alginate gels to lesion formation in ex-vivo human prostate tissue; green outline indicated areas of histotripsy damage and yellow outline denotes area of intended/expected treatment A) Evaluation of histotripsy induced damage under phase contrast microscopy in hybrid gels between treatment area (green) and expected treatment area (yellow). B) Masson's trichrome stained ex-vivo human prostate tissue, showing a complete homogenized lesion (green) within the expected treatment area (yellow).

Treatment with high-PRF parameters yield discrete pockets of damage rather than a contiguous homogenized lesions indicating poor concordance between actual and expected treated areas for both the hybrid gel and the prostate tissue, covering only 19% and 12% of the expected

area respectively as measured from the phase contrast image and histology section. In contrast, the treatment area generated by the low-PRF parameter settings was higher with damage seen over 72% and 66% of the expected area for the hybrid gel and tissue respectively. However, at low-PRF exposures there were some intact structures (fibromuscular stroma with glandular elements) within the treatment area surrounding otherwise homogenized tissue. Some visible artifacts (darkened spots) were also noted with the high-PRF gel phase contrast images. These were a result of the equipment's optical limitation and the slice thickness of the sample. Quantitative assessment of the change in Young's moduli pre and post treatment for the prostate at all sonications are summarized in Table 4.7.

The 95/5 hybrid gel showed a significant change with $P<0.005$ in the post vs pre treatment test statistic for all treatment exposures indicating liquefaction. For the prostate, change in Young's modulus was significant with a P value of <0.05 and <0.005 with the high-PRF- High dose (50k pulses/step) and the low-PRF exposures respectively, while no significant difference was seen with the high-PRF – Low Dose (25k pulses/step) exposure. For the 90/10 and 85/15 hybrid gel, the change in Young's modulus was significant with a P value <0.005 with the low-PRF sonication indicating liquefaction, while no significant change was observed for any of the high-PRF low or high dose sonications.

Bubble Activity Experiment

Cavitation cloud images were recorded by high-speed photography for each exposure in the hybrid and 1.5% agarose gels. Figure 4.7a highlights the difference in the cavitation cloud between agarose gels and hybrid gels (90/10 for example) over frames 1, 500, 1000, and 2000 while part B shows the overlay of the bubble cloud over 2000 frames. The transducer is placed on

the left relative to the frame with the focus towards the center of the frame. The bubble cloud typically forms at the focus and grows towards the transducer. In agarose gels, irrespective of the PRF, the cloud appeared predominantly around the focus, with bubbles appearing at different locations between pulses, although appearing denser with the low-PRF exposure. In the hybrid gels, the cloud pattern appeared static (*i.e.*, bubbles formed in the same locations between pulses) with minimal cloud changes throughout the high-PRF exposure for all 2000 frames. In contrast, when treated with the low-PRF exposure, there was an observable increase in the cloud area and formation of new bubbles in successive pulses. The bubble area increases, as seen in Figure 4.7b was also substantially greater than the agarose gel exposed to similar exposures. In the agarose gel, the increase in bubble area between the high and low-PRF exposure parameters was about 6% and for the hybrid gel the difference was an average of 83%.

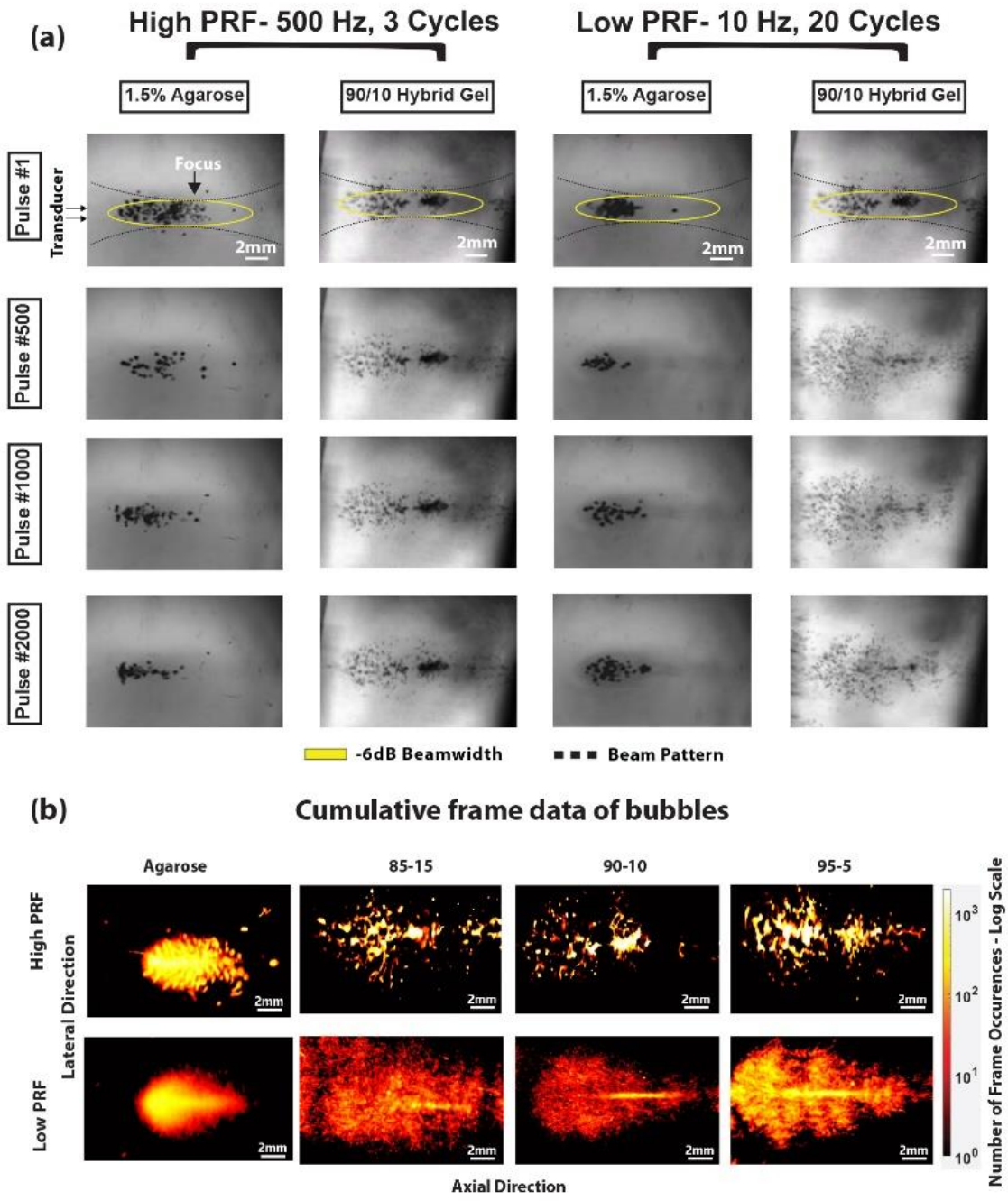

Figure 4.7. (A) High speed camera images showing cavitation cloud progression in agarose vs acrylamide/alginate hybrid gels at both high-PRF and low-PRF parameters. (B) Superimposed bubble clouds from all 2000 frames, with the dynamic range of frames measured varying across Low and high-PRF settings, with the white arrows encompassing the total cumulative cloud observed.

Dose Response Experiment

Figure 4.8 shows the dose response to low-PRF exposures under phase contrast microscopy in an 85/15 polyacrylamide hydrogel and a 1.5% agarose gel. Both gels were treated at different doses to determine the minimal threshold to produce a liquefied cavity. As seen in Figure 4.8, the hydrogels show damage at 400 pulses but appear similar up to 3000 pulses. The damage caused optical variations within the hybrid gels, but failed to form a complete liquefactive cavity, covering only 37% of the total lesion volume. In contrast, histotripsy damage with low-PRF exposures produced prominent damage in 1.5% agarose gels at 200 pulses with complete cavity formation occurring at 300 pulses, indicating more rapid breakdown of the gel. These images show that hybrid gels of similar stiffness are more resistant to histotripsy, as evidenced by the minimal cavity formation even with 10 times the dose administered to agarose gel.

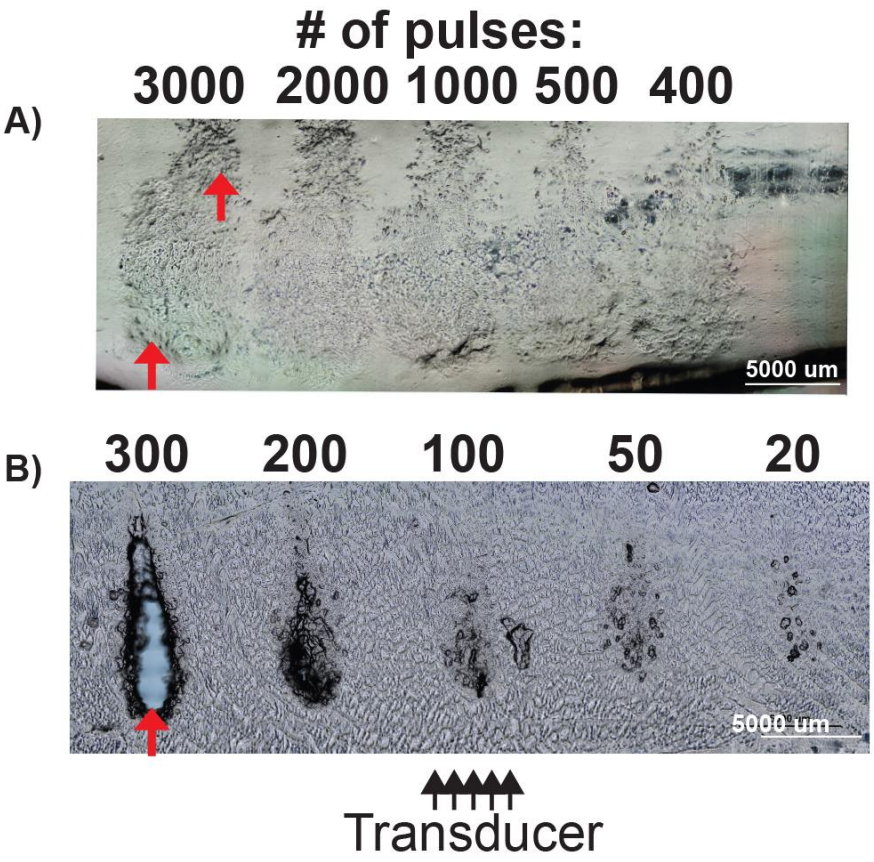

Figure 4.8. Phase contrast image for low-PRF parameter settings in 85/15 polyacrylamide gel vs 1.5% agarose gel A) 85/15 polyacrylamide gel showing progressive refractive changes indicating damage at increasing pulse count. The cavity present is denoted by red arrows (B) Dose response evaluation in 1.5% agarose gel showing cavity formation that progresses to a portion of the beamwidth at 200 pulses with complete cavity formation (fully defined lesion) at 300 pulses (red arrow).

4.4 DISCUSSION

The results demonstrate that the developed phantoms produce a response to histotripsy comparable to BPH ex-vivo tissue and is similar in terms of acoustic and mechanical properties, making it an appropriate candidate for optimizing treatment parameters. A variety of gel phantoms were explored in the past for treatment optimization, visualization and feedback by different researchers, including agarose lined with red blood cells [96,132], polyurethane [86,91], collagen[133], agar, gelatin [124] polyacrylamide[126,134–136]. While these gels closely approximate both the acoustic and mechanical properties of soft tissue, they do not explicitly mimic the toughness of fibrous tissue. The stiffness and toughness of the current hybrid gel described in this paper could be modified by simply manipulating the ratio of acrylamide -alginate with the gels becoming highly stiff and tough as the alginate content increased [102,121,123]. The results also further indicate that stiffness alone does not determine treatment efficacy, and that toughness is an important factor, as seen in the dose response experiments (Figure 4.8) where the number of pulses required to treat the agarose was only one-tenth that of the hybrid gel of similar stiffness. The reason for the increased toughness of this phantom is the cross linking of the alginate chains involving an improved ionic cross linking between calcium and carboxyl ions [102], which is similar to the collagen and elastin cross linking seen in fibromuscular hyperplasia typical for BPH tissue vs weak hydrogen boding in the agarose. Fibrous tissues in general respond non-linearly to external stress, a characteristic that explains the high fracture toughness of these materials, but such materials have been treated with histotripsy effectively in the past with increased pulse count [137 40]

The acrylamide-alginate hybrid gel provides multiple avenues to analyze treatment efficacy. The high transparency of gels enables study the dynamics of cavitation through high-speed camera observations of the bubble cloud. Transparency also allowed immediate post-

treatment observation of the lesion dimensions through the use of phase contrast microscopy as explored in this study. It was shown that treated regions are easily identifiable as the damage produces minor variations in the optical homogeneity of the gel, which further assist in analyzing the extent of damage.

The hybrid gels also appear to contain acoustic scatterers, thus providing a way to subject them to ultrasound imaging techniques like B-mode and SWE. B-mode imaging was successfully used in the past with RBC – agarose phantoms [138] and BSA – polyacrylamide gels [139], where RBCs and BSA act as scatterers. SWE was shown to ascertain viscoelastic properties of the medium [140] and as a successful imaging feedback technique in treating tissue [141]. The hydrogels respond to histotripsy treatment in a way similar to ex-vivo tissue, in that fully treated volumetric lesions resolve with hypoechogenicity on B-mode, with clear changes in the SWE mapping. Partially treated areas often resolved as hyperechoic zones due to potential disruption in the crosslinking, but that did not necessarily show significant change in stiffness. While the possible explanation and mechanism is not well understood at this point, it is possible that as the gel is partially damaged, it creates areas of heterogeneity, with 'disrupted' and intact regions with different density, and the size of these regions may have acoustic heterogeneity on a scale that leads to more scattering.

The response of the gels was found to be different between sets of exposure parameters. high-PRF parameters tested across the different experiments showed minimal damage both in tissue and in hybrid gels in most cases, whereas low-PRF parameters consistently showed significant damage. The bubble clouds observed in the gels under different parameters showed that they followed the same principles of shock wave scattering as described in previous studies [6,84]. Both in high-PRF and low-PRF exposures in the hybrid gels, once the sonication ended, the

bubbles collapse but do not necessarily dissolve immediately, indicating a form of bubble stabilization. They were proportionally longer for the high-PRF settings and with longer dose durations vs the low-PRF exposures. This could possibly be due to the structural differences between the hybrid and the agarose phantom, as such behavior was not observed in the latter. These structural differences could also explain the differences in the observed bubble cloud areas, where in the hybrid gel the bubble cloud comprised smaller bubbles spread over a larger area. In contrast, the cloud comprised larger bubbles confined to a smaller area in the agarose gel. One other possible reason for these observed differences in bubble cloud dynamics could be due to increased bubble nuclei present in hybrid gels which could interact with the incident acoustic field to make the gels more resistant to treatment. In this way, bubble nucleation could be an important distinction between hybrid and agarose gels beyond the differences in structure and potential differences in toughness.

There are several potential reasons for the relatively lower efficacy of high-PRF exposures, such as bubble shielding or non-dissolution of bubbles between pulses[62]. Pre-focal cavitation bubbles may prevent the acoustic energy from reaching the focus, as observed in other prior studies[142]. High-speed photography showed the bubbles in the clouds occurring exclusively in the same location over all 2000 pulses, which could lead to liquefaction occurring only in those small areas, making it less effective. Additional experiments using high-PRF settings at extremely high pulse counts at almost half a million did show measurable damage in the lower stiffness 95/5 gel, but such a dose would be impractical to perform in clinical scenarios.

The trends observed with the pre vs post treatment elasticity for the hybrid gels and ex-vivo tissue demonstrate that the low-PRF exposure effectively liquifies them. No such significance was seen for any gel combination or the prostate with the high-PRF low dose settings. At a higher

dose however, the prostate and the weaker 95/5 gel showed a significant change in stiffness post treatment. For agarose phantoms, the use of indentometry was the only source of stiffness measurements aside from existing literature [143]. The indentometry technique could not measure the stiffness of the prostate samples due to their small dimensions. There was a consistent discrepancy between the shear wave and indentometry techniques measuring 24-33% lower for indentometry vs. SWE, which may be due to differences in the shear rates applied in each technique. Another limitation of the study was that the toughness of the hybrid gels and ex-vivo tissue samples were not directly measured. However, the toughness of similar hydrogels is reported in literature [102], and were further established through the dose response studies here.

This phantom may have multiple uses in the development of histotripsy therapies. For one, this gel could be expanded to test boiling histotripsy modalities, as preliminary experiments showed that these gels would not melt up near 100ºC. The 3-dimensional nature and transparency of the gel also makes it easy to study the boiling bubble behavior under different exposures and provide further insights. We envision our future experiments to expand on this initial study to perform more systematic comparisons of histotripsy pulsing parameters, or complex treatment methodologies [40,60] to reduce treatment time while maintaining efficacy.

4.5 CONCLUSION

This work demonstrated the formulation and use of a tough hydrogel from alginate-acrylamide that is optically transparent was found to mimic ex-vivo pathologic BPH tissue acoustic and mechanical properties. The phantoms had a response to histotripsy that could be measured by B-Mode ultrasound and SWE. The results further established that the hybrid hydrogels demonstrate similar lesion formation to ex-vivo human BPH tissue and can effectively be used to

provide an initial comparison of treatment parameters, providing immediate feedback. Such phantoms may be used precursory to translational studies to rapidly test the efficacy of different histotripsy parameters in treating BPH and other fibrous tissues.

CHAPTER 5. A COMPARATIVE STUDY OF HISTOTRIPSY PARAMETERS FOR THE TREATMENT OF FIBROTIC EX-VIVO HUMAN BENIGN PROSTATIC HYPERPLASIA TISSUE

5.1 INTRODUCTION

Benign prostate hyperplasia (BPH) is a noncancerous enlargement of the prostate gland, wherein an imbalance in cell proliferation and cell death leads to an increase in the epithelial and stromal cell count in the periurethral area of the prostate. It is the only solid organ to grow throughout a man's life, and thus, the incidence of BPH increases dramatically with age, particularly in individuals over 60 years of age. BPH is among the top 5 noncancer-related disorders for men[144]. While BPH in many cases may be asymptomatic and not disruptive, it is one of the leading contributors to lower urinary tract symptoms (LUTS), thus affecting quality of life and increasing the chances of associated medical morbidities. Some LUTS include increased frequency, urgency to urinate, nocturia, painful urination, lack of voluntary control, longer voiding, urinary retention and weak flow of urine[145]. Many live with BPH without treatment[146], but doing so can lead to complications such as urinary tract infections, hematuria, urinary retention, and urinary stasis, leading to stone formation and contributing to kidney failure[76,147].

Histotripsy is a non-invasive, non-ionizing modality that utilizes cavitation bubbles to completely disintegrate tissue. Two modalities of histotripsy, shock-scattering cavitation cloud and boiling histotripsy have been demonstrated in preclinical studies to treat a variety of tissues, such as porcine liver, kidney, hematomas, abscesses, and prostate [16–22]. Some studies have shown that histotripsy can spare fibrous tissue[30], but other studies have demonstrated complete disintegration, such as Peyronie's plaque[31], ureteroceles[32], cholangiocarcinoma[33], uterine fibroids[34] etc., which required a higher dose per point.

A recent pilot study has also shown the ability of BH to ablate the *ex vivo* human BPH prostate (EVHP) [148]. The inconsistency between these studies indicates that a gap in knowledge exists in choosing the right treatment parameters to produce safe and effective ablation of these different tissues. In this study, we aimed to compare three sets of treatment parameters to determine lesion progression as a function of dosage and evaluate the outcomes histologically and by stiffness measurements from shear wave elastography (SWE). For histological analysis, we developed a hybrid entropy-based texture analysis algorithm combined with Otsu's thresholding to automatically segment and identify homogenate lesion from surrounding tissue which also took into account the stain inconsistencies.

5.2 METHODS

5.2.1 *HIFU equipment*

The experimental setup consisted of two transducer setups for administering CH and BH along with their respective image guidance platforms.

1) **Cavitation Histotripsy:** CH was administered using a 700 kHz 18-element transducer with an *f-number* =0.85, a focal distance of 11 cm and an aperture of 13 cm. The transducer was constructed from piezoelectric elements (880 ceramic, APC International Limited,

Mackeyville, PA, USA) and fixed using a tungsten-epoxy matching layer to a 3D printed housing lens made from Accura 60 photopolymer (Protolabs, Plymouth, MN, USA). The transducer has a central cavity to coaxially host an M5Sc ultrasound imaging probe from GE Healthcare (Chicago, IL, USA) on a Vivid E95 platform to provide ultrasound B-mode image guidance. A custom-built class D amplifier[149] controlled by a PC was used to electrically power the transducer through a matching network.

2) **Boiling Histotripsy:** BH was administered using a 1.5 MHz 12 element transducer with an *f-number* of 0.77, a focal distance of 5.6 cm and an aperture of 7.3 cm derived from this study [150]**.** The transducer was built using flat trapezoidal elements and bonded to a rapid prototyped focusing lens with a matching layer. B-mode image guidance was provided by a coaxially hosted P4-2 probe on a Sonix RP Ultrasonix legacy system (BK Medical, now part of GE Healthcare, Chicago, IL, USA). The same amplifier system as in the previous section with an added capacitor bank to sustain the longer BH pulses was used to power the transducers through a matching network.

Transducer characterization

Both transducers were characterized for their focal pressure waveforms using a fiber optic hydrophone (FOPH2000, RP Acoustics, Stuttgart, Germany) at a low duty cycle. The -6 dB beamwidth along the three axes was measured using a lipstick hydrophone (HGL-0085, ONDA Corp, Sunnyvale, CA, USA) at low pressure under linear propagation conditions. For the CH transducer, the -6 dB beamwidth measured 13.1 × 2.2 × 2.2 mm (axial × lateral), which translates to a 33.20 mm^3 ellipsoidal focal volume. For the BH transducer, the beam measured 6.7 × 1.0 × 1.1 mm, which translates to a 3.85 mm^3 focal volume.

Pulse parameters and dose

The following pulse parameters (treatment modalities) were used to treat the BPH samples. CH was administered with two pulsing schemes: (i) a high pulse repetition frequency (PRF)-shorter pulse duration treatment (used previously with a clinical system [51],[52]) and (ii) a low PRF, longer-pulse duration scheme, derived from observations of a similar study in eroding soft tissue[151] and from our prior study [53], was used with grids ranging from a minimum of 9 foci points up to a maximum of 25 points with an overlap of 1.15 mm. (iii) BH was administered at a PRF of 1 Hz and 15000 cycles in a similar grid fashion with an overlap of 0.75 mm, which was derived from a similar study from our group on treating EVHP samples[148]. The treatments were administered in a raster scan moving the focus in two dimensions orthogonal to the acoustic axis. The pulse parameter sets are summarized in Table 5.8.

Table 5.8. Pulse parameters used in the study

Treatment modality	Parameter Set Name	Pulse Repetition Frequency (PRF) (Hz)	Pulse Duration (Cycles)	Operating Frequency (MHz)	Duty Cycle (%)	Time Duration per point(s)	Peak Pressure at focus (MPa)
Cavitation Cloud Histotripsy (CH)	High-PRF	500	3	0.7	0.21	15-288	P_+ 54-108 P_- 14-20
	Low-PRF	10	20		0.03	15-288	P_+ 95-108 P_- 16.6-20
Boiling Histotripsy (BH)	N/A	1	15000	1.5	1	15-60	P_+ 68-86 P_- 14.5-15.8

Based on a prior CH-based clinical study [152], it was determined that the average treatment volume was 10.8 cm^3. From the average total treatment time and focal dimensions of the clinical source, we estimated that the average time per focal volume to treat was approximately 30 seconds, and this time was used to determine the duration of treatment for this study. The duration of CH

treatment at each point was set to 15, 30, 60, 87, 144 or 288 seconds. With overlapping treatment points spaced at one-half beamwidth, this would translate to a maximum of ~10k pulses for low-PRF CH and ~500k pulses for the high-PRF CH at the highest time dose (288 s) at the center of the lesion grid. The highest time of 288 seconds was also based on optimization experiments performed in a tissue phantom we developed with mechanical parameters similar to those of fibrous tissue[53]. BH was only performed for time points ≤ 60 seconds based on prior literature, which suggested that fully homogenized tissue can be achieved in softer nonfibrotic models at 15-50 seconds[22].

In both cases, treatment was delivered at focal pressure amplitudes 20% above the threshold at which sustained cavitation or boiling was first observed on B mode ultrasound in each tissue sample while incrementally increasing the output.

5.2.2 *Experimental approach*

Tissue preparation

De-identified human prostate tissue samples (n=23) were obtained from patients undergoing simple prostatectomy procedures for BPH at the University of Washington (UW) Medical Center, Seattle, WA. Patients provided informed consent through NWBioTrust, Seattle, WA which also handled the sample collection and transfer according to an UW Human Subjects Division (HSD) institutional review board (IRB) approved protocol. The study was determined to be an IRB exempt non-human subject research by UW HSD IRB and all experiments were performed in accordance with institutional and National Institutes of Health (NIH) guidelines.

Samples ranged from 5-10 cc and were acquired within an hour of the operation. The samples were stored in phosphate-buffered saline (PBS) until they were embedded in 1.5% UltraPure™ Agarose (Thermo Fisher Scientific, Waltham, MA, USA) for sonication experiments,

which were performed within 24 hours of extraction. The 1.5% agarose solution was made by dissolving 3 g of agarose into 230 mL of deionized water and boiling for 6 minutes, yielding ~200 mL of the final mixture. The solution was then transferred into a casting container and allowed to cool to approximately 40°C before the sample was embedded.

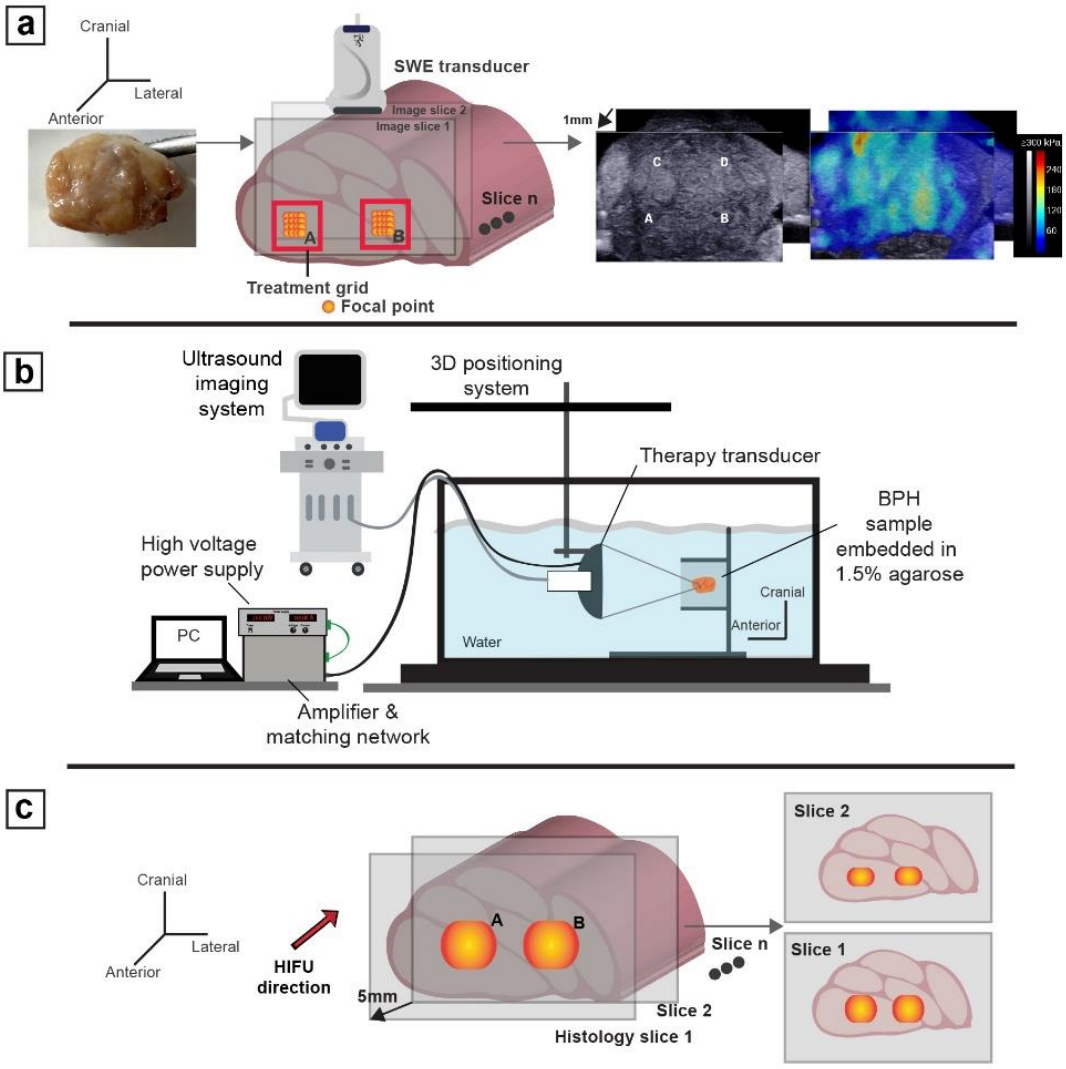

Figure 5.1. Illustrations of the experimental setup (a) Shown from L-R the assumed orientation of the sample with respect to the transducer. The SWE setup captured stiffness measurements at 1 mm intervals along the entire sample transversing from anterior to posterior. An example B-Mode and SWE image of the sample measured using the apparatus is shown. (b) Experimental setup for *ex vivo* treatment of human prostate tissue. The setup shows the samples embedded in 1.5% agarose and placed in a degassed deionized water chamber. The therapy transducer with a coaxially arranged imager is then submerged into the tank with the focus of the therapy positioned within the sample. The therapy transducer parameters are controlled externally using a custom FPGA board and powered by a class D amplifier. Multiple therapy points are delivered as shown by orange dots in a raster fashion. (c) After treatment, the fixed tissue was sectioned for histological analysis in a manner encompassing all the treatment grids

Stiffness measurement, sonication setup, treatment and preparation of samples for histology

The baseline stiffness of the samples prior to embedding in agarose was measured by SWE using a 256-element linear SL 15-4 transducer from Supersonic Imagine (AiXplorer, Aix-en-Provence, France) mounted on a 3-axis positioner[53]. The sample was placed in a fixture aligned with sound-absorbing rubber pads to reduce reverberation and filled with saline solution. The acquisition settings involved using the 'general' preset, set to penetration mode. The regions for treatment were identified by initial coarse measurements using the on-board measurement tool. Next, the SWE maps were collected in 1-mm increments capturing most of the tissue along the length of the sample to generate a 3-dimensional SWE stiffness map. The SWE image plane was perpendicular to the plane in which the therapy was delivered to capture all the treatments in a single plane. Figure 5.1(a) illustrates the orientation, an example of the B-mode image, and the corresponding SWE image.

The agarose-embedded sample was placed in a fixture that provided minimal disruption to the acoustic pressure field and lowered into a tank filled with deionized and degassed water, ideally at approximately 20-25% O_2 saturation, to mimic conditions within the human body. The transducer was attached by optical rods to a motorized positioner and controlled via MATLAB (The Mathworks, Natick, MA, USA). The setup is shown in Figure 5.1(b). Treatment grid points were positioned with 50-70% overlap and delivered in a raster scan with the focus moved from the anterior to the posterior of the sample. Treatment was delivered at least 5 mm from the anterior surface at all points, such that the entire treatment was confined within the sample based on prior studies[153]. The threshold pressure was determined in a volume distinct from the treatment grid, where the amplifier voltage was increased until a cloud was observed, which was verified using B-mode imaging. Treatment was then delivered at +20% above threshold to account for threshold

changes from tissue inhomogeneities. A minimum of a 5-mm gap between each treatment grid was maintained to ensure no overlap between different treatment regimes. The number of treatments and the grid size were determined based on the size of the sample available. Post-treatment, all the samples were removed from the agarose gel, and stiffness measurements were collected by SWE in a similar fashion as outlined above. All the SWE data were then exported for offline processing.

Next, the samples were fixed in a 10% neutral buffered formalin solution for at least 72 hours. Each sample was then segmented into multiple blocks of 5 mm thickness covering all treatment grids as shown in Figure 5.1(c), dehydrated in 70% ethanol, and sent offsite (Scientific solutions, Fridley, MN) for histological processing. Whole mount sections (5 um) taken from each block were stained with Masson's trichrome (MT).

5.2.3 *Histological evaluation*

Qualitative analysis

Histological analysis served as the primary method for evaluating treatment effectiveness. Whole mount MT-stained sections were scanned using an Aperio slide scanner (Leica Biosystems, Illinois, United States). Based on our extensive experience analyzing histotripsy lesions qualitatively, we classified the lesions from this study into the following categories to assess treatment outcomes:

1) ***Partial lesion:*** Damaged pockets coinciding with bubble clouds, as observed in high-PRF bubble cloud images[154]. Homogenized areas that start to appear with larger tissue fragments (broken collagen strands, muscular fibers).
2) ***Complete lesion:*** Fully homogenized lesion with minimal tissue fragments (<~50μm) and cell debris.

Quantitative assessment, areal analysis

In this study, we used textural analysis of histological images to quantify lesion area as a function of dosage for each treatment parameter set using a custom algorithm called Histotripsy lesion quantification by the entropy analysis algorithm (HLQE). For every parameter set and dose, across n=3 samples, one histological slice representing the "center of the lesion" was chosen for quantification to measure the maximum treatment effect. Characteristically, histotripsy homogenizes tissues and reduces their structure to a uniform field of debris. As such, an appropriate method to identify homogenized tissue vs. intact tissue is based on the variation in structure within the image, which is done here through measurement of image entropy. To estimate the fraction of intact tissue within a lesion, a local entropy filter was used on an image of each histological section. Within a subregion of 25x25 pixels in the image, the entropy filter calculates the associated entropy S,

$$S = -\sum p \log_2 p \qquad (5.5)$$

where p is the normalized histogram of pixel intensity counts. Entropy as a function of position is displayed, with areas of low entropy indicating disrupted tissue due to their uniformity and lack of tissue structure. These images were thresholded and converted to binary images using Otsu's method (graythresh function in MATLAB), and areas below the threshold were considered part of the disrupted tissue. Within the region of interest (ROI) consisting of the intended treatment volume, a total of 48 random areas of r=20 pixels were sampled, and the fraction of area disintegrated was calculated as a quantitative estimate of the completeness of treatment. A detailed description of the HLQE algorithm processing steps is included in Appendix A along with performance evaluation results compared against manually segmented histology slides.

A one-sample t-test was performed for the average percentage of tissue destroyed from the histological slides using the HLQE algorithm across all treatment modalities. The null hypothesis is that the measured mean percentage of tissue destroyed in the sample is equal to 100%, indicating a complete lesion, $H_0: \beta 1 = 100\%$ with the alternate hypothesis $H_1: \beta 1 \neq 100\%$ with a=0.05. The outcome of this test will determine the doses at which the average percentage of tissue destroyed is indistinguishable from 100% destroyed tissue. Also, we will establish the threshold value (minimum average percentage of tissue destroyed) to be used for the receiver operator characteristic analysis to be discussed later below.

5.2.4 *Shear wave elastography analysis*

To account for the different starting stiffnesses between the samples, the pre- and post-treatment stiffness changes were measured as the fractional reduction in stiffness from the initial value in the respective grid. The stiffness measurements were processed offline using a custom-written MATLAB algorithm that parametrized the SWE scale from the exported JPEG image of a slice and created an RGB map corresponding to the displayed stiffness for all the pixels present in the on-screen scale. From both pre- and post-treatment SWE maps, the measurement representing the center of the lesion was chosen. Within these planes, the center of the region of interest was manually selected using a freeform ellipse tool of radius (2-4 mm), and the average stiffness within that region was calculated to avoid boundary artifacts often encountered when measuring near the edge of the treatment grid. This process was repeated for all n=3 samples for each treatment parameter set and dose. From the change in stiffness and treatment time, the stiffness change as a function of the rate of reduction (time spent per individual focus) was calculated and plotted. To normalize the different beamwidth volumes of the foci used between the two different CH and BH

transducers, the fractional reduction in stiffness was plotted as a function of the inverse rate of treatment, i.e., the dose normalized by the focal volume.

5.2.5 *Regression analysis between histological analysis and shear wave elastography*

An analysis was performed to determine whether there were relationships between the histological intactness of the tissue and the SWE data:

- Student's t-test for the slope coefficient was performed to determine whether there was a significant correlation between changes in stiffness and tissue disintegration. The null hypothesis is that the coefficient $H_0: \beta 1 = 0$ indicating no significant relationship between the regression analysis variables, with the alternate hypothesis $H_1: \beta 1 \neq 0$ with a=0.05.
- A receiver operating characteristic curve (ROC) was constructed to determine the utility of SWE as a predictor of complete lesion formation. Lesions with average tissue destroyed (%) greater than the threshold value determined from the histological quantitative analysis and correlated with the qualitative analysis were deemed a fully homogenized lesion. The area under the curve (AUC) was calculated to determine the predictive value of SWE. The optimal threshold/cutoff was determined by using Youden's *J statistic*, which captures the performance of the classifier. It is given by the following formula.

$$J\ statistic = TPR + TNR - 1 \qquad (5.6)$$

and has a value between 0-1. The index was calculated for all the threshold points on the ROC curve, and the maximum value of the index was used to determine the cutoff point.

5.3 RESULTS

In this study, we explored different parameter sets across cavitation CH and BH as described in Table 5.8 at various doses to treat ex-vivo human prostate samples (N=23) obtained from patients undergoing simple prostatectomy procedures for BPH using an IRB exempt tissue procurement protocol (NWBiotrust, Seattle, WA). Two different transducers were used to deliver the respective therapies with image guidance provided by in-line off-the-shelf commercial imagers. Shear wave elastography (SWE) was used to measure tissue stiffness before and after treatment to assess the treatment outcome and the tissue was later fixed and sent to histology for Masson's trichrome staining. Additionally, a novel processing algorithm was developed, named the Histotripsy Lesion Quantification by Entropy analysis (HLQE) to quantify the lesion as a direct measure of the treatment outcome.

During treatment, bubble clouds appear as hyperechoic regions on the B-mode, with no significant change in appearance of tissue at lower treatment dose**.** Figure 5.2(a), (b) summarizes the appearance of a complete lesion generated by BH across the B-mode and SWE. In B-mode, the fully developed lesion appears as a hypoechoic zone, which is also reflected in the shear wave image, where there is a clear contrast in the colormap. Shown in Figure 5.2(c) a representative image of Masson's trichrome stained section with lesion site identified. Figure 5.2(d) shows the performance of the HLQE algorithm in identifying the lesion and calculating the % destroyed tissue. The top row of (d) shows the binary image produced from thresholding the entropy calculated across the lesion grid, with the bottom panel showing the superimposed binary image onto the actual histology slice, with red outline representing the lesion area. There is a slight difference in the lesion outlines between imaging modalities and histology, partially due to shrinkage of tissue during formalin fixation and artefacts during processing for staining.

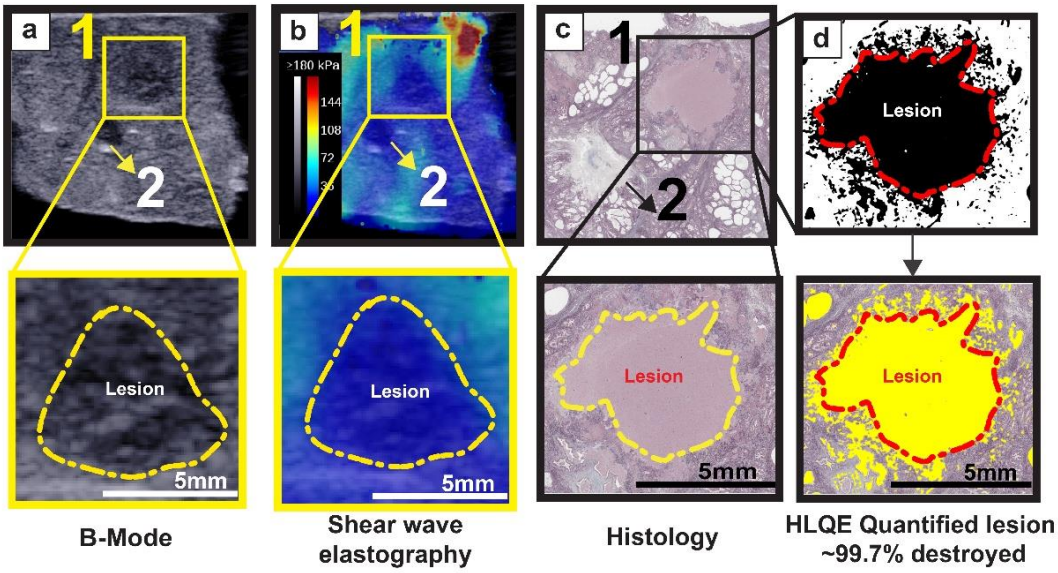

Figure 5.2. Lesion visualization modalities: (a)-(c) show the lesion appearance across B mode, shear wave elastography and histology. Identified here are two treatment areas with grid 1 receiving BH at 60s and grid 2 receiving BH at 30s. Both treatment grids can be visibly identified (by the yellow/red outline) and are distinguishable on all the modalities. (d) binary map of the lesion identified by the HLQE algorithm and superimposed on the histological slice.

5.3.1 *Histological evaluation*

Both qualitative and quantitative metrics were evaluated across all treatment parameter sets and dose. Figure 5.3(a) presents a detailed picture of the progression of tissue damage for each parameter set with an increase in dose. Panel (i) is Masson's trichrome stained slide with important treatment-related features. Panel (ii) shows the lesion map detected by the HLQE algorithm superimposed on the histology section.

Qualitative analysis.

With increasing dose, small, isolated regions of damage progress to contiguous larger lesions at higher doses. A fully homogenized lesion was observed at 288s for high-PRF CH, ≥144s

for the low-PRF CH and at ≥30s for the BH. All histotripsy parameter sets produced lesions with high fidelity to cover the entire intended area of treatment plan.

- *Lesion border distinction:* In both BH and CH treatments, a clearly distinguished lesion was found if the treatment was entirely within a glandular region of the tissue. Treatments in fibromuscular bands showed a lesion surrounded by a less distinct border with multifocal areas of homogenization and frayed collagen and muscle fibers. All BH treatments showed presence of frayed collagen within the lesion (blue arrows) at all doses, however in CH treatments they tend to appear less frequently at higher doses.
- *Globular collagen with increasing dose and duty cycle*: Globular collagen was observed in tissue treated with BH (1% duty cycle) at a dose of 30 s (Figure 5.3 (a) BH 30 and 60s. Some amount of globular collagen was also observed in the High-PRF CH treatments (duty cycle-0.21%) at 144s and more prominently at 288 s (Figure 5.3 (a) High-PRF CH (ii) 144 s and 288 s). However, in the low-PRF CH treatments, globular collagen was not observed.
- *Tissue fragments:* In BH treatments, collagen and muscular fragments were present for all doses. Across both CH parameter sets, tissue fragments were only identified at higher doses(≥144s). In fully homogenized treatments, they were <50μm.

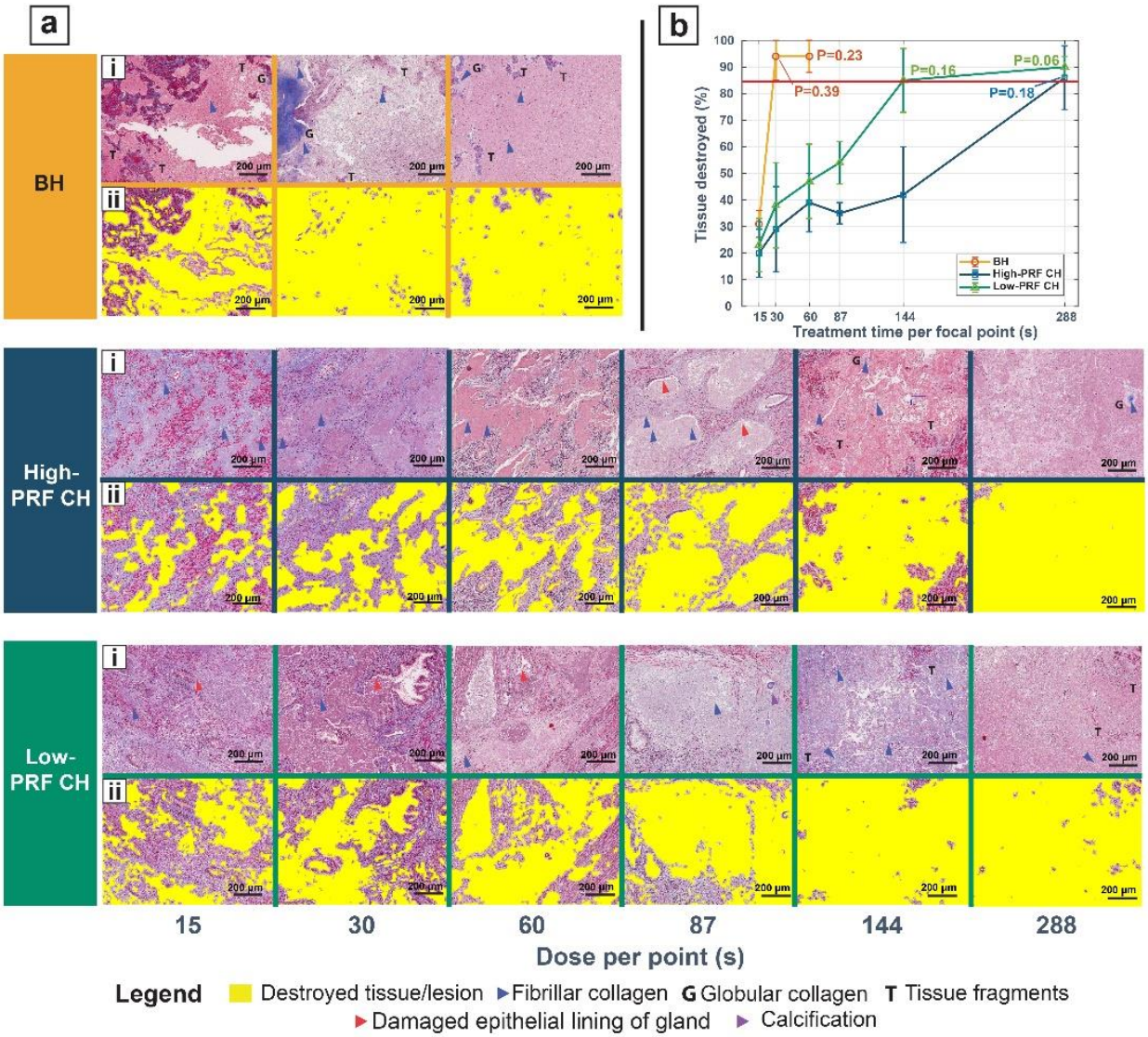

Figure 5.3. The appearance of histotripsy treated prostate by histology. (a)(i) shows the Masson's trichrome stained sections of EVHP samples subjected to various exposure parameters and treatment times. The blue arrows indicate the presence of intact fibrillar collagen, with "G" indicating globular collagen, "T" pointing to tissue fragments. Red arrows point to the damaged epithelial lining of the glands. a(ii) is the superimposed lesion image detected by the HLQE algorithm. (b) Average percentage of tissue destroyed across different doses (time per focus) based on areal analysis of the histological sections using the HLQE algorithm. **p-values* for the one sample t-test, where the population mean is statistically indistinguishable from a mean value= 100%. The red line indicates the minimum average tissue destroyed (%) set as the minimum threshold required to classify as a complete lesion.

Quantitative assessment, areal analysis.

The percentage of tissue destroyed with each parameter set and dose is summarized in Figure 5.3(b). BH destroyed a greater percentage of tissue within the measured ROI, at a lower dose, followed by the low-PRF and high-PRF CH parameter set. The results of a one sample t-test annotated in the same figure indicate the dose at which the average tissue destroyed (%) was statistically indistinguishable from 100% destroyed for each parameter set. For BH, this was at 30s with 94±9% of the tissue destroyed. Approximately 85±12% of the tissue was destroyed with the low-PRF CH at 144 s, and approximately 86±12% was destroyed with the high-PRF CH at 288 s. The minimum average tissue destroyed (%) across all parameter sets and dose for a complete lesion was measured to be ~85%, which was set as the minimum threshold, as highlighted by the red line. All the treatments above this threshold were also correlated with the qualitative analysis findings to determine that the treatments were complete.

5.3.2 *Shear wave elastography analysis*

Pre-treatment sample stiffness

The allocation of the treatment dose and modality in each sample was randomly assigned. However, the pre-treatment stiffness for the low-PRF CH treatments were significantly higher than the high-PRF CH and BH ($P<0.001$), as indicated by a 2-tailed 2-sample t-test (Figure 5.4 (a)).

Summarized in Figure 5.4(b) is the pre-treatment stiffness sorted by dose for each parameter set. For BH, the mean pre-treatment stiffness was 37±27.3(s.d.) kPa, with a median value of 26.16 kPa and an IQR=22.3-41.6 kPa. For the high-PRF CH treatment group, the mean stiffness was 53.2±31.6(s.d.) kPa, with a median value of 46.4 and an IQR of 28.6-72.4 kPa. For low-PRF CHs, the mean pre-treatment stiffness was 88.2±43.3(s.d.) kPa, with a median value of 96.5 kPa and an IQR=56 -118.6 kPa.

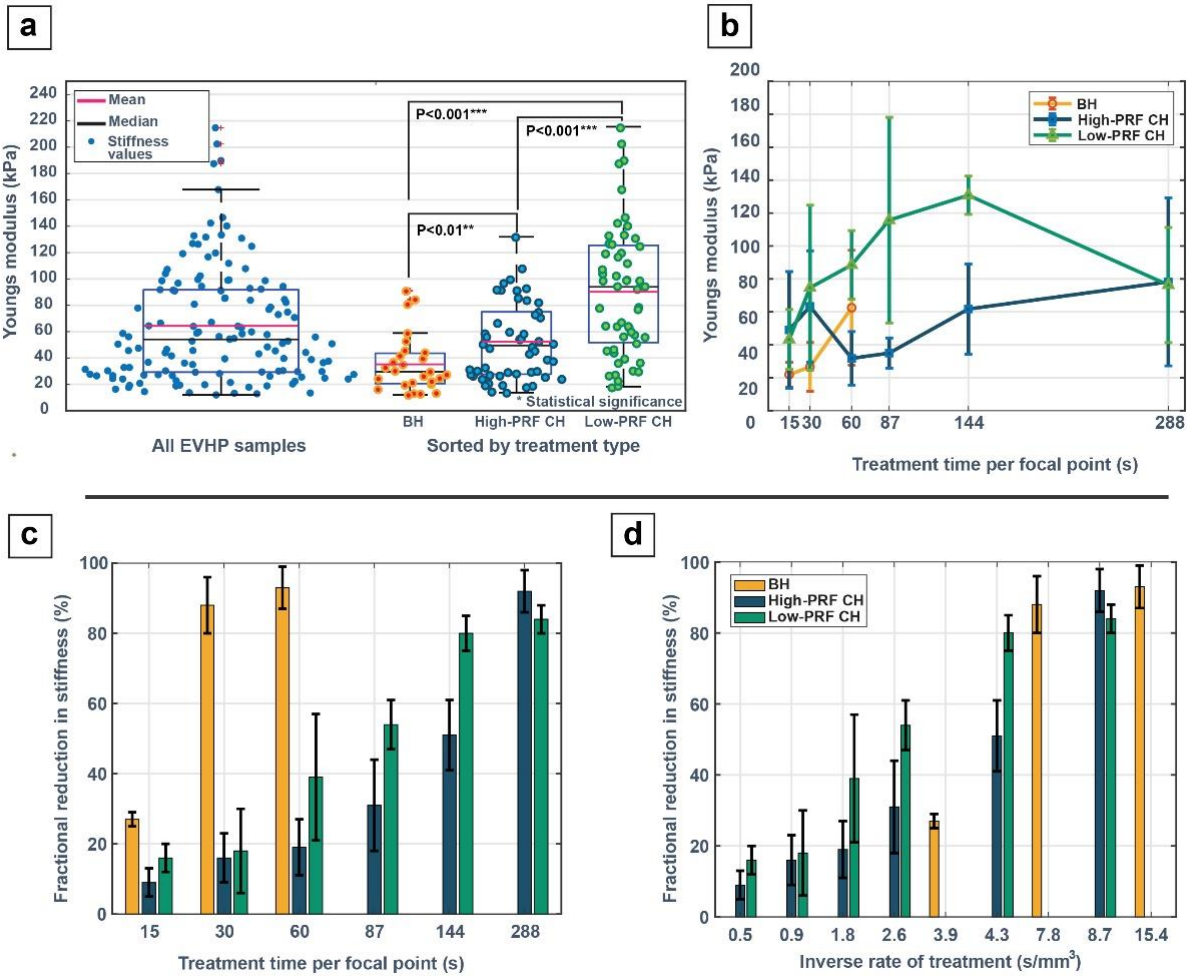

Figure 5.4. Shear wave elastography measurements (a) Pre-treatment young's modulus (stiffness) of all the EVHP samples across all treatments segregated based on the treatment parameter set. *p-values* were derived from a 2-tailed 2-sample t-test. (b) The pre-treatment stiffness of the slices that represent the center of the lesion segregated by dose and treatment parameters (c) Reduction in stiffness percentage post-treatment as a function of dosage (treatment time per grid point) and (d) Reduction in stiffness percentage post-treatment normalized by the individual transducer focal volume. The purple line indicates a SWE threshold that corresponds to complete lesion homogenization.

Post-treatment stiffness change analysis:

Post-treatment, SWE measured stiffness was reduced within the histotripsy treatment area with a clear contrast in the shear wave color map and a corresponding hypoechoic region observed on the B-mode for sufficiently long treatment times Figure 5.4(c) shows the fractional reduction data across all the parameter sets at every dose. At the histologically identified complete lesion dosage points, towards the center of the lesion the change was -88.4±8.5(s.d.) % at 30 s for BH, while it was -91.6±6.0 (s.d.) %. for the high-PRF CH at 288 s and -79.9±5.4 (s.d.) % for the low-PRF CH at 144 s.

Due to the different focal volumes of the CH and BH transducers respectively, it is difficult to directly compare volumetric treatment rates for these data. Nonetheless, we approximately estimated the rates based on the volumes treated and time required to achieve a complete ablation for the entire lesion. The inverse rate of treatment (time per unit volume for the specific treatments) plotted as a function of the fractional reduction in the stiffness percentage, is shown in Figure 5.4(d), where the stiffness data was normalized by the individual transducer focal volume to estimate the rate for these specific treatments**.** This translated to a rate of 13.9 mm^3/min for low-PRF treatments followed by BH at 7.7mm^3/min and high-PRF treatments at 6.9mm^3/min.

5.3.3 *Regression analysis between histological analysis and shear wave data*

Regression analysis was performed to compare the destroyed tissue percentage vs. the stiffness reduction via SWE, and the results are shown in Figure 5.5(a), with $R^2 = 0.87$ and a t-test of the slope coefficient where P<0.0001*, indicating a significant relationship between the two parameters. The individual scatter points are also indicative of three clusters, with green cluster representing completely fractionated lesions and the red, yellow clusters representing progressing partial lesions.

The ROC curve generated to determine the relative predictive strength of the SWE measurements for the assessment of tissue disintegration is shown in Figure 5.5 (b). The area under the ROC curve (AUC) was 0.98, which indicates the high performance of the classification criteria based on the SWE threshold in distinguishing full lesions from partial lesions. The Youden's J statistic calculated as 0.97 further captures the performance of the dichotomous test, where a higher value is considered better. From the J statistic, the optimal threshold for stiffness reduction was identified as 75% from a premeasured value. These two observations emphasize that shear wave-based feedback can be a reliable indicator of a histologically observed lesion.

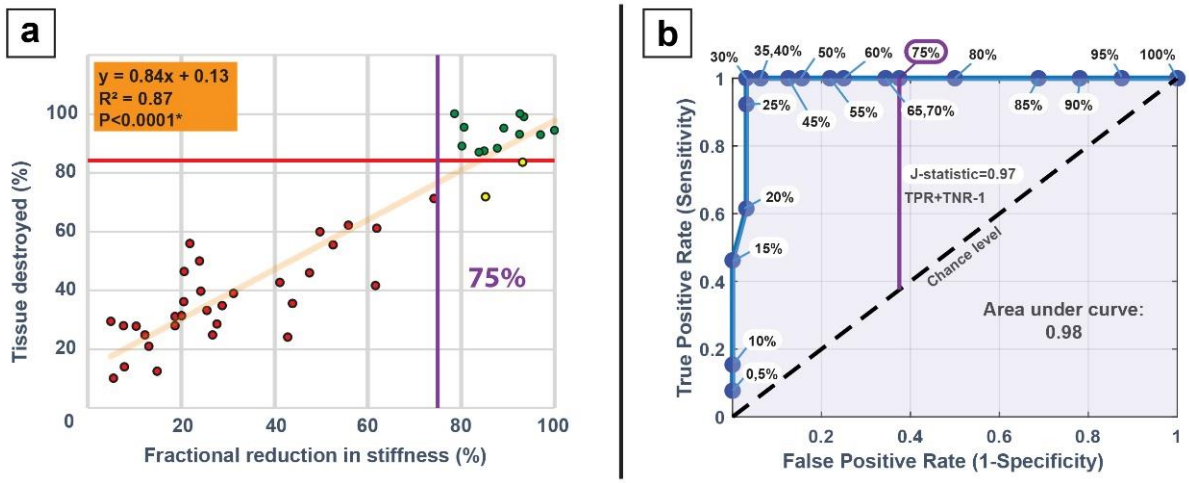

Figure 5.5. Regression analysis of shear wave and histology measurements: (a) Linear regression analysis between the shear wave reduction stiffness and homogenized tissue percentage quantified using the HLQE algorithm. The red line indicates the 85% threshold calculated from histological assessment from prior section which is the minimum average tissue destroyed (%) across all parameter sets and dose for a complete lesion. The red cluster represents completely fractionated lesions, with yellow, red clusters representing partial lesions. (b) An ROC curve was constructed for every shear wave threshold, with the Youden's j statistic predicting a 75% reduction in stiffness pre-post as measured by shear wave to be a good indicator for histologically observed complete lesions.

5.4 DISCUSSION

Previous histotripsy studies of BPH examined parameters and dose in a dog model[51], but the canine prostate tends to be predominantly glandular; therefore, the identified treatment may be an underestimate of the actual dose needed in humans. This may also explain some of the inefficacy of the results in a pilot clinical trial[152] using histotripsy to treat BPH. As such, this work is a step toward understanding how to optimize parameters to ablate fibrotic or fibromuscular tissue more rapidly and to evaluate treatment monitoring techniques for predicting successful treatment completion. This study compared the dose effects of different parameters of cavitation cloud histotripsy and boiling histotripsy in mechanically ablating *ex vivo* human benign prostatic hyperplasia tissue. Although a substantial body of literature exists on testing histotripsy modalities with different parameters, few studies have compared the ablation efficacy of different modalities for a single tissue type. Additionally, *in vitro* and *in vivo* data indicate the differential susceptibility of different tissues to a given set of parameters. For example, Vlaisavljevich et al demonstrated that mechanically tough tissues require a greater dose to completely erode than soft tissues[155,156], which was also observed in cholangiocarcinoma[33] and uterine fibroid[34] treatments. BPH tissue is a heterogeneous mixture of soft glandular tissue and tough fibromuscular tissue, the composition of which can vary widely between patients.

All three parameter sets produced complete ablation at sufficient doses. On a point-by-point basis, the BH parameters tested here produced liquefaction more rapidly. This may be related to the high duty cycle of this treatment (1%) compared to that of the other parameters (0.2% for high-PRF CH and 0.03% for low-PRF CH). However, the difference in focal volumes between the BH and CH transducers and scanning parameters limit our ability to conclude whether these are more effective volumetrically. Through an analysis where we estimated the volumetric treatment

rates, low-PRF CH parameters produced a greater rate than both BH and high-PRF CH. The volumetric rate for BH estimated in this study is consistent with a recently published study involving treating the *ex-vivo* human prostate with similar BH parameters[30]. The total exposure time per point for each parameter set, calculated as

$$Exposure\ time(s) = Time\ duration(total\ ablation) * PRF * Cycles * f \quad (5.7)$$

Where *f*=operating frequency of transducer, *PRF* – Pulse repetition frequency, is as follows BH=0.3s, high-PRF CH=0.617s and low-PRF CH=0.041s. Within the CH parameters there was a~15-fold difference between low-PRF and high-PRF indicating a large difference in efficiency. One potential explanation for these differences, as observed in our previous studies[53,154] is that high-PRF treatments suffer from cavitation memory effects, an observation also mentioned in other studies[157–159]. The bubbles generated from the previous pulse persist for longer durations in tougher media [53] before completely dissolving. If a second pulse arrives prior to the previous bubble dissolution, it cavitates bubbles in the same location. This can lead to sparse cloud formation with only isolated small regions of damage. Low-PRF CH, on the other hand, creates denser clouds that nucleate bubbles in different locations with each pulse, due to sufficient time for the bubbles to dissolve, and therefore cover the volume of the tissue to form a more complete homogenate lesion faster. A potential reason for estimating the volumetric rate as described in this paper versus estimating from histological slides, was due to artefacts in tissue processing for staining including tissue shrinkage that occurs during the fixation process. Another challenge with comparison is that despite randomization of the treatments, the initial stiffness of the tissue on average for the low-PRF treatments was considerably higher than that of the BH parameters or

high-PRF CH parameters. Also, BH treatments had a slightly higher overlap, about ~70% in comparison to CH treatments at ~50%, meaning a slightly higher dose per unit area; therefore, the actual efficacy of low-PRF in comparison to BH could be underreported. Despite these challenges, it is clear simply from the comparison of the two sets of CH parameters that the efficacy of treatment for fibrous BPH tissue can be significantly improved with the use of parameters different than those attributed to early BPH studies, indicating a need for optimization of parameters for this application prior to clinical trials.

Thermal effects were seen with both BH and high-PRF treatments. This was validated by the presence of globular collagen that is consistent with findings from Wang et al [160], when using higher duty cycle BH pulses. At the lesion borders, there was presence of frayed collagen, similar to BH outcomes of treated *ex vivo* prostate cancer samples [148], and we also observed some thermal damage in the form of blanched tissue at the outer rim of the lesion which was reported in other studies using 10ms pulses[160,161] BH parameters. There was also an increased presence of tissue fragments possibly due to the vapor cavity created by the boiling bubble leading to an acoustic fountain effect that causes tissue disruption into several smaller fragments[9]. Broken collagen and muscle fibers make up the composition of these fragments, indicating origins from predominantly fibromuscular treatments. In treatments primarily positioned in glandular areas, tissue fragments were rarely observed, as they tend to completely homogenize. The CH parameters displayed reduced evidence of thermal effects, but the presence of more globular collagen in the high-PRF treatment group was potentially due to the increased duty cycle used in this study and the greater dose for liquefaction.

Shear wave elastography was found to be well correlated with lesion progression histologically and may be a valuable tool to determine treatment completion in the clinical setting.

SWE estimates the Young's moduli of the prostate samples with high accuracy[162], and the values reported here are consistent with those reported from transrectal SWE in patients[163–165]. From the *ex vivo* studies, we encountered samples with different initial stiffnesses, and a similar variance is expected in a clinical scenario. Along with attenuation and aberration affecting the acoustic pressures achieved *in situ* at the focus, the homogenization rates will differ for each treatment. It is therefore essential to obtain feedback to assess the progress of treatment to provide an opportunity to adjust the dose for each location, to optimize treatment. B-mode provides only qualitative feedback, and it can be difficult to track the hypoechoic treated region due to the presence of hyperechoic bubbles that can persist for longer time intervals. Recent studies have employed Doppler-based measurements[166,167] that track the speed and direction of cavitation bubbles as an indicator of homogenization, and may also offer quantitative information. Accounting for different starting conditions, we found a threshold of >75% reduction from the initial stiffness to indicate complete histologic disintegration. This feedback can allow optimization of treatment times specific to each case. One of the inherent limitations of shear wave measurements in an *ex vivo* setting is that saturation effects arising due to solid tissue and liquid boundary artifacts tends to overestimate the stiffness if the size of the sample is too small, thus we were careful to avoid treating near such boundaries.

In this study, we also successfully showed the utility of an entropy-based analysis for the quantification of lesions in Masson's trichrome images to better assess the treatment effects for future treatment planning. Computationally, the algorithm identified lesions in $\sim<$ 1 minute compared to manual processing. Currently, there does not exist an automated segmentation methodology for differentiating homogenate lesions from tissue based on texture, and the HLQE algorithm can also be extended for the analysis of other stains to look at damage patterns.

One limitation of this study is the variation between size and shape of samples that necessitated treatment of different volumes of tissue. However, the dose per focal volume was constant between samples, and this variance is not expected to affect the measurements made since the minimum grid size was still large enough to perform shear wave elastography and histologic analysis. Future studies will aim to use a more uniform grid size to quantify the true treatment area vs the intended area. We aim to carry out a more direct comparison across several histotripsy parameters and strategies[61 168] using hardware that can perform both BH and CH at a constant duty cycle, varying the PRF and pulse duration, and potentially through a transrectal approach[66] that can circumvent the challenges associated with delivering ultrasound through a transperineal/transabdominal approach.

To summarize, we compared homogenization of tough fibrotic human *ex vivo* benign prostatic hyperplasia tissue via three different sets of histotripsy treatment parameters at varying doses. The results demonstrated that alternative treatment parameters can achieve more rapid ablation of BPH tissue compared to those attributed to previous BPH studies. This work also established the utility of shear wave elastography as a reliable tool for obtaining feedback during treatment to determine the endpoint. A threshold reduction in SWE-measured stiffness for of approximately 75% [3] was found to correlate well with complete lesion formation. These results and feedback offer strategies to achieve more efficient treatment of BPH tissue by histotripsy in future trials.

CHAPTER 6. TREATING FIBROUS TISSUE MIMICKING DOUBLE NETWORK HYDROGEL PHANTOMS USING HISTOTRIPSY: A PARAMETER STUDY

6.1 INTRODUCTION

Tissues with higher stiffness and tough tissues are resilient to histotripsy and often require a higher number of pulses to disintegration[156,169]. Following a successful pre-clinical study[51], a clinical trial with histotripsy attempted to treat human benign prostatic hyperplasia tissue [52] by a transperineal approach, but did not achieve any objective improvements. Since then, researchers have employed various modalities of histotripsy discussed, in treating fibrous tissue. For example, uterine fibroids [39,170], cholangiocarcinoma [33], prostate cancer [171], human BPH, [66,148,172] and bladder wall[40] have been treated *ex vivo*. This was achieved using different transducers with varying f-numbers, operating at different frequencies and duty cycles, and requiring different doses. However, these variations make direct comparisons challenging and complicated the determination of which parameter has the most significant impact on effectively treating a given tough tissue. It is well-documented that histotripsy outcomes can vary significantly based on tissue stiffness and frequency[56,169]. Additionally, bubble activity is influenced by factors such as pulse repetition frequency[57] and the f-number[84] of the transducer used.

Past research has focused on understanding the mechanisms of ablation by studying the bubble cloud characteristics in RBC agarose phantoms[55], [56,57,173,174], and polyacrylamide phantoms [175],[142]. However, from our previous study (Nanda Kumar et al[53]) we noted that while these

---

**Manuscript in preparation for submission to IEEE Transactions on Biomedical Engineering.*

phantoms are stiff, they do not accurately represent tough fibrous tissue or its typical response to sonication. This highlighted a gap in knowledge, where comparing different parameters and their outcomes in a fibrous tissue-mimicking phantom was necessary. Further optimization of histotripsy for effectively liquefying fibrous tissue within a clinically relevant timeframe is crucial, particularly for debulking applications.

In this study, we aim to use the double network hydrogel made from a polyacrylamide and alginate hybrid, and build on top of our existing findings [53,154,172], by sonicating these phantoms using different parameters spanning all histotripsy modalities, but delivered by a single transducer operating at a fixed frequency, constant duty cycle, and multiple doses, to accurately evaluate the effects of these parameters on liquefaction outcomes. The use of high-speed photography to study the bubble dynamics will aim to further assist our understanding of this respective outcome. We hypothesize that these phantoms will respond differently in comparison to the agarose or polyacrylamide phantoms, but will accurately mimic the outcomes as reported in some of the ex-vivo tissue studies.

6.2 METHODS

6.2.1 *Gel Phantom*

Double-network hydrogel phantoms, composed of a 90:10 weight ratio of acrylamide to alginate, were selected for these experiments due to their stiffness range of 62.77 ± 7.28 kPa, which closely matches that of common tough fibrous tissues found in conditions such as benign prostatic hyperplasia and uterine fibroids. These phantoms were fabricated following the methods detailed in our previous work on gel phantom preparation (Nanda Kumar et al.[53]) with an increased thickness of approximately 30 mm to encompass the focal beam fully. To accommodate the

increased thickness and enhance user safety during gel pouring, the following modifications were made to the original process:

- Crosslinking agent adjustment: N,N′-Methylenebisacrylamide, the crosslinking agent for polyacrylamide, was originally obtained in powder form. A 1% liquid solution was then prepared, and the required quantity was measured to be mixed with the gel mixture, as described in our previous work [53]. However, this was replaced with a commercially available 2% liquid solution (M1533) from Sigma Aldrich Inc. (St. Louis, MO, USA), with corresponding adjustments made to the final volume calculations. Table 6.9 provides the exact quantities required to prepare 200 g of 90:10 acrylamide-alginate gel for convenience.

Table 6.9. Sample weight and volume measurements for preparing 200 g of 90:10 polyacrylamide-alginate gel

Chemical name	**Final quantity**
De-ionized water	103.96 ml
Acrylamide (40% solution)	63 ml
Sodium alginate	2.8 g
Ammonium persulfate (APS)	From 1% solution, 4.3 ml
N,N-methylenebisacrylamide (MBAA)	From 2% solution 0.76 ml
N,N,N',N'- tetramethylethylenediamine (TEMED)	91 µL

A 1-M solution of $CaSO_4.2H_2O$ is prepared by mixing 136.14 g in 1L of de-ionized and degassed water.

- Since these gels were thicker than the ones used in the previous work, the $CaSO_4.2H_2O$ cross-linking time was increased from 48 to 72 hours to ensure complete crosslinking. Post

cross-linking, the gels were left in a vacuum-sealed humid box for an additional 48 hours to stabilize the reactions and achieve a homogenous stiff gel.

6.2.2 *HIFU equipment*

Histotripsy treatments were performed using a single 12-element 1 MHz transducer with a radius of curvature 65mm and an aperture of 90mm, with a f-number of 0.72. The transducer has a central opening of 28mm to co-axially mount an imaging transducer (3PE, 134 Humanscan, Gyeonggi-do, South Korea) connected to a Verasonics system (V-1 Ultrasound Acquisition Platform, Verasonics Inc., Kirkland, WA, USA) operating in B-mode at 3 MHz, for guidance. The setup was driven by a custom Class D amplifier powered by a high voltage source (TDK Lambda GENH600-1.3) and controlled using an FPGA board (Altera DE0Nano Terasic Technology, Dover, DE, USA).

Transducer characterization: Focal pressure measurements of the transducer were performed using a fiber optic hydrophone (FOPH2000, RP Acoustics, Stuttgart, Germany) at a variable duty cycle, with increasing input source voltage before cavitation at the fiber tip occurred. Non-linear simulations were performed using the HIFU beam software, which solved the Westervelt equation using a Wide-angle Pade approximation(WAPE) (Yuldashev et al [80]) to compare against FOPH measurements and estimate the in-situ focal pressure at input source voltages used for treatments beyond the hydrophone measurable range. Linear beamwidth measurements were taken using a needle hydrophone (Precision Acoustics, Dorset, United Kingdom) with a 75µm active area at lower voltages to estimate the -6dB beamwidth.

6.2.3 *High-speed camera, pulse parameters, and experimental setup*

The transducer was submerged in a tank filled with degassed and deionized water, and its position was fixed. The double network hydrogel was placed onto a fixture mounted to a 3-axis motorized positioner with linear slides driven by lead screws and a stepper motor (Bislides and VXM controller, Velmex, Inc., Bloomfield, NY, USA). The gels cast in cylindrical beakers were further embedded in a 1.5% UltraPure^{TM} Agarose (Thermo Fisher Scientific, Waltham, MA, USA) phantom prepared as described in our previous article [53]. The camera (Photron Fastrax APS-RX, Photron, San Diego, CA, USA), paired with a ZEISS Makro-Planar T* 100mm f/2 ZE prime lens (ZEISS Corporation, Hebron, KY, USA) with an additional bellow, was set up in an orthogonal plane to the acoustic travel. An LED light source driven by a current-controlled DC supply was placed on the opposite side of the camera, providing a backlight. A collimating lens further focused the light from the LED source, and a diffuser was used to provide uniform illumination (Ambekar et al [176]). The lens's aperture was adjusted such that the camera's depth of field was set to 3mm. A PC was used to record video from the high-speed camera using the Photron FASTCAM Viewer (PFV4) software. The PC also controlled the 3-axis positioner and programmed the pulse parameters onto the FPGA through MATLAB (Mathworks, Natick, MA, USA). The setup is shown in Figure 6.1.

A total of 5 pulse parameters were tested in this study, with the duty cycle kept constant at 1%. The pulse repetition frequency (PRF) was changed from 1Hz to 1000 Hz, and the number of cycles (Pulse Duration PD) was interchanged from 10000 cycles to 1 cycle. Different doses were also examined that ranged from 30,60 and 120s per point, and this was chosen based on the results from our previous *ex vivo* prostate study [54,172], where 30s was identified as the minimum dose at which complete liquefaction of the prostate was observed with longer pulse durations. A

compilation of the pulse parameters and the camera acquisition settings are summarized in Table 6.10

Table 6.10. Pulse parameters and camera acquisition settings.

Parameter No	**Pulse repletion frequency (Hz)**	**Pulse Duration (cycles)**	**Camera frame rate (FPS)**	**Camera shutter speed (us)**	**Dose (s)**
1	10000	1 (1μs)	10000	2	30,60,120
2	1000	10 (10 μs)	10000		
3	100	100 (100 μs)	10000		
4	10	1000 (1ms)	10000		
5	1	10000 (10ms)	1000		

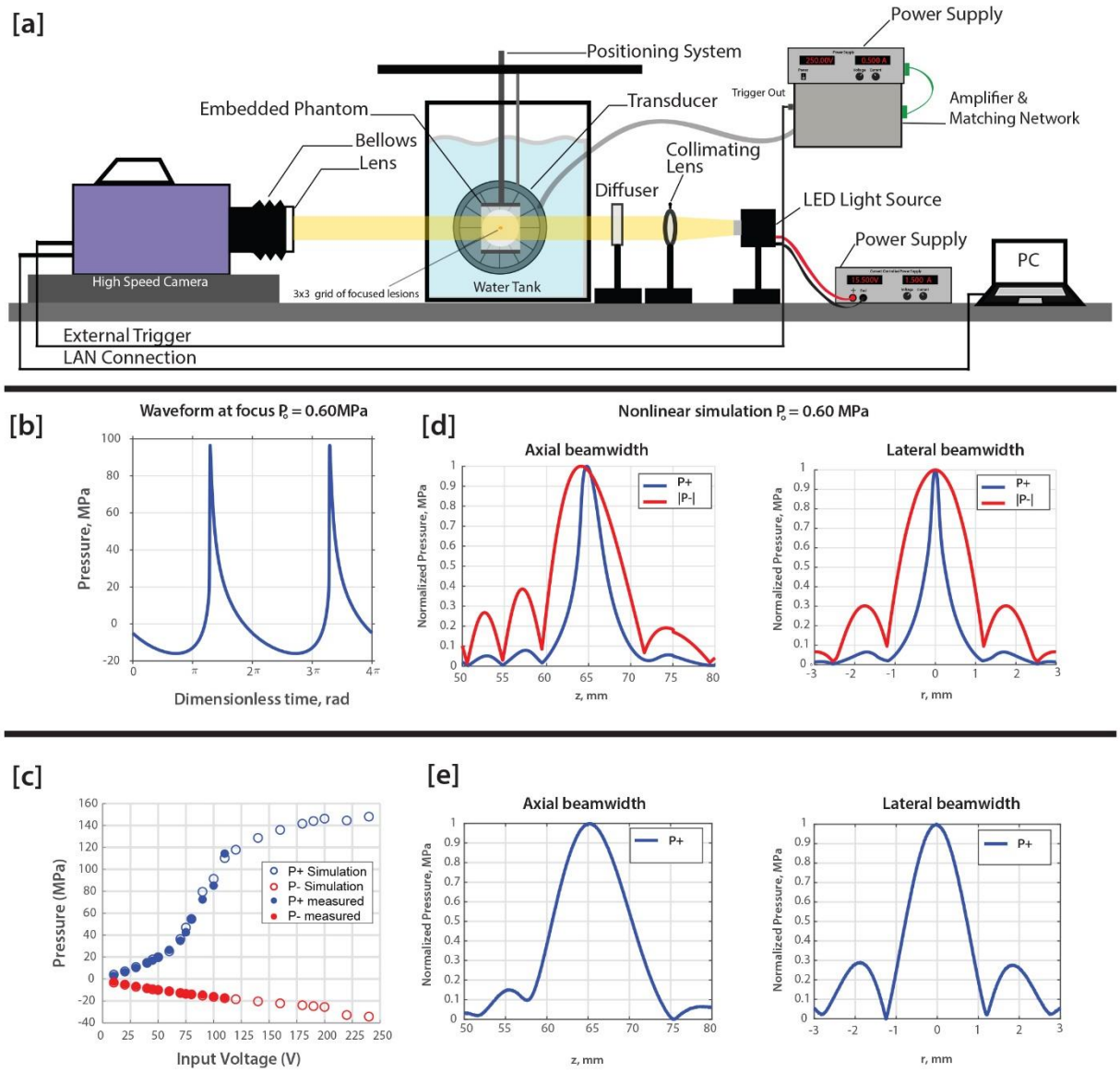

Figure 6.1. (a) High-speed camera and experimental setup. (b) The FOPH waveform was recorded at an input source voltage of 100V and used for most treatments (except 1-cycle treatments). The waveform was almost shocked. (c) Fiber optic measurements and nonlinear simulations from HIFU Beam software (d) Normalized beamwidth simulation (nonlinear regime) at the input source voltage of 100V translates to a source pressure of 0.60 MPa. (e) Needle hydrophone measurements of the field with the transducer operating in the linear regime at low input source voltages were used to estimate the -6dB beamwidth.

6.2.4 *Ablation experiments*

Single point lesions: The goal of these experiments was to study bubble cloud evolution and characteristics as a function of the different parameters, using high-speed camera at different doses and correlate with lesion outcomes, the methods of which are similar to our prior publication[154]. n =3 single-point treatments for every parameter and dose were performed in 4 gels encompassing multiple treatments. The input source voltage was set to +20% of the threshold at which consistent cavitation was seen as the voltage was ramped up.

A delay of 44.79 μs was added to the different pulse duration for every parameter used in this study to take into account the travel time for the pulse train to arrive at the focus. The shutter speed was set to 2 μs with a frame captured exactly at the end of the pulse train arriving at the focus, and this was done for every 1s of treatment. This made sure a similar frame was captured across all parameters tested. Different frame rates were adapted which also meant there were different capture resolutions across parameters. The images were post-processed to include a frame size spanning 512(width)x256(height) pixels. The resolution of the video frames was 33.2 um/pixel.

Grid ablation: These experiments aimed to assess the minimal dose at which complete liquefaction can be achieved by the different parameters at the fastest rate possible. A total of n=3 treatments for every parameter and dose were performed on cuboidal phantoms suspended directly in the fixture without agarose embedding. Each treatment grid size was 3x3 points applied in a raster scan and an overlap of 0.75mm, which is half of -6dB lateral beamwidth. Treatments were performed at +20% of the threshold at which consistent cavitation was observed. B-mode, SWE stiffness change, and phase contrast microscopy measured post-treatment outcomes.

Post-treatment, several methodologies were employed to measure the treatment outcomes both qualitatively and quantitatively, as described in the sections below.

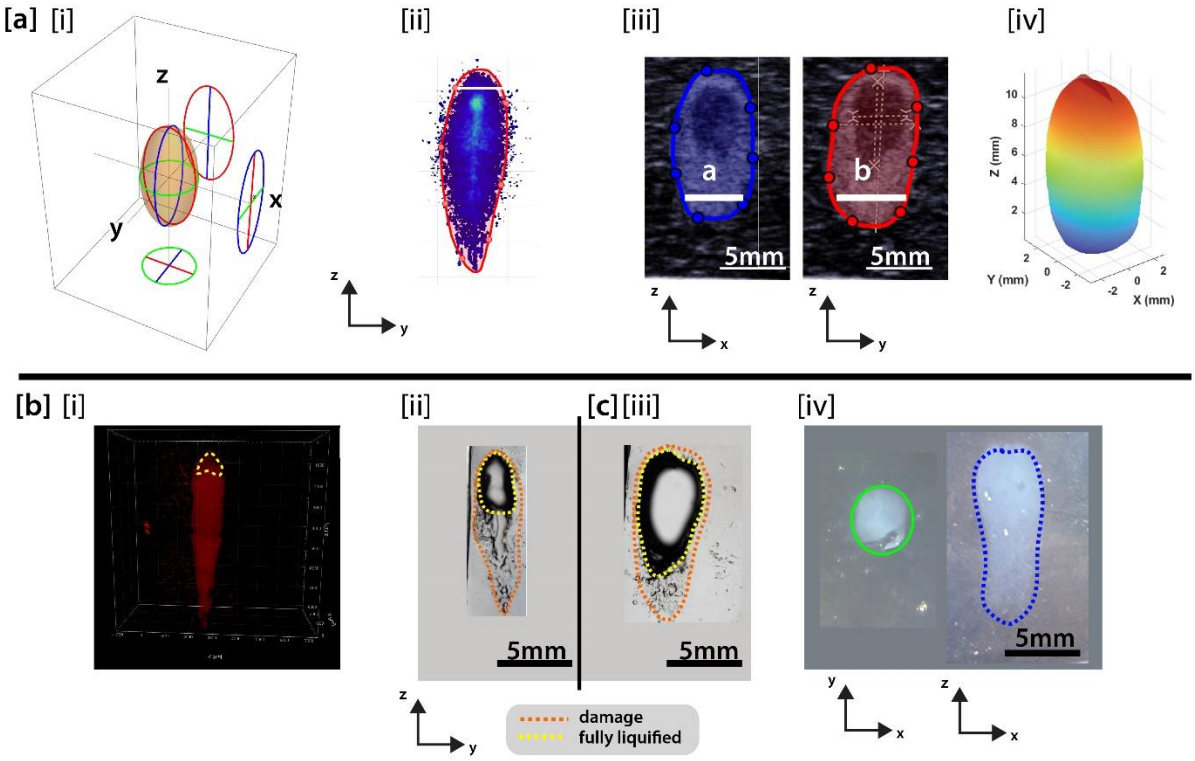

Figure 6.2. (a) A representation of the different planes from which volume estimates were made (ii) Cumulative bubble cloud image (iii) B-mode scan in two orthogonal planes, and (iv) a reconstruction of the 3D volume from the integrated individual areas. (b) (i) 3D rendering of the OTLS scan from Imaris viewer with the circled yellow region shows fully liquified areas similar to what was seen on (ii) phase contrast imaging. (c) (iii) represents a volumetric treatment lesion seen in phase contrast imaging, with the fully liquified volume circled in yellow and total damage area in orange. (iv) A bench top illumination of the same lesion is shown from two different planes.

6.2.5 *Qualitative assessment: Phase contrast imaging:*

An advantage of using these double network hydrogels was the ability to assess damage using phase contrast microscopy, as shown in Nanda Kumar et al [53]. Damaged areas, as well as fully

liquified areas, show phase variations, which resolve with a darker background in comparison to intact gel, thus enhancing the contrast and helping to identify the regions distinctly. An example of the lesion is shown in Figure 6.2c, along with a representation of the same lesion by benchtop illumination. The gels were sectioned along the midplane of the lesion and visualized on a Nikon Eclipse 80i at 2x magnification with a phase contrast filter. A series of images were captured through NIS elements (Nikon Instruments Inc., Melville, NY, USA) and stitched to visualize the full cross-section of the lesion. A qualitative assessment was then performed to determine the treatment outcomes of the different parameters and dose.

6.2.6 *Quantitative assessment: Bubble cloud characteristics:*

The bubble cloud videos from the single point lesions were analyzed in MATLAB, after binarizing them using a custom algorithm from (Nanda Kumar et al [154]). Frames were processed that represented every 1s of treatment progression. For every frame processed, the total bubble area was calculated along with a Pearson correlation coefficient between successive frames. Additionally, the cumulative bubble area was calculated by adding the binarized frames across the total duration of treatment to track the spread of the bubble cloud evolution and the number of occurrences of the cloud at a given location throughout the treatment. A series of probability measurements were made by grouping the total number of pixels (bubble area) that fall within the quartiles between 0 and 1, with 1 meaning a bubble appearing in all the frames for a given location. The percentage area of the pixels falling in the top two categories that, when summed, represent the area with a $P>0.5$, and along with the Pearson correlation coefficient, was useful in determining which parameters had a profound cavitation memory effect.

Plotting considerations: In Figure 6.4, the cumulative bubble area representation's color bar was set to 120s across all 30, 60, and 120s treatments. In Figure 6.5, the bubble area and correlation

coefficient were plotted using n=9 samples averaged for t=30s, which included data from the first 30s of treatment from t=60s and t=120s samples, and n=6 samples averaged for t=30-60s, which included data from the t=120s treatments.

Volume estimation: The volume estimates were measured from the cumulative map at 30,60, and 120s. Historically, an ellipsoidal shape was assumed for making volume estimates, but a more accurate estimation method was needed with the clouds observed to be of a variable shape. In this study, we made this estimation based on fitting a mask complying with the cloud's shape. From this mask (as shown in Figure 6.2a), individual widths (a) along the Z axis (acoustic) at a single pixel resolution were estimated. Assuming an axisymmetric shape, the volume of the ellipse was calculated using

$$V \approx \int \frac{\pi}{4} * (a(z)^2) * dz \qquad (6.8)$$

Where $\mathrm{dz} = \text{single pixel resolution in mm}$,

6.2.7 *Quantitative assessment: OTLS imaging*

An open-top light-sheet (OTLS) microscopy system was investigated as a novel approach to nondestructively evaluate the single point lesions. The non-orthogonal dual-objective (NODO) arm of the OTLS system was used to capture volumetric datasets of lesions within the phantoms, achieving an isotropic resolution of approximately 4 μm[177]. The phantom gel was placed on a Teflon sample holder designed to match the refractive index of the water/gel (RI = 1.33). Lesions were imaged using a 488 nm laser in scattering mode (i.e., without an emission filter in the detection path). The captured images were stitched and fused using the BigStitcher plugin in ImageJ and saved as a TIFF file with a pixel sampling of 5.8 μm/px [178,179].

Volume estimation: The TIFF stack was further processed in FIJI ImageJ, an open-source processing platform [180] to estimate lesion (total damage) volumes. Once the TIFF stack was loaded into ImageJ, the frames were converted to 8-bit and then thresholded using the "Maximum Entropy Threshold". This technique is similar to the commonly used Otsu thresholding that maximizes inter-class variance, but the entropy thresholding maximizes the inter-class entropy, which performs slightly better by using textural analysis. Once thresholded, the total number of pixels representing damage across all the frames was summed and multiplied by the voxel volume (195.11 μm^3) to obtain the total damage volume. 3D reconstruction of the lesion TIFF stack was done using Imaris viewer (Oxford Instruments, Abingdon, UK) for visualization as shown in Figure 6.2b.

6.2.8 *Quantitative assessment: Shear wave stiffness and B-mode analysis*

The hybrid gels also display sufficient acoustic scattering for B-mode and shear wave elastography (SWE) analysis. On B-mode, fully liquified regions at a macroscopic level appear as a continuous hypoechoic region that is easily distinguishable, and partially destroyed regions appear hyperechoic. On SWE, this translates to a change in the Young's modulus (stiffness in kPa) in the damaged areas vs intact gel, which can be measured. Both B-mode and SWE maps were taken by suspending the gel in a container filled with degassed and deionized water. A 256-element linear transducer, SL 15-4 (Supersonic Imagine, Aix-en-Provence, France), connected to the AiXplorer system and operating with a bandwidth of 4-15 MHz was attached to a custom 3-axis manual positioner and brought closer to the face of the phantom. The transducer was set to a penetration mode, and B-mode and SWE maps were taken at a cross-section representing the center of the lesion in the x-z plane representing the lateral and axial acoustic axis. An additional

B-mode scan was taken in an orthogonal plane representing the y-z axis, to be used for volume estimations.

Stiffness change: The stiffness of the lesion proximal to the transducer was measured using a region of interest (ROI) ~= 2mm in diameter. In treatments with full liquefaction at a macroscopic level, this diameter would be consistent with the hypoechoic region on B-mode. All measurements were taken in a similar manner across all parameters. An additional measurement was taken in the untreated area and the percentage difference in stiffness between the untreated and treated areas were calculated and plotted.

Volume estimation: Two types of volume estimates were made from B-mode images, in a similar fashion to the estimation made from cloud images as described earlier in this manuscript. The total damage volume that encompassed both hyper and hypoechoic regions were estimated from the two B-mode scans taken in the x-z and y-z plane. A mask was drawn around the total damage, as shown in Figure 6.2a, and the width estimates ("a" along the y-z plane and "b" along the x-z plane) were made at a single pixel resolution along the z-axis. The final volume (V) was calculated using the equation below.

$$V \approx \int \frac{\pi}{4} * \big(a(z)\big) * \big(b(z)\big) * dz \qquad (6.9)$$

Where $\mathrm{dz} = \text{single pixel resolution in mm}$,

The same calculation was done for the fully liquified regions (hypoechoic zone) visualized at the macroscopic level on B-mode. The ratio of the fully liquified volume to total damage volume was also calculated.

Treatment rate estimation: Treatment rates were estimated from the visually observable fully liquified volume at a macroscopic level divided by the treatment times and were reported in mm^3/min.

6.2.9 *Statistical analysis*

ANOVA analysis: A one-way ANOVA was performed using JMP statistical software (SAS Institute, Cary, NC, USA) for the bubble area and untreated stiffness measurement. The null hypothesis was that the group means across parameters or dose was the same at significance level 0.05. If a significant p-value was measured, a post hoc analysis using Tukey's HSD was performed to identify which groups differed.

ANCOVA analysis: To compare the slopes of different regression lines plotted for total damage volume and fully liquified volume as a function of parameter and dose, an ANCOVA analysis was performed, specifically focusing on the parameter(cycle): dose(time) interaction term, which represented the slope. The data was grouped by parameters and individual group to group comparison was made with the null hypothesis at $\alpha=0.05$, that the slopes are same between the two parameters being compared.

Correlation of bubble cloud volumes to damage volume: The total damage volume estimates from OTLS and B-mode scans were compared to bubble cloud volume estimates using a matched-pair t-test grouped by parameters, with a null hypothesis ($\alpha=0.05$) stating that no difference exists between them. This analysis aimed to determine whether bubble cloud volumes could be directly equated to damage volumes.

6.3 RESULTS

6.3.1 *HIFU equipment: Transducer calibration and pressure estimation:*

The -6 dB beamwidth was measured using a needle hydrophone, yielding 9.8 mm axially and 1.51 mm and 1.48 mm on the lateral axes while the transducer operated in the linear regime at low voltages. Most treatments using 10–10000 cycles were conducted at an input source voltage of ~100V, which was +20% above the cavitation threshold, resulting in pressures of P_+ = 85.2 MPa and P_- = 15.8 MPa, as measured by the fiber optic hydrophone (FOPH). HIFU beam simulations estimated pressures of P_+ = 91.3 MPa and P_- = 16.3 MPa, closely matching the experimental values. However, when operating in the nonlinear regime, the beamwidth changed as the waveform began to shock. HIFU beam simulations at this 100V input source voltage estimated an axial beamwidth of P_+ = 3.4 mm, P_- = 8.4 mm, and a lateral beamwidth of P_+ = 0.47 mm, P_- = 1.80 mm. The theoretical time to boil for boiling histotripsy at this amplitude was calculated to be 1.97 ms. Pressure estimates from FOPH measurements and simulations were obtained in the stable region of the pulse train, after the initial ring-up phase. For single-cycle treatments, most treatments were conducted at a higher input source voltage of ~240V. Since this voltage exceeded the hydrophone's measurable range, HIFU beam simulations were used to estimate the in-situ pressure. A linear regression model was fitted across all FOPH-measured values at different voltages to establish the relationship between the first cycle and the third cycle (stable waveform) of the pulse train. Using this regression, the predicted in-situ pressures at the 240V input voltage were P_+ = 40 MPa and P_{-v} = 13.6 MPa. For single-cycle treatments, only peak negative pressures (P^-) are critical for cavitation cloud formation. The predicted P_- values at the current PRF of 10000 Hz aligned with values from a similar study using a single-cycle histotripsy transducer at 1000 Hz PRF. That study also reported that the P_- cavitation threshold decreased accordingly, as PRF increased. [57].

6.3.2 *Single point qualitative assessment: Phase contrast evaluation and OTLS*

A qualitative assessment of the lesions using phase contrast microscopy showed a fully liquified contiguous volume (yellow outline), surrounded by partially damaged areas (orange outline) in Figure 6.3 for all doses with the 100,1000 and 10000 cycle treatments. The lesions overall resembled a densely packed, ellipsoid-shaped pattern as also seen from the OTLS scans. On B-mode this appeared as fully hypoechoic regions surrounded by a hyperechoic region. Both the 1-cycle and 10-cycle treatments also resulted in microscopic fully-liquefied regions with pockets of damage interspersed with intact gel, forming tubular-like structures, as indicated by the red arrows. The lesions can be classified as loosely sparse, unlike the higher pulse duration treatments that formed a single contiguous liquefied region. OTLS scan renders further confirm this, revealing sparsely distributed tubular structures for the 1-cycle and 10-cycle treatments. However, on B-mode, there were no discernable differences in the speckle pattern to differentiate the fully liquified areas from partially damaged areas.

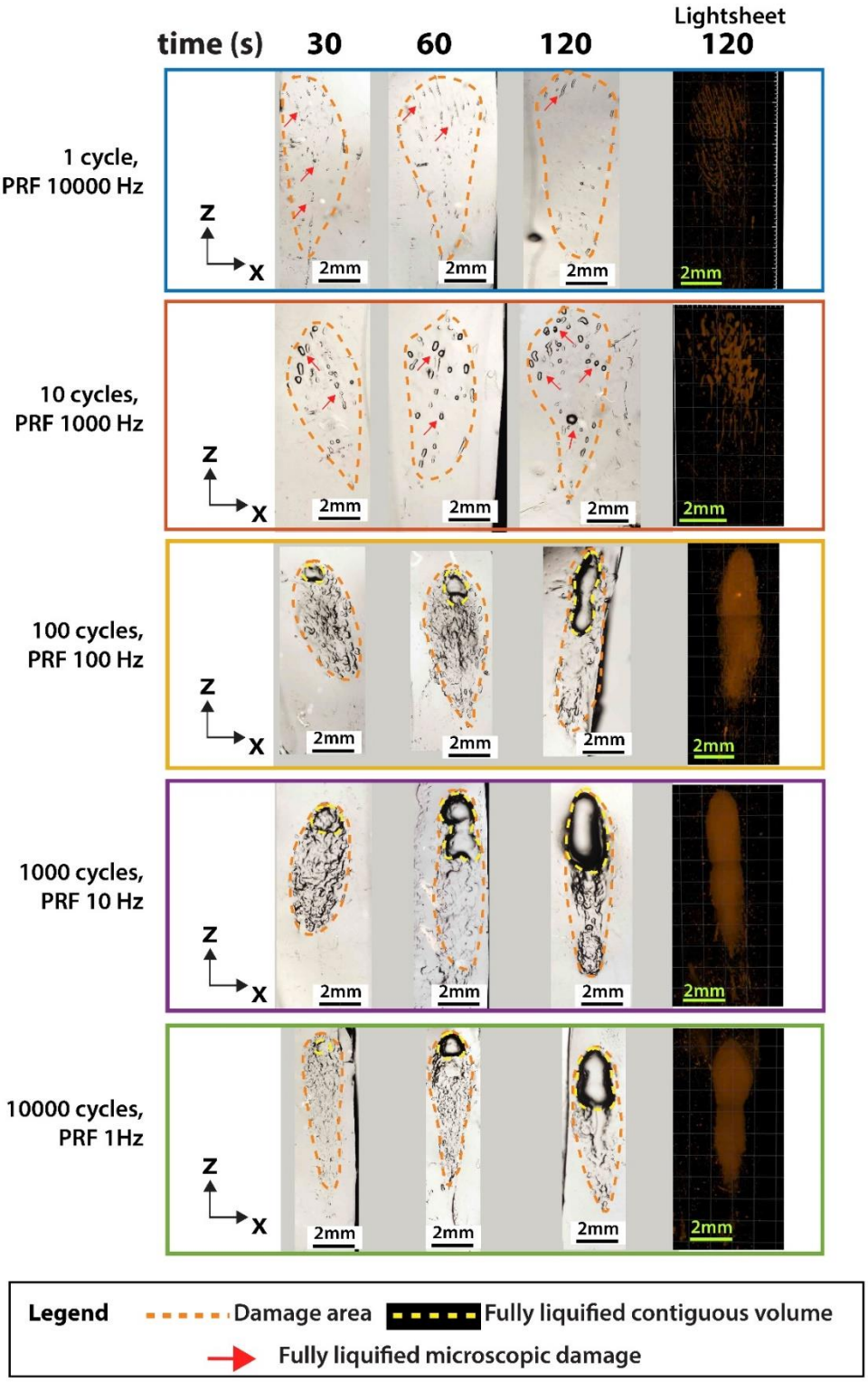

Figure 6.3. Phase contrast microscopy images and OTLS scans rendered through Imaris viewer of single point lesions. Images rotated 90° with respect to the cloud image. The face of the transducer is at the top, with the acoustic propagation axis going from top to bottom.

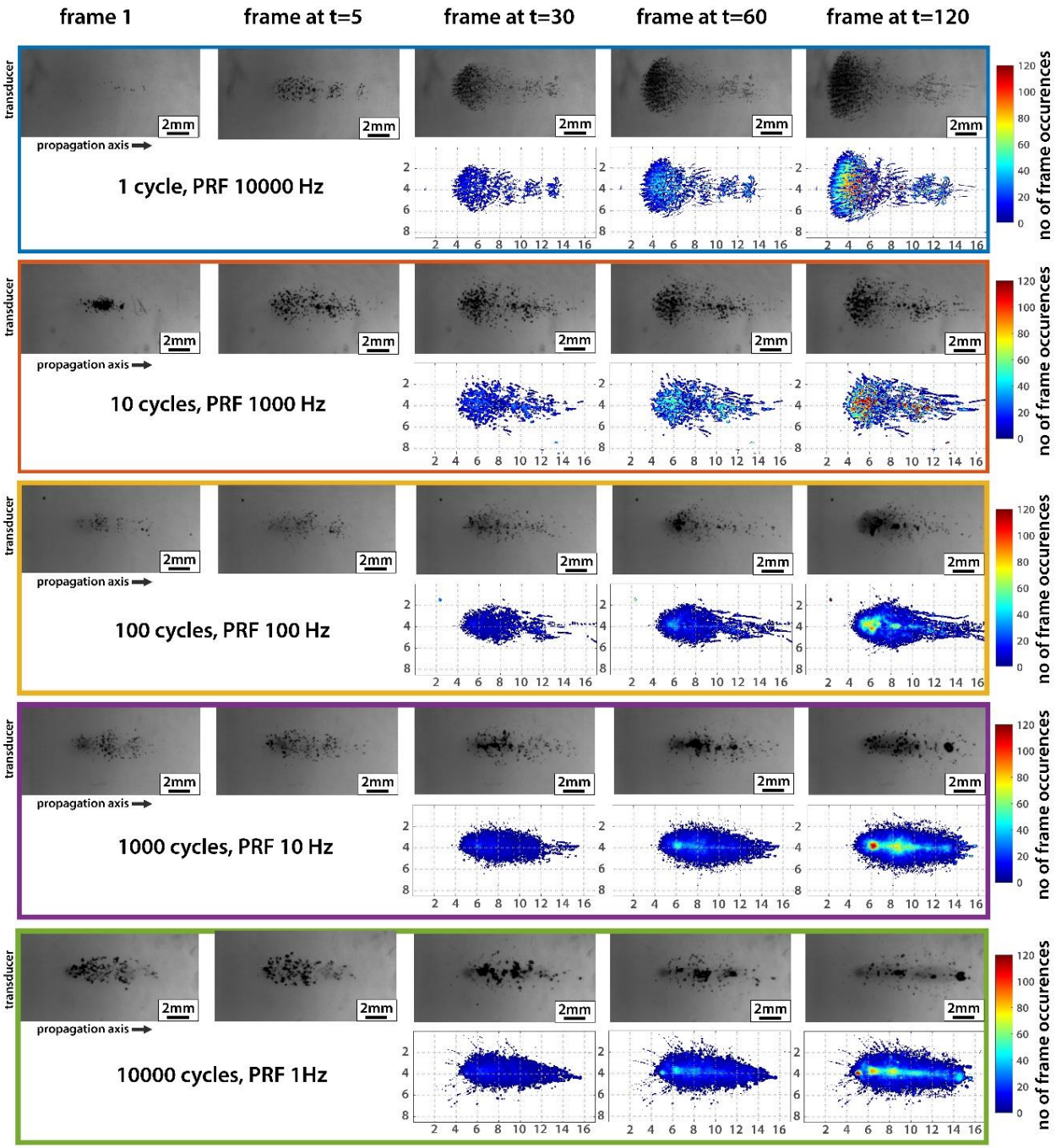

Figure 6.4. Representative high-speed camera image frames from different time points (representative scale=2mm, t in seconds). The transducer is positioned to the left of the frame and the acoustic beam transversing left to right. A cumulative map shows the bubble cloud's spread and tracks the number of frames over which a bubble appears in that location.

6.3.3 *Single point quantitative assessment: Bubble cloud characteristics*

Bubble area: The highest bubble area was observed for the 1-cycle, 10,000 Hz treatment, measuring 7.18 ± 2.96 mm². As the PRF decreased and the pulse duration increased, the bubble area progressively reduced, with measurements of 5.93 ± 1.24 mm² for the 10-cycle treatment and 2.83 ± 1.15 mm² for the 100-cycle treatment. However, beyond 100 cycles, the trend reversed—despite the continued decrease in PRF, the bubble area increased to 3.78 ± 1.08 mm² for the 1000-cycle treatment and 4.52 ± 1.20 mm² for the 10000-cycle treatment. The progression of bubble area with dose is illustrated in Figure 6.5a. A one-way ANOVA test indicated that increasing the dose did not result in a statistically significant increase in bubble area for the 10, 100, 1000, and 10000-cycle treatments. However, for the 1-cycle treatments, the bubble area visibly increased with dose progression. Post-hoc analysis using Tukey's HSD method confirmed significant differences between the 30–60 s, 30–120 s, and 60–120 s dose comparisons ($p < 0.05$). Additionally, a one-way ANOVA grouped by dose was performed to compare bubble area differences across different treatment parameters:

- At 120 s, the 1-cycle treatment exhibited a significantly larger bubble area (10.77 ± 1.81 mm²) compared to all other treatments ($p < 0.05$).
- At 60 s, both the 1-cycle and 10-cycle treatments were significantly different from the other treatments ($p < 0.05$*), whereas the 100, 1000- and 10000 cycle treatments showed no significant differences among them.
- At 30 s, the following comparisons were statistically significant: 1 vs 100 cycles, 1 vs 1000 cycles, 10 vs 100 cycles, 10 vs 1000 cycles, and 100 vs 10000 cycles.

Correlation coefficient: The Pearson correlation coefficient was highest for the 1-cycle treatments at 0.82 ± 0.04, followed by the 10-cycle treatments at 0.75 ± 0.04. For the 100, 1000,

and 10000-cycle treatments, the coefficient showed a slight decreasing trend with an increasing cycle count, measuring 0.34 ± 0.06, 0.31 ± 0.06, and 0.32 ± 0.04, respectively. As shown in Figure 6.5b, the correlation coefficient for the 1- and 10-cycle treatments quickly exceeded 0.7 at lower doses, indicating that bubbles consistently appeared in the same location from frame to frame with subsequent pulses. This was further supported by the cumulative bubble cloud maps in Figure 6.4. Additionally, for the 1-cycle treatments, the correlation coefficient continued to increase after 30 seconds of treatment, with cumulative maps revealing a prefocal shift of the bubble cloud towards the transducer face.

Cumulative bubble area and probability plots: The cumulative bubble area, shown in Figure 6.5c as a measure of cloud spread observed through the camera in a 2D view, was tracked at 30, 60, and 120 seconds of treatment. The results showed an increasing trend with increasing dose. At 30 seconds, the highest cumulative bubble area was recorded for the 10000-cycle treatments at 28.09 ± 4.85 mm², gradually decreasing with shorter pulse durations, reaching 12.78 ± 2.57 mm² for the 10-cycle treatments. However, the 1-cycle treatments deviated from this trend, measuring 14.44 ± 1.33 mm². A similar pattern was observed at 60 and 120 seconds. By 120 seconds, the cumulative bubble area peaked at 34.92 ± 3.23 mm² for the 10000 cycle treatments and 22.16 ± 4.32 mm² for the 10 cycle treatments. Interestingly, the 1-cycle treatments exhibited a higher cumulative area of 33.77 ± 4.17 mm² at 120 seconds.

Probability plots in Figure 6.5c showed that across all doses, the percentage of the cumulative bubble area with $P > 0.5$—indicating regions where the cloud appeared in more than half of the frames—was highest for the 10-cycle treatments (20.2–26.3% of the total area),

followed by the 1-cycle treatments (14.3–15.2%). For the 100-, 1000-, and 10000-cycle treatments, these values were lower, measuring <2%, ~3%, and ~6%, respectively.

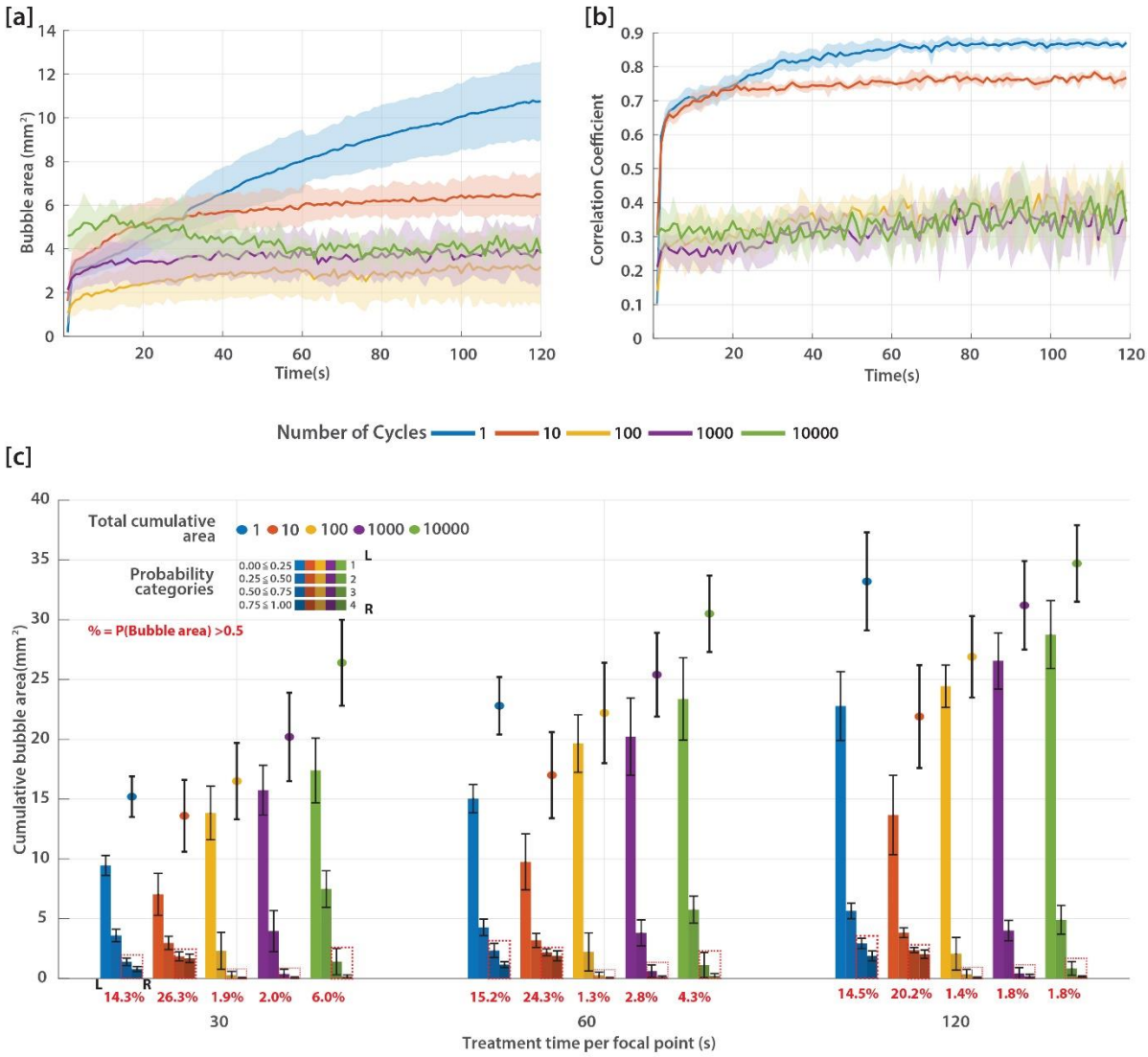

Figure 6.5. (a) Representation of the bubble cloud area (mean±sd) evolution for the different parameters with respect to time (dose). (b) Pearson correlation coefficient measured for every successive frame for all the parameters. The values plotted represent mean±sd across n=3 treatments. (c) The scatter plot represents the cumulative bubble area (mean±sd), and the bar graph represents the percentage bubble area with a falling in the different probability categories The values mentioned in red, is the percentage of the cumulative bubble area with a P>0.5.

6.3.4 *Single point quantitative assessment, Shear wave elastography and B-mode:*

The gels were homogenous across all treatments and doses as seen in Figure 6.6(a). The mean value of the stiffness measured in the untreated areas was 91.74±7.87 kPa. A one-way ANOVA of the stiffness between parameters showed a $p<0.05$; however, a post hoc test using Tukey's HSD to compare the groups showed a lack of statistically significant difference between most treatments ($p>0.05$), except 10-1000,10-10000 comparisons, which was a weak significance ($p=0.04$).

The stiffness difference between the untreated and treated area, measured in % difference, showed an increasing trend as the dose increased as shown in Figure 6.6b for ≥100 cycle treatments. No such patterns were observed for the 1 and 10 cycle treatments. The difference in stiffness between untreated and treated regions at 30s, was -38.33±6.68 %, -54.55±1.87 % and -44.46±6.74 % for 100,1000 and 10000 cycle treatments. At 120s, this difference was more pronounced at -74.31±4.27 %, -78.46±1.87 % and -75.34±7.35 %. 1000 cycle treatments had the highest difference in stiffness across all doses in comparison to other parameters. For both 1 and 10 cycle treatments, the maximum difference in stiffness was 8.18±5.91 % and 10.91±9.59 % respectively.

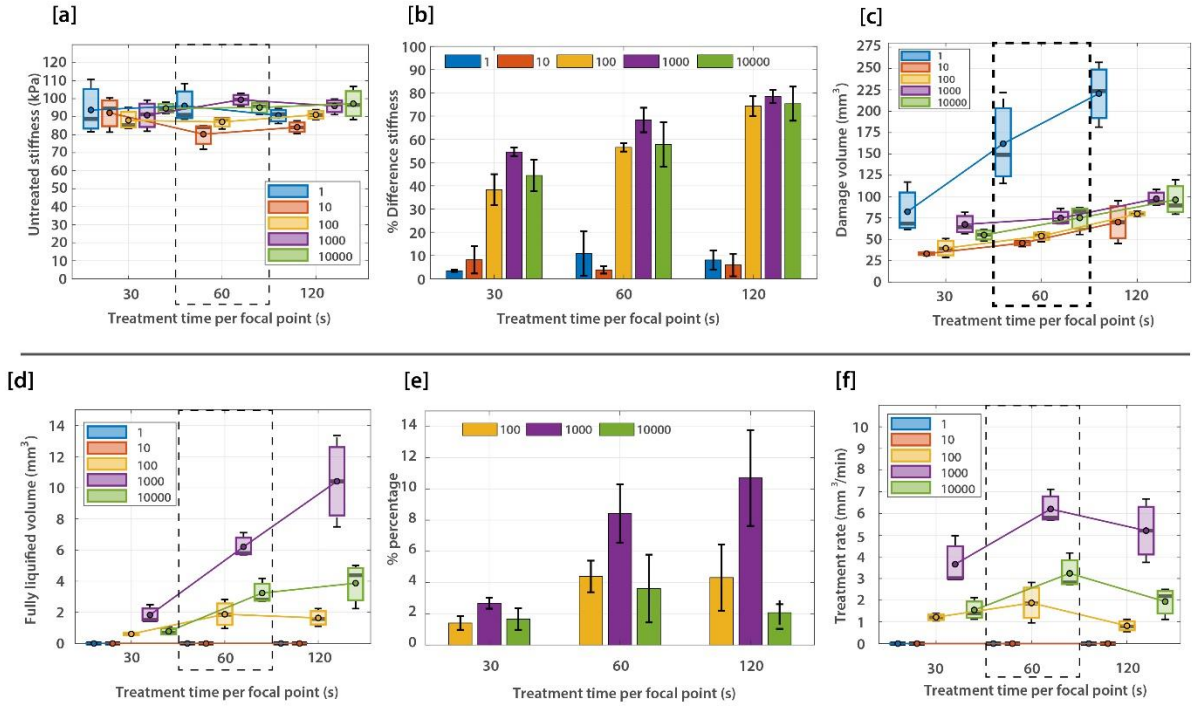

Figure 6.6. (a) Untreated stiffness of the gel from all treatments and dose (b) Percentage difference in stiffness (untreated-treated) (c) Total damage volume (Hyper and hypoechoic region) from B-mode scans. (d) Fully liquified volume estimates from hypoechoic region in B-mode scans (e) percentage ratio of the fully liquified volume to the total damage volume (f) Volumetric rate estimations for the treatments that had fully contiguous liquified volume at the macroscopic level.

The total damage volume and fully liquefied volume measurements from B-mode imaging are presented in Figure 6.6(c), Figure 6.6(d), and Table 6.11. With increasing dose, the total damage volume consistently increased across all parameters. The highest total damage volume was observed in single cycle treatments at 120s 220.73 ± 37.99 mm³, while the lowest was in 10 cycle treatments 70.17 ± 25.03 mm³. Fully liquefied volumes were only calculated for treatments with ≥100 cycles, as the hypoechoic region was clearly identifiable, unlike in the 1 and 10 cycle treatments, where no discernible macroscopic speckle pattern changes were observed. Among the 100, 1000, and 10000 cycle treatments, the 1000 cycle treatment at 120s had the largest total

damage volume 97.49 ± 9.60 mm³ and fully liquefied volume 10.42 ± 2.93 mm³, resulting in the highest liquefied-to-total damage volume ratio 10.70 ± 3.08%. In comparison, the 10000 cycle treatment at 120s had a similar total damage volume 96.30 ± 20.98 mm³ but a lower liquefied-to-total damage ratio 3.87 ± 1.45%. The 100-cycle treatment exhibited a total damage volume of 79.83 ± 2.85 mm³, with the lowest liquefied-to-total damage ratio 1.64 ± 0.57% at the highest dose.

Table 6.11. Tabulation of total damage volume and fully liquified volume(macroscopic) across parameters and dose measured from B-mode scans (mean±sd) for single point lesions.

Cycles	**Total damage volume (mm^3) - Single point**			**Fully liquified volume (mm^3) - Single point**		
	Dose (s)			**Dose (s)**		
	30	**60**	**120**	**30**	**60**	**120**
1	82.36 ± 30.25	162.03 ± 54.41	220.73 ± 37.99	-	-	-
10	33.17 ± 2.11	45.50 ± 3.50	70.17 ± 25.03	-	-	-
100	39.56 ± 11.13	53.87 ± 5.94	79.83 ± 2.85	0.61 ± 0.09	1.87 ± 0.93	1.64 ± 0.57
1000	67.49 ± 12.84	74.85 ± 9.92	97.49 ± 9.60	1.83 ± 0.57	6.21 ± 0.79	10.42 ± 2.93
10000	55.02 ± 6.95	75.13 ± 16.96	96.30 ± 20.98	0.77 ± 0.26	3.24 ± 0.82	3.87 ± 1.45

6.3.5 *Single point: Statistical analysis*

The ANCOVA analysis, summarized in Table 6.12, indicates that the slope of the total damage volume for the single-cycle treatment was statistically significantly different ($p<0.001$) compared to all other parameters. For comparisons among the remaining parameters, no statistically significant differences were observed in total damage volume estimates. Similarly, for the fully liquified volume, no statistically significant difference was seen between 100 and 10000 cycle treatments. However, for the 100-1000 and 1000-10000 cycle comparisons showed a

statistically significant difference in slopes ($p<0.0001$). with average damage volume difference of -4.78±3.68 mm^3 and 3.52±3.32 mm^3 respectively, indicating the 1000 cycle treatment performed better than the other groups.

The volumetric rate analysis on the single point lesions shown in Figure 6.6(f) , which is important from a clinical perspective, showed that the maximum rate mm^3/min was achieved at 60s of dose across all the parameters 1.87 ± 0.93 mm^3/min (100 cycle), 6.21 ± 0.79 mm^3/min (1000 cycle), 3.24 ± 0.82 mm^3/min (10000 cycle), with the highest rate observed for 1000 cycle. The rate marginally decreased at 120s of dose.

Table 6.12. Comparison of the slope coefficients (ANCOVA analysis- Parameter (cycle) : Dose (time) interaction) on the single point and grid lesions with volume measurements from B-mode scans. * show statistically significant results.

Reference Parameter (Cycles)	2nd Parameter (Cycles)	Total damage (single point)		Fully liquified volume (single point)		Total damage (Grid)		Fully liquified volume (Grid)	
		t-ratio	p-value	t-ratio	p-value	t-ratio	p-value	t-ratio	p-value
1	10000	-3.68	0.0008*	-	-	-7.43	<.0001*	-	-
1	1000	-4.05	0.0003*	-	-	-5.33	<.0001*	-	-
1	100	-3.67	0.0008*	-	-	-7.09	<.0001*	-	-
1	10	-3.79	0.0006*	-	-	-7.08	<.0001*	-	-
10	10000	0.12	0.907	-	-	-0.36	0.7246	-	-
10	1000	-0.26	0.7971	-	-	1.75	0.0896	-	-
10	100	0.12	0.9018	-	-	-0.02	0.9875	-	-
100	10000	-0.01	0.9947	1.68	0.1021	-0.34	0.7364	-1.21	0.2326
100	1000	-0.38	0.7038	6.36	<.0001*	1.76	0.0868	7.7	<.0001*
1000	10000	0.38	0.7087	-4.68	<.0001*	-2.1	0.0429*	-8.92	<.0001*

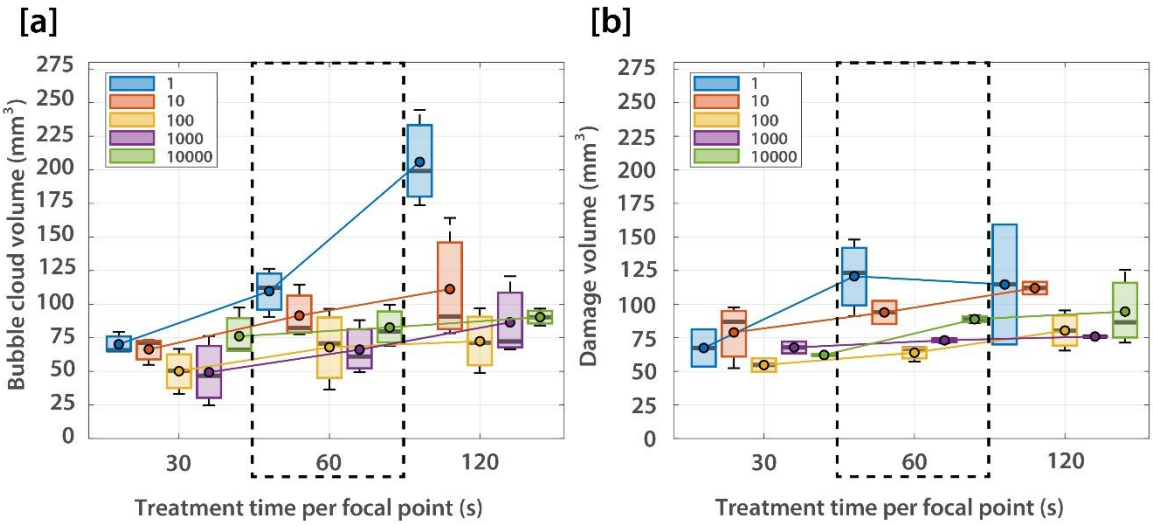

Figure 6.7. (a) Total damage volume measurement from cumulative bubble cloud image for each parameter and dose, (b) Total damage volume measurement from OTLS scan for each parameter and dose

Correlation of bubble cloud volumes to damage volume: Figure 6.7 illustrates the volume estimate from bubble cloud data and damage volume estimates from OTLS scans. For ≥100 cycle treatments, bubble cloud volume estimates correlated well with total damage estimates from B-mode and OTLS scans, with no statistically significant difference observed in a two-tailed test. For 10-cycle treatments, no significant difference was found between cloud volume and OTLS scans. However, both cloud volume and OTLS damage estimates were significantly different from B-mode estimates ($p<0.001$, $p<0.0001$), with average difference of $36.71\pm7.0 mm^3$ and $49.32\pm5.48 mm^3$ respectively, indicating that B-mode underestimated damage volume. Similarly, for 1-cycle treatments, no significant difference was found between cloud volume and OTLS scans. However, a statistically significant difference was observed between cloud volume and B-

mode estimates ($p<0.05$), with a difference of $-33.51\pm11.34 mm^3$ indicating an overestimation by B-mode.

6.3.6 *Grid ablation qualitative assessment: Phase contrast imaging*

Prior to phase contrast microscopy, the lesions were examined using a benchtop illumination setup, appearing cloudy due to changes in the refractive index of the damaged areas. Similar to single-point lesions, a qualitative assessment using phase contrast microscopy revealed a fully liquefied contiguous volume (yellow outline) surrounded by partially damaged regions (orange outline) for treatments of ≥100 cycles, as shown in Figure 6.8. The lesions exhibited a densely packed, widened ellipsoid-shaped pattern due to 50% grid overlap, appearing as fully hypoechoic regions surrounded by a hyperechoic border on B-mode imaging. For 1-cycle treatments, the lesion shape also appeared ellipsoidal but was more sparsely packed, with intact gel interspersed between damaged regions. The fully liquefied regions were significantly more prominent in higher-cycle treatments compared to single-cycle treatments, which appeared skinnier and elongated, as indicated by the red arrows. Additionally, the lesions from 1-cycle treatments were not discernible on B-mode imaging, as no differences in the speckle pattern allowed for differentiation between fully liquefied and damaged areas.

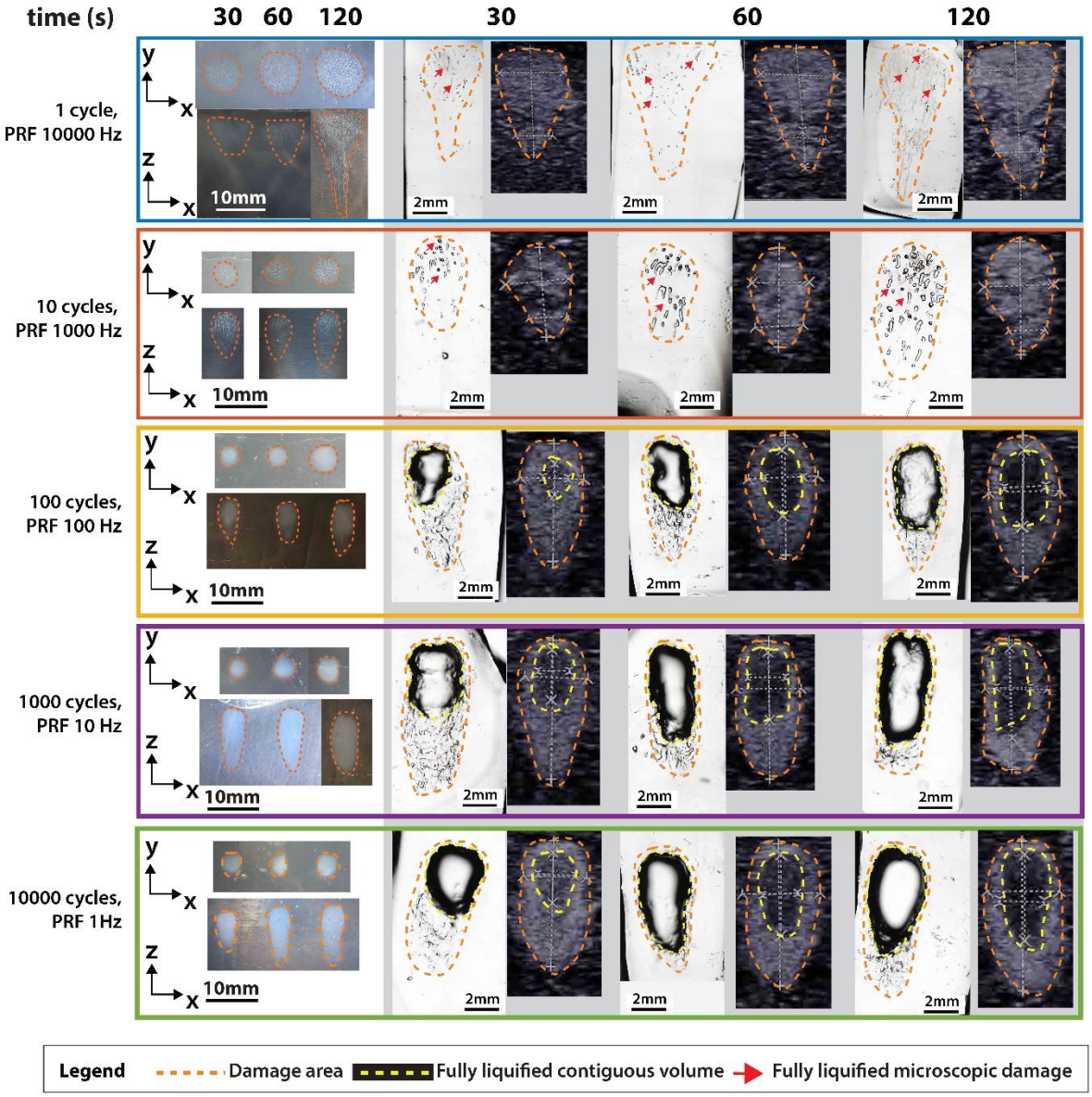

Figure 6.8. Phase contrast microscopy images and OTLS scans rendered through Imaris viewer of grid lesions. Images rotated 90o with respect to the cloud image. The face of the transducer is at the top, with the acoustic propagation axis going from top to bottom.

6.3.7 *Grid ablation quantitative assessment: Shear wave stiffness and B-mode analysis*

The gels used for these treatments were homogenous and was verified by stiffness measurements using shear wave elastography (SWE) as seen in Figure 6.9(a). The mean value of the stiffness measured in the untreated areas was 69.75±5.45 kPa, which was lower than the single point lesion study. There were no statistically significant differences in untreated stiffness of the gels across all treatments ($p=0.153$).

The stiffness difference between the untreated and treated areas, measured in % difference, showed an increasing trend as the dose increased as shown in Figure 6.9b for ≥10 cycle treatments. For 1 cycle treatment, however, there was a decreasing trend as dose increased. The difference in stiffness between untreated and treated regions at 30s, was 70.65±1.73 %, 80.97±1.78 % and 80.88±1.21 % for 100,1000 and 10000 cycle treatments. At 120s, this was more pronounced at -78.36±2.17 %, -91.29±2.41 % and -84.13±2.30 %. 1000 cycle treatments once again had the highest difference in stiffness across all doses in comparison to other parameters. For both 1 and 10 cycle treatments, the maximum difference in stiffness was -18.96±7.95 % (dose=30s) and -23.37±8.16 % (dose=120s) respectively.

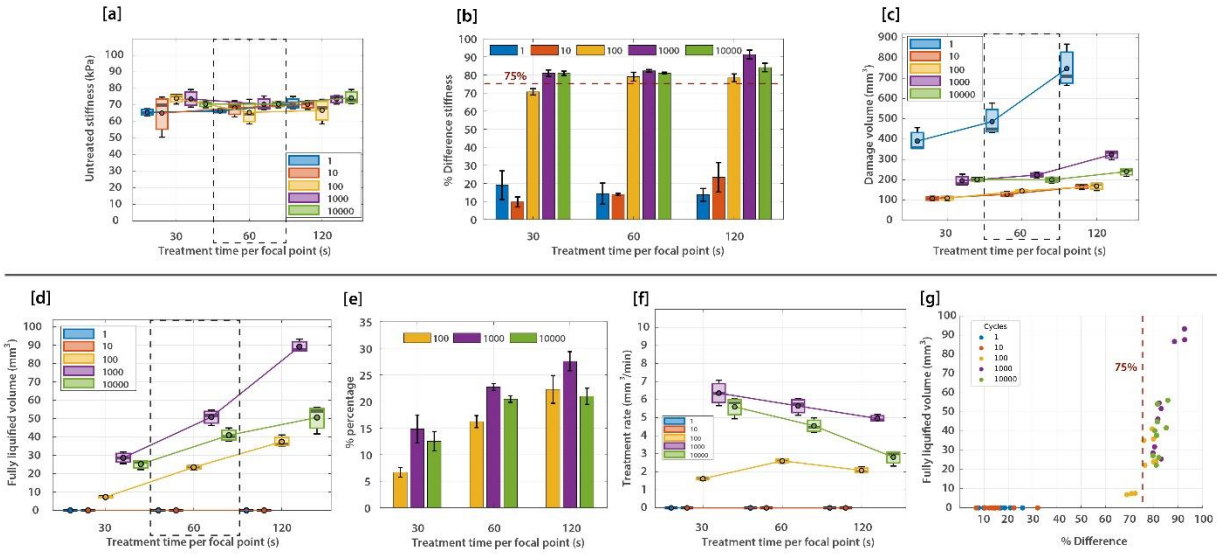

Figure 6.9. (a) Untreated stiffness of the gel from all treatments and dose (b) Percentage difference in stiffness (untreated-treated) (c) Total damage volume (Hyper and hypoechoic region) from B-mode scans. (d) Fully liquified volume estimates from hypoechoic region in B-mode scans (e) percentage ratio of the fully liquified volume to the total damage volume (f) Volumetric rate estimations for the treatments that had fully contiguous liquified volume at the macroscopic level.

The total damage volume and fully liquefied volume measurements from B-mode imaging are presented in Figure 6.9(c), Figure 6.9(d), and Table 6.13. With increasing dose, the total damage volume exhibited an upward trend across all parameters. The highest total damage volume was observed in single-cycle treatments at 120s, measuring 747.52 ± 106.63 mm³, while the lowest was comparable between the 10-cycle and 100-cycle treatments at the same dose, measuring 165.09 ± 11.44 mm³ and 168.92 ± 18.99 mm³, respectively.

Fully liquefied volumes were only calculated for treatments with ≥100 cycles where the hypoechoic region was clearly identifiable. In contrast, the 1-cycle and 10-cycle treatments showed no discernible hypoechoic regions. Among the 100, 1000 and 10000-cycle treatments, the

1000-cycle treatment at 120s resulted in the largest total damage volume 324.16 ± 22.88 mm^3 and the highest fully liquefied volume 89.17 ± 3.57 mm^3, leading to the highest liquefied-to-total damage volume ratio 27.58 ± 1.79%, which was ~3 times higher than the single point lesion.

For comparison, at 120s:

- The 100-cycle treatment had a total damage volume of 168.92 ± 18.99 mm^3 with a liquefied-to-total damage volume ratio of 22.27 ± 2.60%, that was approximately ~13 times higher than the single point lesions.
- The 10000-cycle treatment had a total damage volume of 240.06 ± 20.47 mm^3, with a liquefied-to-total damage volume ratio of 20.99 ± 1.53% that was approximately ~5 times higher than the single point lesions.
- Despite the 100-cycle treatment exhibiting a lower total damage volume than the 10000-cycle treatment, a greater percentage of it was fully liquefied.

Table 6.13. Tabulation of total damage volume and fully liquified volume(macroscopic) across parameters and dose measured from B-mode scans (mean±sd) for grid lesions.

Cycles	**Total damage volume (mm^3) - Grid**			**Fully liquified volume (mm^3) - Grid**		
	Dose (s)			**Dose (s)**		
	30	**60**	**120**	**30**	**60**	**120**
1	390.71 ± 57.25	486.41 ± 79.26	747.52 ± 106.63	-	-	-
10	108.29 ± 11.18	128.35 ± 13.04	165.09 ± 11.44	-	-	-
100	109.73 ± 12.14	144.91 ± 7.34	168.92 ± 18.99	7.26 ± 0.35	23.47 ± 1.11	37.37 ± 3.25
1000	195.46 ± 27.96	223.54 ± 13.74	324.16 ± 22.88	28.62 ± 3.16	50.83 ± 4.26	89.17 ± 3.57
10000	201.97 ± 10.50	199.97 ± 14.55	240.06 ± 20.47	25.20 ± 2.63	40.92 ± 3.65	50.59 ± 7.80

6.3.8 *Grid ablation: Statistical analysis*

A statistical comparison of the total damage volume and fully liquified volume performed using the ANCOVA analysis is summarized in Table 6.12. The results indicate that the slope of the total damage volume for the single-cycle treatment was statistically significantly different ($p<0.0001$) compared to all other parameters. For comparisons among the remaining parameters, no statistically significant differences were observed in total damage volume estimates except for the 1000-10000 cycle. With a $p=0.0429$, however, it was weakly significant. Similarly, for the fully liquified volume, no statistically significant difference was seen between 100 and 10000 cycle treatments. However, for the 100-1000 and 1000-10000 cycle comparisons showed a statistically significant difference in slopes ($p<0.0001$). with average volume difference of -33.51±14.17 mm^3 and 17.31±16.84 mm^3 respectively, indicating the 1000 cycle treatment performed better than the other groups.

The volumetric rate analysis of the grid lesions is presented in Figure 6.9(f). Interestingly, in contrast to single-point lesions, the trend line for 1000-cycle and 10000-cycle treatments showed a decrease in volumetric rate with increasing dose. The maximum volumetric rate was observed at 30s of dose, reaching 6.36 ± 0.70 mm^3/min for the 1000-cycle treatment and 5.60 ± 0.58 mm^3/min for the 10000-cycle treatment. For 1000-cycle treatments, these rates were comparable to those of single-point lesions at 60s. However, for 100-cycle treatments, the volumetric rate increased from 30s to 60s, reaching a peak of 2.61 ± 0.12 mm^3/min, before marginally decreasing at 120s. Between the single point lesion and the grid study, the 1000 cycles treatment, achieved a maximum rate that was within 2% of each other, albeit at different doses per point (60s, and 30s respectively). For 100 cycle treatments, going from single point to grid, the increase was 40%, observed at 60s and for 10000 cycles, the increase was 73% compared from doses (60s, and 30s respectively).

Figure 6.9(g) plots the % difference in stiffness (kPa) versus fully liquified volumes measured from B-mode scans. Notably, most data points fall to the right of the 75% threshold line which was established in our previous publication Nanda Kumar et al [172], as the threshold above which complete contiguous liquefied areas were achieved in the ex vivo prostate equivalent tissue. This alignment suggests that most of the measured lesions from this study surpassed the stiffness reduction threshold necessary for achieving fully liquefied regions at a macroscopic level.

6.4 DISCUSSION

Previous studies have explored the use of histotripsy in liquefying a variety of tough tissues, like ureteroceles[40], peyronie's plaque[31], uterine fibroids[39,170], cholangiocarcinoma[33] and benign prostatic hyperplasia[52,148,172]. Most of these studies successfully treated these tissues, using a transabdominal-based delivery of histotripsy by different transducers operating in different regimes (cavitation cloud, intrinsic and boiling histotripsy). In the lead-up to our previous publication on treating the ex-vivo human benign prostatic hyperplasia[172] successfully, we compared the clinically used high-PRF, low duty cycle cavitation cloud histotripsy regime (Schuster et al [52]) and tested it against a low PRF regime at different doses with the same transducer, operating at 700kHz. In addition, we also tested a boiling histotripsy regime with a longer pulse duration and higher duty cycle but delivered by a 1.5MHz transducer. All parameters successfully fully liquified the tissue at varying levels of dose, which translated to different volumetric rates. As a continuation of that work, in this study, we systematically compared the outcomes of different treatment parameters in histotripsy by varying pulse duration (cycles) and pulse repetition frequency (PRF) while maintaining a duty cycle of 1%. The therapy was delivered into a fibrous tough tissue mimicking double network hydrogel phantom using a 1 MHz transducer, to compare the effects at the parameter level.

Longer pulse durations of 100 μs and above (≥100 cycles) at lower pulse repetition frequencies (≤100 Hz) achieved complete and contiguous liquefaction of the gels at all doses in the single-point lesion as well as the grid overlap study. This liquified volume was surrounded by partially damaged areas that resolved with hyperechogenicity on the B-mode. In contrast, both 1-cycle and 10-cycle pulses produced sparsely liquefied areas resembling tubular structures under OTLS scans, which were also visible on phase contrast microscopy. However, these lesions were microscopic and lacked the macroscopic continuity observed with other parameters. A potential explanation for the reduced efficacy of the 1-cycle and 10-cycle treatments is the "cavitation memory effect," a phenomenon well-documented in prior studies[57,61,157,158,181]. This effect is evident in the cumulative maps in Figure 6.4, the probability plots and correlation coefficient measures in Figure 6.5. for both treatment types. In 10-cycle treatments, the cavitation cloud was continuously re-excited in most regions, yet minimal pre-focal cloud growth was observed. Conversely, for 1-cycle treatments, strong pre-focal cloud growth occurred, likely due to shielding and cavitation memory effects. These findings are further supported by the probability plots, where the cumulative area with P>0.5 was significantly higher for 10-cycle treatments compared to 1-cycle treatments. Additionally, the correlation coefficient rapidly exceeds 0.7 at lower doses for both treatment types, indicating that with successive pulses, bubbles repeatedly appear in the same location. In 1-cycle treatments, the correlation coefficient continues to rise even after 30 seconds of treatment. The bubble dynamics are influenced by the driving frequency, amplitude, pulse duration[84,169], and the time required for dissolution also varies as a function of liquefaction. In 1-cycle treatments, with a PRF of 10000 Hz, it is possible that the bubbles persist at a size that enhances the reflection of incoming shock waves, promoting pre-focal growth towards the transducer face and further restricting bubble growth at the focus. In contrast, in 10-cycle treatments with a PRF of 1000 Hz,

bubble clouds collapse more significantly between pulses, reducing pre-focal growth and allowing for greater cavitation activity at the focus.

Prior studies have reported on higher PRF's as a reason for cavitation memory effect and pre focal shift of the cloud, often finding that PRF's of ≥1 Hz [157] or ≥ 10Hz, [57] created significant contribution to this effect. However, to the contrary, in this study, we found the cavitation memory effect appeared only in PRF's 1000 Hz and above and prefocal shift occurred with the 10000 Hz (1cycle) parameter, even though the treatments were performed at a much higher duty cycle. One potential reason could be that most of these studies were conducted in RBC agarose phantoms, which are known to be stiff but lack the toughness of double-network hydrogels that more closely mimic fibrous tissue. This difference in mechanical properties could influence bubble dynamics and progression of lesion formation[169].

The shape of the lesions correlated well with the bubble cloud activity. It was "ellipsoidal" for both 1000 and 10000 cycle and "near ellipsoidal" for the 100 cycle treatments, therefore precise ablation was achieved. The lesions formed with these 3 parameters also had a clear contiguous liquid pocket. For both the 10 and 1 cycle treatments, since the PRF increased, the shape deviated from an ellipsoidal shape to a more distinct "conical shape" for the 1-cycle treatments. A similar observation was made in the study by Wang et al [158]. The sparse lesion formation could also be due to the higher f-number used in this study, which meant that at these higher PRF's a dense cloud may not be formed, which is crucial for higher ablation efficiency [84]. It is also possible that at higher PRF treatments, if the dose was increased beyond the scope of this study, a contiguous liquid pocket will eventually form but may not be clinically viable. This was observed both in the study by Wang et al [158] and our prior study Nanda Kumar et al [172]. At higher PRF's off-target cavitation events can cause damage in unintended areas, which in our study were observed by

potential tunnel like structures in regions beyond the focus and pre-focally, a phenomena also reported by Simon et al[57].

We explored a novel approach using Open Top Light Sheet (OTLS) microscopy to nondestructively evaluate lesions, which worked on the principle of reflective based imaging. The properties of this double network hydrogel made it possible, and this was our novel attempt to measure true volume estimates rather than relying on projections from 2D scans. While this technique provided the most accurate measurements of total damage volume, it had some limitations. In a few 10000-cycle treatments, fully liquefied regions were not detected due to the absence of light scattering, preventing them from appearing in the final scan. Additionally, distinguishing between fully liquefied volumes and partially damaged areas was challenging, as both appeared with the same intensity. As a result, only total damage volumes were estimated from these scans. Saturation effects caused by reflections from the holder rendered some scans unusable, reducing the number of datasets available for processing. Further refinements to this technique will be explored to enhance its accuracy and differentiation capabilities. Additionally, Optical Coherence Tomography (OCT) will be investigated as a potential alternative for future studies.

B-mode scans served as the primary means to estimate damage volume estimates. The total damage volumes estimated from OTLS scans and cloud images correlated well with those from B-mode scans for treatments with ≥100 cycles. However, in 1-cycle treatments, a discrepancy was observed, with B-mode scans overestimating the total damage volumes. This overestimation occurred because the volumes were calculated by fitting a mask to the overall extent of the hyperechoic region. As observed in the cloud images and damage patterns under benchtop illumination, individual bubbles were sparsely distributed, potentially leading to estimations that included empty spaces. A similar effect may have influenced the grid study volume measurements,

where high values were recorded for the 1-cycle treatment. This issue did not occur with ≥100-cycle treatments, as the cavitation clouds and hyperechoic regions were densely packed. However, in 10-cycle treatments, B-mode severely underestimated the damage volume due to the high noise in the speckle pattern, making identification challenging. This limitation was not observed in the grid study. These challenges highlight the limitations of using B-mode for volume measurements when monitoring parameters that generate sparse cavitation clouds. For B-mode to be more effective, a higher-frequency transducer could improve image resolution for better identification; however, this would come at the cost of reduced penetration depth and will be explored for future studies.

Shear-wave elastography (SWE) has once again proven to be a useful indicator in correlating with fully liquified volumes, which will serve as an important tool for treatment monitoring in the pursuit of making treatment times clinically viable. Both 1 and 10 cycle treatments showed a very low percentage difference in stiffness, possibly because the ROI measured areas of liquified volume laced with intact tissue. In the grid study, except for the 100-cycle treatments at a dose of 30 seconds, all other doses, as well as the 1000-cycle and 10,000-cycle treatments, exhibited a percentage difference above 75%. This threshold, established in our prior study, indicates full liquefaction, as observed in ex vivo prostate studies[172].

Among all the parameters tested, the 1000-cycle treatments were most effective in creating larger volumes of fully liquefied regions in both the single-point and grid studies. Beyond 1000 cycles, a plateau effect was observed, indicating no additional benefit in increasing cycles beyond 1000. The volumetric rate from the grid study, a crucial parameter for clinical viability, was measured at 6.36 ± 0.70 mm^3/min for 1000-cycle (1-ms) treatments and 5.60 ± 0.58 mm^3/min for 10000-cycle (10-ms) treatments. These values closely matched patterns observed in other studies,

notably Khokhlova et al. [148] who reported ablation rates of 9±1.7 mm³/min for 1-ms treatments and 4.5 ± 0.7 mm³/min for 10-ms treatments. Their study, which used histological slides as the gold standard, treated ex-vivo human BPH prostate with a similar f-number transducer but at a different frequency. Additionally, the 10-ms values from the current study align with findings from our previous ex-vivo prostate work [172]. The volumetric rate was the highest for 1000 cycle treatments in comparison to all other parameters, across both single point and grid lesions. This was, however, observed at different doses and was within 2% for the 1000 cycle treatments. Though with dose, damage volumes increased as well as the fully liquified volume, the highest rate was not necessarily observed at the highest dose which warrants further investigation. Although for the other parameters, there was an increase in the rate by >40% because of the overlap, it did not offer any advantage for the 1000 cycle treatment. Future studies will explore grid spacing, to identify the most optimal distance that could enhance the volumetric rate. Additionally, one could also explore a lower dose of 15 seconds which could narrow down parameter space that are effective in creating fully liquified volumes. Continuous treatment monitoring by shear-wave elastography, Doppler ultrasound [167] can inform the user when necessary liquefaction is achieved, which can reduce overtreating and customize the treatments to individual patients and will greatly assist in optimizing the treatment time.

6.5 CONCLUSION

In this study, we systematically compared a wide range of parameters at different doses to evaluate their effectiveness in ablating tough double-network hydrogels that mimic fibrotic tissue. The results showed that longer pulse durations at lower PRFs were significantly more effective in ablating the gel. The transparency of the gels allowed for a detailed study of bubble cloud characteristics, providing further insight into the outcomes. The volumetric ablation rates observed

were comparable to those reported in ex vivo tissue from similar studies, confirming the gel as a valuable tool for optimizing parameters for clinical translation. These findings lay the groundwork for developing more efficient treatment strategies in future trials, with potential clinical applications.

CHAPTER 7. CONCLUSION AND FUTURE WORK

7.1 CONCLUSIONS

This dissertation explores various approaches to enhance the treatment of fibrous tissue that is typically resistant to histotripsy at previously tested parameters. It includes the development of specialized hardware to address challenges in clinical studies[52] and the creation of a new double-network hydrogel optimized for histotripsy treatment evaluation. Additionally, alternative treatment parameters and dosing strategies were identified to liquefy tough ex vivo benign prostatic hyperplasia (BPH). The development of an automated histological analysis technique, combined with shear wave elastography, provided quantitative metrics to assess treatment completion, that works in conjunction with qualitative B-mode imaging. Furthermore, this work presented an in-depth study of bubble dynamics across different parameters to guide future optimizations. A summary of this research is provided below.

In Chapter 2, we evaluated various commonly used histotripsy transducers, assessing their performance through holography and efficiency metrics while driving them to the highest possible power input. The study results indicated that piezocomposite transducers were the most efficient and resistant to damage; however, their higher cost and specialized manufacturing process limit rapid iterative design. In contrast, the lensed transducer emerged as the most suitable option due to its lower cost, ease of rapid iterative design, and resistance to damage. Although it exhibited some efficiency loss, its performance remained acceptable. Additionally, holography proved beneficial in identifying transducer behavior patterns which allows for the early detection of potential issues in manufactured transducers.

In Chapter 3, we explored the design and development process of recreating the clinical transducer as a reference. To address the challenges of transabdominal and transperineal

histotripsy delivery to the prostate, we developed a miniaturized transrectal transducer designed to perform both cavitation cloud histotripsy and boiling histotripsy. Initial benchtop results were promising; however, transducer failures prevented continued experimentation. Despite these setbacks, the design process documented in this chapter provides valuable insights and future directions for improving transducer development.

In Chapter 4, we demonstrated the development of a tunable homogenous double-network hydrogel composed of polyacrylamide and alginate, which effectively mimics the extracellular matrix found in more fibrous tissues. The properties of this phantom, including sound speed and density closely resemble those of ex vivo human BPH prostate tissue except for attenuation, which was found to be lower. By varying the ratio of acrylamide to alginate, we were able to achieve stiffness values commonly observed in the ex-vivo human prostate, measured in our experiments. A key advantage of this phantom is its optical transparency, which allows for studying bubble dynamics using high speed camera shadowgraphy. Additionally, its scattering properties enable stiffness measurements via shear wave elastography (SWE). To our knowledge, this is the only phantom with these properties that does not require special additives, such as alumina powder, which is commonly used in polyvinyl alcohol phantoms. Treatments applied to these phantoms were visualized using B-mode ultrasound and SWE, as well as phase contrast microscopy. Lesions appeared with enhanced contrast when using a phase contrast filter, making them easier to identify. This proved to be a valuable tool for optimizing treatment outcomes efficiently.

The shear wave elastography results were validated against indentometry, the gold standard for stiffness measurement, and were found to be equivalent. We also determined the dose, about 288s per point at which the clinical treatment parameters which is a high pulse repetition frequency (PRF) regime operating at 500 Hz with 3 cycles achieved liquefaction. Additionally, we

demonstrated that an alternative parameter set, operating at a lower PRF with a longer duration (10 Hz, 20 cycles), could achieve liquefaction at a significantly lower dose.

Our findings were further validated through preliminary experiments on ex vivo tissue, demonstrating the equivalence of the double network hydrogel model. Furthermore, we analyzed bubble dynamics by comparing high- and low-PRF treatment regimes in both agarose and the double-network hydrogel. These experiments revealed distinct differences in bubble behavior, showing that agarose liquefies at a much lower pulse count, making it an unsuitable model for replicating fibrous tissue response to the same treatment parameters.

In Chapter 5, we translated the findings from the previous chapter into a comparative study, evaluating high-PRF clinical histotripsy, the low-PRF alternative, and boiling histotripsy (BH) at varying doses to determine the optimal parameters for treating ex vivo human prostate samples. We found that BH was the most efficient in terms of dose required for liquefaction, achieving it in 30 seconds per point, followed by low-PRF histotripsy at 144 seconds and high-PRF histotripsy at 288 seconds per point. We introduced HLQE (Histotripsy Lesion Quantification by Entropy analysis) algorithm that automated the lesion quantification process and was insensitive to stain inconsistencies as it relied on the structural variations of the image. Quantitative analysis showed that more than 85% of the targeted prostate tissue was destroyed, statistically indicating full liquefaction, with breakdown observed in both glandular and fibromuscular regions while maintaining minimal thermal effects. Since different transducers were used for the CH and BH treatments, we assessed the volumetric ablation rates, finding that low-PRF histotripsy achieved the highest rate at 13.9 mm^3/min, followed by BH at 7.7 mm^3/min and high-PRF histotripsy at 6.9 mm^3/min. Within the CH parameters, low-PRF histotripsy demonstrated nearly twice the

efficiency of high-PRF histotripsy, potentially due to the cavitation memory effect observed in high-PRF treatments.

While B-mode imaging provided qualitative feedback for treatment evaluation, we established a shear wave elastography (SWE) metric of >75% reduction in stiffness from pre- to post-treatment as a reliable quantitative indicator of treatment completion.

In Chapter 6, we conducted a systematic comparison of an expanded parameter set while maintaining a constant duty cycle of 1%. Treatments were performed using the same transducer at varying doses. Until this study, most bubble dynamics had been extensively examined in a red blood cell-based agarose phantom, which, while viscoelastic, does not adequately replicate fibrous tissue response to treatment, as demonstrated in Chapter 4. This study continued our efforts to understand bubble dynamics in tough, fibrous tissue mimics subjected to different types of sonication.

A clear distinction in bubble dynamics was observed between the two higher-PRF treatments (1000 Hz and 10000 Hz) and the lower-PRF treatments (1–100 Hz), which also explained differences in treatment outcomes. We found that longer pulses and lower-PRF treatments were more effective at creating a contiguous ablation volume at doses ≥30 seconds per point. In contrast, shorter-pulse, higher-PRF treatments resulted in liquefied pockets of damage interspersed with intact tissue, rather than a fully contiguous volume, which is typically expected from histotripsy. These findings were supported by phase contrast microscopy scans that showed clear contrast between fully liquified volumes vs intact tissue.

Additionally, we explored the novel use of open-top light sheet microscopy to estimate lesion volumes and correlated these measurements with B-mode imaging. However, B-mode remained the primary method for establishing treatment volumes and volumetric rates. Volume

estimates for fully liquefied treatments were more accurate due to a robust measurement approach using two orthogonal B-mode scans. Among the longer pulse durations, 1ms produced the maximum liquified volume and showed the highest decrease in stiffness The volumetric rates reported in this study for the two longer pulse durations 1 ms (9 ± 1.7 mm^3/min) and 10 ms (4.5 ± 0.7 mm^3/min)—aligned with trends observed in ex vivo prostate studies measured via histology[148].

Shear wave elastography once again demonstrated a >75% difference in stiffness between fully treated regions and untreated areas. These findings confirmed that SWE is a valuable tool for optimizing treatments and the response of the phantom to treatments closely mimics treatment responses in fibrous tissue, making it an ideal model for optimizing treatments.

The Key contributions of this dissertation are summarized below:

Development of a Tunable Double-Network Hydrogel

- We introduced a tunable double-network hydrogel with properties similar to the prostate, as measured in this dissertation. Additionally, this hydrogel can be adjusted to mimic other fibrous tissues.

Identification of Alternative Treatment Parameters

- We identified alternative treatment parameters—lower PRF and longer duration—that are more effective at ablating fibrous ex vivo human prostate tissue and the fibrous-mimicking double-network hydrogel with a lower dose, in comparison to the standard clinical parameters.

Establishment of Quantitative Treatment Metrics

- In addition to qualitative evaluation, we established definitive quantitative metrics using shear wave elastography (SWE) to determine when treatment is complete. This allows for

personalized treatment optimization and reduces procedure time, which is particularly crucial in debulking conditions such as benign prostatic hyperplasia (BPH).

Introduction of HLQE for Automated Lesion Quantification

- We introduced HLQE, an automated lesion quantification method that provides a more reliable and objective comparison of treatment outcomes than qualitative histological analysis alone.

7.2 FUTURE WORK

While these double-network hydrogels demonstrated superior equivalence to fibrous tissue compared to pure agarose gels or individual polyacrylamide or alginate-based gels, their low attenuation does not adequately replicate the thermal effects caused by ultrasound absorption in tissue, as observed in some of the ex vivo results in this study. Future iterations of these phantoms could incorporate additives to enhance attenuation and better simulate the thermal response seen in biological tissues. Future iterations of these phantoms could explore additives to achieve higher attenuation values, better simulating these effects. Additionally, benign prostatic hyperplasia (BPH) is inherently anisotropic, whereas the hydrogels developed in this study are relatively isotropic. To further enhance the mimicry of fibrous tissues, such as uterine fibroids, tendons and BPH-affected prostate tissue, additives like mesoporous silica particles[182] could be incorporated into the hydrogel formulation. These particles can help improve mechanical properties and introduce structural anisotropy, making the phantom more representative of actual biological tissues. Additionally, procedural modifications such as controlled stretching, air drying, and swelling with water could further enhance anisotropy, better replicating the characteristics of fibrous tissues.

The volumetric rates achieved in this study are still far from being useful for debulking applications. An ideal rate would be between 100-150 mm^3/min, as the resection requirements vary by patient and the current size of the prostate[48]. One approach to increasing the treatment rate would be to optimize the outcomes of high-PRF treatments. A study by Simon et al[39]. demonstrated that increasing PRF can improve efficiency if pulse parameters are carefully designed.

To mitigate cavitation memory effects, continuous electronic steering of the bubble cloud to an adjacent location, followed by a return to the original site once the bubbles have dissolved, could be employed. This strategy requires an advanced understanding of bubble dissolution times, which was initially intended to be explored in this dissertation but ultimately fell outside its scope. Investigating dissolution times through power Doppler studies could help optimize PRF, ensuring cavitation occurs at random locations rather than repeatedly exciting nuclei in the same spot.

In Chapter 6, we demonstrated that high-PRF treatments with 1-cycle and 10-cycle pulses create damage, but the effect is dispersed, forming notch-like patterns. Additionally, the total damage volume from these high-PRF treatments was greater than that of longer-pulse, lower-PRF treatments, whereas the latter can produce a contiguous liquified volume. A potential strategy could be to alternate between high-PRF shorter pulses and low-PRF longer pulses in a combinational approach to see if that could enhance treatment outcomes.

One advanced strategy that was proposed initially but not tested is bubble deletion by bubble coalescence. Since it primarily relies on secondary Bjerknes forces, which may or may not occur in fully intact, stiff tissues, it was not tested in this study. While studies have shown promising results in agarose phantoms[61,157] potentially due to the faster liquefaction of the gel which in turn aided in better bubble coalescence. Future research is needed to determine whether similar responses can be observed in tougher, fibrous tissues.

It is also possible that liquefaction could occur at lower doses, as the initial stiffness of the tissue may influence treatment outcomes a time point that was not explored in Chapter 6 studies. A more effective approach would involve continuous monitoring to inform the provider when the treatment is complete. One way to achieve this is through shear wave elastography (SWE). In this dissertation, we relied on an external system that performed independent SWE measurements, separate from the treatment procedure. These measurements were taken at different intervals after delivering a fixed dose of treatment, making it difficult to determine the exact moment when treatment was complete. To address this limitation, SWE should be implemented with an in-plane transducer capable of measuring stiffness in the treatment region both before, during, and immediately after the procedure. This real-time feedback could optimize treatment efficiency and ensure precise endpoint detection, a technique that is already in development by other members in our lab. Doppler based velocity monitoring [167] also has been in development and could be a useful tool in measuring treatment outcomes.

Most treatments in this study used fixed pulse dosing and grid spacing with half beamwidth(-6dB) overlap. However, different grid spacing strategies remain unexplored and could potentially accelerate treatment times and optimize treatment efficiency. In the case of prostate treatments, it is also essential to develop transrectal transducer approach for clinical application.

Although most experiments were conducted on ex vivo prostate tissue, it would be valuable to extend the findings of longer pulse duration treatments to other fibrous tissues, such as uterine fibroids, ureteroceles, and tendons. Additionally, translating the results from Chapter 6 into ex vivo prostate and subsequently into in-vivo models would be crucial for identifying the most effective parameters before clinical implementation.

BIBLIOGRAPHY

1. Haar, G. T. & Coussios, C. High intensity focused ultrasound: physical principles and devices. *Int J Hyperthermia* **23**, 89–104 (2007).
2. Xu, Z. Controlled ultrasound tissue erosion. (2005).
3. Parsons, J. E., Cain, C. A., Abrams, G. D. & Fowlkes, J. B. Pulsed cavitational ultrasound therapy for controlled tissue homogenization. *Ultrasound in Medicine and Biology* **32**, 115–129 (2006).
4. Simon, J. C. *et al.* Investigation into the Mechanisms of Tissue Atomization by High-Intensity Focused Ultrasound. *Ultrasound in Medicine & Biology* **41**, 1372–1385 (2015).
5. Leighton, T. G. & Apfel, R. E. *The Acoustic Bubble*. *The Journal of the Acoustical Society of America* **96**, 2616–2616 (1994).
6. Maxwell, A. D. *et al.* Cavitation clouds created by shock scattering from bubbles during histotripsy. *The Journal of the Acoustical Society of America* **130**, 1888–1898 (2011).
7. Canney, M. S., Khokhlova, V. A., Bessonova, O. V., Bailey, M. R. & Crum, L. A. Shock-Induced Heating and Millisecond Boiling in Gels and Tissue Due to High Intensity Focused Ultrasound. *Ultrasound in Medicine and Biology* **36**, 250–267 (2010).
8. Khokhlova, T. D. *et al.* Controlled tissue emulsification produced by high intensity focused ultrasound shock waves and millisecond boiling. *The Journal of the Acoustical Society of America* **130**, 3498–3510 (2011).
9. Simon, J. C. *et al.* Ultrasonic atomization of tissue and its role in tissue fractionation by high intensity focused ultrasound. *Phys. Med. Biol.* **57**, 8061 (2012).
10. Kreider, W. *et al.* Rectified growth of histotripsy bubbles. *Proceedings of Meetings on Acoustics* **19**, 1–6 (2013).

11. Pahk, K. J., de Andrade, M. O., Gélat, P., Kim, H. & Saffari, N. Mechanical damage induced by the appearance of rectified bubble growth in a viscoelastic medium during boiling histotripsy exposure. *Ultrasonics Sonochemistry* **53**, 164–177 (2019).

12. Maxwell, A. D., Cain, C. A., Hall, T. L., Fowlkes, J. B. & Xu, Z. Probability of Cavitation for Single Ultrasound Pulses Applied to Tissues and Tissue-Mimicking Materials. *Ultrasound in Medicine and Biology* **39**, 449–465 (2013).

13. Lin, K. W. *et al.* Histotripsy beyond the intrinsic cavitation threshold using very short ultrasound pulses: Microtripsy. *IEEE Transactions on Ultrasonics, Ferroelectrics, and Frequency Control* **61**, 251–265 (2014).

14. Eranki, A. *et al.* Mechanical fractionation of tissues using microsecond-long HIFU pulses on a clinical MR-HIFU system. *International Journal of Hyperthermia* **34**, 1213–1224 (2018).

15. Ponomarchuk, E. M. *et al.* Ultrastructural Analysis of Volumetric Histotripsy Bio-effects in Large Human Hematomas. *Ultrasound in Medicine & Biology* **47**, 2608–2621 (2021).

16. Khokhlova, T. D. *et al.* Histotripsy liquefaction of large hematomas. *Ultrasound in Medicine and Biology* **42**, 1491–1498 (2016).

17. Kim, Y. *et al.* Developmental Impact and Lesion Maturation of Histotripsy-Mediated Non-Invasive Tissue Ablation in a Fetal Sheep Model. *Ultrasound in Medicine and Biology* **39**, 1047–1055 (2013).

18. Matula, T. J. *et al.* Histotripsy Treatment of Abscesses. in *2020 IEEE International Ultrasonics Symposium (IUS)* 1–4 (2020). doi:10.1109/IUS46767.2020.9251683.

19. Schade, G. R. *et al.* Histotripsy focal ablation of implanted prostate tumor in an ACE-1 canine cancer model. *Journal of Urology* **188**, 1957–1964 (2012).

20. Khokhlova, T. D. *et al.* Pilot in vivo studies on transcutaneous boiling histotripsy in porcine liver and kidney. *Scientific Reports* **9**, 1–12 (2019).

21. Roberts, W. W. *et al.* Pulsed cavitational ultrasound: A noninvasive technology for controlled tissue ablation (histotripsy) in the rabbit kidney. *Journal of Urology* **175**, (2006).

22. Khokhlova, T. D. *et al.* Ultrasound-guided tissue fractionation by high intensity focused ultrasound in an in vivo porcine liver model. *Proceedings of the National Academy of Sciences of the United States of America* **111**, 8161–8166 (2014).

23. Maxwell, A. D. *et al.* Noninvasive treatment of deep venous thrombosis using pulsed ultrasound cavitation therapy (histotripsy) in a porcine model. *Journal of Vascular and Interventional Radiology* **22**, 369–377 (2011).

24. Hall, T. L. *et al.* Histotripsy of rabbit renal tissue in vivo : Temporal histologic trends. *Journal of Endourology* **21**, 1159–1165 (2007).

25. Knott, E. A. *et al.* Robotically-Assisted Sonic Therapy for Renal Ablation in a Live Porcine Model: Initial Preclinical Results. *Journal of Vascular and Interventional Radiology* **30**, 1293–1302 (2019).

26. Vlaisavljevich, E. *et al.* Image-Guided Non-Invasive Ultrasound Liver Ablation Using Histotripsy: Feasibility Study in an In Vivo Porcine Model. *Ultrasound in Medicine and Biology* **39**, 1398–1409 (2013).

27. Sukovich, J. R. *et al.* In vivo histotripsy brain treatment. *Journal of Neurosurgery* **131**, 1331–1338 (2018).

28. Vlaisavljevich, E. *et al.* Image-guided non-invasive ultrasound liver ablation using histotripsy: Feasibility study in an invivo porcine model. *Ultrasound in Medicine and Biology* **39**, 1398–1409 (2013).

29. Wang, Y.-N. *et al.* Mechanical decellularization of tissue volumes using boiling histotripsy. *Phys. Med. Biol.* **63**, 235023 (2018).

30. Schade, G. R., Hall, T. L. & Roberts, W. W. Urethral-sparing histotripsy of the prostate in a canine model. *Urology* **80**, 730–735 (2012).

31. Wang, Y.-N. *et al.* Pilot evaluation of histotripsy treatment for Peyronie's disease. *The Journal of the Acoustical Society of America* **140**, 3031–3031 (2016).

32. D MaxwellAdam *et al.* Noninvasive Ureterocele Puncture Using Pulsed Focused Ultrasound: An In Vitro Study. *Journal of Endourology* **28**, 342–346 (2014).

33. Hendricks-Wenger, A. *et al.* Histotripsy for the Treatment of Cholangiocarcinoma in a Patient-Derived Xenograft Mouse Model. *Ultrasound in Medicine & Biology* **48**, 293–303 (2022).

34. Simon, A. *et al.* Histotripsy for the Treatment of Uterine Leiomyomas: A Feasibility Study in Ex Vivo Uterine Fibroids. *Ultrasound in Medicine & Biology* **48**, 1652–1662 (2022).

35. Vlaisavljevich, E. *et al.* Effects of tissue stiffness, ultrasound frequency, and pressure on histotripsy-induced cavitation bubble behavior. *Physics in Medicine and Biology* **60**, 2271–2292 (2015).

36. Hall, T. L. *et al.* Histotripsy of the Prostate: Dose Effects in a Chronic Canine Model. *Urology* **74**, 932–937 (2009).

37. Definition of fibrous connective tissue - NCI Dictionary of Cancer Terms - NCI. https://www.cancer.gov/publications/dictionaries/cancer-terms/def/fibrous-connective-tissue (2011).

38. Kamrani, P., Marston, G., Arbor, T. C. & Jan, A. Anatomy, Connective Tissue. in *StatPearls* (StatPearls Publishing, Treasure Island (FL), 2025).

39. Simon, A. *et al.* Histotripsy for the Treatment of Uterine Leiomyomas: A Feasibility Study in Ex Vivo Uterine Fibroids. *Ultrasound in Medicine & Biology* **48**, 1652–1662 (2022).

40. Maxwell, A. D., Hsi, R. S., Bailey, M. R., Casale, P. & Lendvay, T. S. Noninvasive ureterocele puncture using pulsed focused ultrasound: An in vitro study. *Journal of Endourology* **28**, 342–346 (2014).

41. Awedew, A. F. *et al.* The global, regional, and national burden of benign prostatic hyperplasia in 204 countries and territories from 2000 to 2019: a systematic analysis for the Global Burden of Disease Study 2019. *The Lancet Healthy Longevity* **3**, e754–e776 (2022).

42. Urologic Diseases in America: Annual Data Report.

43. Verze, P., Cai, T. & Lorenzetti, S. The role of the prostate in male fertility, health and disease. *Nature Reviews Urology* **13**, 379–386 (2016).

44. Hammer, S. J. *et al.* Quantitative mechanical assessment of the whole prostate gland ex vivo using dynamic instrumented palpation. *Proceedings of the Institution of Mechanical Engineers, Part H: Journal of Engineering in Medicine* **231**, 1081–1100 (2017).

45. Russell, D. W. & Wilson, J. D. Steroid 5 alpha-reductase: two genes/two enzymes. *Annu Rev Biochem* **63**, 25–61 (1994).

46. Kaplan, S. A. Factors in Predicting Failure with Medical Therapy for BPH. *Rev Urol* **7**, S34–S39 (2005).

47. Yu, Z.-J. *et al.* Efficacy and Side Effects of Drugs Commonly Used for the Treatment of Lower Urinary Tract Symptoms Associated With Benign Prostatic Hyperplasia. *Front Pharmacol* **11**, 658 (2020).

48. Leslie, S. W., Chargui, S. & Stormont, G. Transurethral Resection of the Prostate. in *StatPearls* (StatPearls Publishing, Treasure Island (FL), 2025).

49. Persu, C. *et al.* TURP for BPH. How Large is Too Large? *J Med Life* **3**, 376–380 (2010).

50. Rassweiler, J., Teber, D., Kuntz, R. & Hofmann, R. Complications of Transurethral Resection of the Prostate (TURP)—Incidence, Management, and Prevention. *European Urology* **50**, 969–980 (2006).

51. Roberts, W. W. *et al.* Histotripsy of the prostate using a commercial system in a canine model. *Journal of Urology* **191**, 860–865 (2014).

52. Schuster, T. G., Wei, J. T., Hendlin, K., Jahnke, R. & Roberts, W. W. Histotripsy Treatment of Benign Prostatic Enlargement Using the Vortx Rx System: Initial Human Safety and Efficacy Outcomes. *Urology* **114**, 184–187 (2018).

53. Nanda Kumar, Y. *et al.* Development of Tough Hydrogel Phantoms to Mimic Fibrous Tissue for Focused Ultrasound Therapies. *Ultrasound Med Biol* **48**, 1762–1777 (2022).

54. Singh, Z. *et al.* Mp04-02 analysis of ex-vivo human bph tissue treated by histotripsy: dose and parameter effects. *Journal of Urology* **207**, e56 (2022).

55. Maxwell, A. D. *et al.* A tissue phantom for visualization and measurement of ultrasound-induced cavitation damage. *Ultrasound in Medicine and Biology* **36**, (2010).

56. Edsall, C., Ham, E., Holmes, H., Hall, T. L. & Vlaisavljevich, E. Effects of frequency on bubble-cloud behavior and ablation efficiency in intrinsic threshold histotripsy. *Phys. Med. Biol.* **66**, 225009 (2021).

57. Simon, A., Edsall, C., Maxwell, A. & Vlaisavljevich, E. Effects of pulse repetition frequency on bubble cloud characteristics and ablation in single-cycle histotripsy. *Phys. Med. Biol.* **69**, 025018 (2024).

58. Edsall, C. *et al.* Bubble Cloud Behavior and Ablation Capacity for Histotripsy Generated from Intrinsic or Artificial Cavitation Nuclei. *Ultrasound in Medicine & Biology* **47**, 620–639 (2021).

59. Lin, K.-W. *et al.* Dual-beam histotripsy: a low-frequency pump enabling a high-frequency probe for precise lesion formation. *IEEE Transactions on Ultrasonics, Ferroelectrics, and Frequency Control* **61**, 325–340 (2014).

60. Duryea, A., Cain, C., Tamaddoni, H., Roberts, W. & Hall, T. Removal of residual nuclei following a cavitation event using low-amplitude ultrasound. *IEEE Transactions on Ultrasonics, Ferroelectrics, and Frequency Control* **61**, 1619–1626 (2014).

61. Duryea, A. P., Tamaddoni, H. A., Cain, C. A., Roberts, W. W. & Hall, T. L. Removal of residual nuclei following a cavitation event: a parametric study. *IEEE Transactions on Ultrasonics, Ferroelectrics, and Frequency Control* **62**, 1605–1614 (2015).

62. Wang, T. Y., Xu, Z., Hall, T. L., Fowlkes, J. B. & Cain, C. A. An Efficient Treatment Strategy for Histotripsy by Removing Cavitation Memory. *Ultrasound in Medicine and Biology* **38**, 753–766 (2012).

63. Lafond, M., Payne, A. & Lafon, C. Therapeutic ultrasound transducer technology and monitoring techniques: a review with clinical examples. *International Journal of Hyperthermia* **41**, 2389288 (2024).

64. Maxwell, A. D. *et al.* A Prototype Therapy System for Transcutaneous Application of Boiling Histotripsy. *IEEE Transactions on Ultrasonics, Ferroelectrics, and Frequency Control* **64**, 1542–1557 (2017).

65. Woodacre, J. K., Landry, T. G. & Brown, J. A. Fabrication and Characterization of a 5 mm × 5 mm Aluminum Lens-Based Histotripsy Transducer. *IEEE Transactions on Ultrasonics, Ferroelectrics, and Frequency Control* **69**, 1442–1451 (2022).

66. Schade, G. *et al.* Transrectal boiling histotripsy of the prostate: Initial pre-clinical results with a prototype device. in 9–13 (7th International Symposium on Focused Ultrasound., Washington, DC, 2020).

67. Bawiec, C. R. *et al.* A Prototype Therapy System for Boiling Histotripsy in Abdominal Targets Based on a 256-Element Spiral Array. *IEEE Transactions on Ultrasonics, Ferroelectrics, and Frequency Control* **68**, 1496–1510 (2021).

68. Mallay, M. G., Landry, T. G. & Brown, J. A. An 8 mm endoscopic histotripsy array with integrated high-resolution ultrasound imaging. *Ultrasonics* **139**, 107275 (2024).

69. Williams, R. P., Simon, J. C., Khokhlova, V. A., Sapozhnikov, O. A. & Khokhlova, T. D. The histotripsy spectrum: differences and similarities in techniques and instrumentation. *International Journal of Hyperthermia* **40**, 2233720 (2023).

70. Landry, T. G. *et al.* Endoscopic Coregistered Ultrasound Imaging and Precision Histotripsy: Initial In Vivo Evaluation. *BME Frontiers* **2022**, 9794321 (2022).

71. Sapozhnikov, O. A., Tsysar, S. A., Khokhlova, V. A. & Kreider, W. Acoustic holography as a metrological tool for characterizing medical ultrasound sources and fields. *J Acoust Soc Am* **138**, 1515–1532 (2015).

72. Hurrell, A. Radiation Force Balance.

73. Bakaric, M. *et al.* Measurement of the ultrasound attenuation and dispersion in 3D-printed photopolymer materials from 1 to 3.5 MHz. *The Journal of the Acoustical Society of America* **150**, 2798–2805 (2021).

74. Drainville, A. *et al.* Transesophageal ultrasound prototype development for the treatment of pancreatic cancer. in *2023 IEEE International Ultrasonics Symposium (IUS)* 1–4 (2023). doi:10.1109/IUS51837.2023.10308291.

75. Woodacre, J. K., Landry, T. G. & Brown, J. A. A Low-Cost Miniature Histotripsy Transducer for Precision Tissue Ablation. *IEEE Transactions on Ultrasonics, Ferroelectrics, and Frequency Control* **65**, 2131–2140 (2018).

76. Hell, B. J. & Schumann, L. Treatment of Benign Prostatic Hyperplasia. *Journal of the American Association of Nurse Practitioners* **11**, 303 (1999).

77. Bortnick, E., Brown, C., Simma-Chiang, V. & Kaplan, S. A. Modern best practice in the management of benign prostatic hyperplasia in the elderly. *Therapeutic Advances in Urology* **12**, 1756287220929486 (2020).

78. Kim, Y. *et al.* Rapid prototyping fabrication of focused ultrasound transducers. *IEEE Transactions on Ultrasonics, Ferroelectrics, and Frequency Control* **61**, 1559–1574 (2014).

79. Xu, Z., Hall, T. L., Vlaisavljevich, E. & Lee, F. T. Histotripsy: the first noninvasive, non-ionizing, non-thermal ablation technique based on ultrasound. *International Journal of Hyperthermia* **38**, 561–575 (2021).

80. Yuldashev, P. V. *et al.* "HIFU Beam:" A Simulator for Predicting Axially Symmetric Nonlinear Acoustic Fields Generated by Focused Transducers in a Layered Medium. *IEEE Trans. Ultrason., Ferroelect., Freq. Contr.* **68**, 2837–2852 (2021).

81. Wear, K. A. Spatiotemporal Deconvolution of Hydrophone Response for Linear and Nonlinear Beams—Part I: Theory, Spatial-Averaging Correction Formulas, and Criteria for Sensitive Element Size. *IEEE Trans. Ultrason., Ferroelect., Freq. Contr.* **69**, 1243–1256 (2022).

82. Wear, K. A., Shah, A. & Baker, C. Spatiotemporal Deconvolution of Hydrophone Response for Linear and Nonlinear Beams—Part II: Experimental Validation. *IEEE Trans. Ultrason., Ferroelect., Freq. Contr.* **69**, 1257–1267 (2022).

83. Khokhlova, T. *et al.* Dependence of inertial cavitation induced by high intensity focused ultrasound on transducer F -number and nonlinear waveform distortion. *The Journal of the Acoustical Society of America* **144**, 1160–1169 (2018).

84. Vlaisavljevich, E., Gerhardson, T., Hall, T. & Xu, Z. Effects of f-number on the histotripsy intrinsic threshold and cavitation bubble cloud behavior. *Physics in Medicine and Biology* **62**, 1269–1290 (2017).

85. Kharine, A. *et al.* Poly(vinyl alcohol) gels for use as tissue phantoms in photoacoustic mammography. *Physics in Medicine and Biology* **48**, 357–370 (2003).

86. Pogue, B. W. & Patterson, M. S. Review of tissue simulating phantoms for optical spectroscopy, imaging and dosimetry. *Journal of Biomedical Optics* **11**, 041102 (2006).

87. Culjat, M. O., Goldenberg, D., Tewari, P. & Singh, R. S. A review of tissue substitutes for ultrasound imaging. *Ultrasound in Medicine and Biology* **36**, 861–873 (2010).

88. Madsen, E. L., Frank, G. R. & Dong, F. Liquid or solid ultrasonically tissue-mimicking materials with very low scatter. *Ultrasound in Medicine and Biology* **24**, 535–542 (1998).

89. Bush, N. L. & Hill, C. R. Gelatine-alginate complex gel: A new acoustically tissue-equivalent material. *Ultrasound in Medicine and Biology* **9**, (1983).

90. Zell, K., Sperl, J. I., Vogel, M. W., Niessner, R. & Haisch, C. Acoustical properties of selected tissue phantom materials for ultrasound imaging. *Physics in Medicine and Biology* **52**, (2007).

91. Kondo, T., Kitatuji, M., Shikinami, Y., Tuta, K. & Kanda, H. New tissue mimicking materials for ultrasound phantoms. *Proceedings - IEEE Ultrasonics Symposium* **3**, 1664–1667 (2005).

92. Cabrelli, L. C., Grillo, F. W., Sampaio, D. R. T., Carneiro, A. A. O. & Pavan, T. Z. Acoustic and Elastic Properties of Glycerol in Oil-Based Gel Phantoms. *Ultrasound in Medicine and Biology* **43**, 2086–2094 (2017).

93. Tatarinov, A., Pontaga, I. & Vilks, U. Modeling the influence of mineral content and porosity on ultrasound parameters in bone by using synthetic phantoms. *Mechanics of Composite Materials* **35**, 147–154 (1999).

94. Clarke, A. J., Evans, J. A., Truscott, J. G., Milner, R. & Smith, M. A. A phantom for quantitative ultrasound of trabecular bone. *Physics in Medicine and Biology* **39**, (1994).

95. McDonald, M., Lochhead, S., Chopra, R. & Bronskill, M. J. Multi-modality tissue-mimicking phantom for thermal therapy. *Physics in medicine and biology* **49**, 2767–2778 (2004).

96. Maxwell, A. D. *et al.* tissue phantom for measurement of US induced cavitation damage. **36**, 2132–2143 (2011).

97. Ambrogio, S. *et al.* A standard test phantom for the performance assessment of magnetic resonance guided high intensity focused ultrasound (MRgHIFU) thermal therapy devices. *International Journal of Hyperthermia* **39**, 57–68 (2022).

98. Ambrogio, S. *et al.* A Polyvinyl Alcohol-Based Thermochromic Material for Ultrasound Therapy Phantoms. *Ultrasound in Medicine & Biology* **46**, 3135–3144 (2020).

99. Eranki, A. *et al.* Tissue-mimicking thermochromic phantom for characterization of HIFU devices and applications. *International journal of hyperthermia : the official journal of*

European Society for Hyperthermic Oncology, North American Hyperthermia Group **36**, 518 (2019).

100. Morchi, L. *et al.* A Reusable Thermochromic Phantom for Testing High Intensity Focused Ultrasound Technologies. *Proceedings of the Annual International Conference of the IEEE Engineering in Medicine and Biology Society, EMBS* 1431–1434 (2021) doi:10.1109/EMBC46164.2021.9629845.
101. Hori, R. Y. & Lewis, J. L. Mechanical properties of the fibrous tissue found at the bone-cement interface following total joint replacement. *Journal of Biomedical Materials Research* **16**, 911–927 (1982).
102. Sun, J. Y. *et al.* Highly stretchable and tough hydrogels. *Nature* **489**, 133–136 (2012).
103. Rodriguez-Nieves, J. A. & Macoska, J. A. Prostatic fibrosis, lower urinary tract symptoms, and BPH. *Nature reviews. Urology* **10**, 546 (2013).
104. Hempel, C. R. *et al.* Histotripsy fractionation of prostate tissue: Local effects and systemic response in a canine model. *Journal of Urology* **185**, (2011).
105. Schuster, T. G., Wei, J. T., Hendlin, K., Jahnke, R. & Roberts, W. W. Histotripsy Treatment of Benign Prostatic Enlargement Using the Vortx Rx System: Initial Human Safety and Efficacy Outcomes. *Urology* **114**, 184–187 (2018).
106. Zhang, J. *et al.* Animal models of benign prostatic hyperplasia. *Prostate Cancer and Prostatic Diseases* **24**, 49–57 (2021).
107. Shapiro, E., Becich, M. J., Hartanto, V. & Lepor, H. The relative proportion of stromal and epithelial hyperplasia is related to the development of symptomatic benign prostate hyperplasia. *Journal of Urology* **147**, (1992).

108. Wang, Y.-N. *et al.* MECHANICAL DECELLULARIZATION OF TISSUE VOLUMES USING BOILING HISTOTRIPSY. *Physics in medicine and biology* **63**, 235023 (2018).

109. Vlaisavljevich, E. *et al.* Effects of tissue mechanical properties on susceptibility to histotripsy-induced tissue damage. *Physics in Medicine and Biology* **59**, 253–270 (2014).

110. Mancia, L. *et al.* Modeling tissue-selective cavitation damage. *Physics in Medicine and Biology* **64**, (2019).

111. Mancia, L., Vlaisavljevich, E., Xu, Z. & Johnsen, E. Predicting Tissue Susceptibility to Mechanical Cavitation Damage in Therapeutic Ultrasound. *Ultrasound in Medicine and Biology* **43**, 1421–1440 (2017).

112. Wells, R. G. Tissue Mechanics and Fibrosis. *Biochimica et biophysica acta* **1832**, 884 (2013).

113. Ishigooka, M. *et al.* Relative and total volume of histological components in benign prostatic hyperplasia: Relationships between histological components and clinical findings. *Prostate* **29**, (1996).

114. Yang, S. *et al.* High-intensity focused ultrasound ablation: An in vitro agarose gel model. *International Journal of Clinical and Experimental Medicine* **10**, 15302–15308 (2017).

115. Stewart, E. A. *et al.* Uterine fibroids. *Nature Reviews Disease Primers* **2**, (2016).

116. Moreland, R. B. & Nehra, A. Pathophysiology of Peyronie's disease. *International Journal of Impotence Research* **14**, (2002).

117. Schuppan, D. & Afdhal, N. H. Liver cirrhosis. *The Lancet* **371**, 838–851 (2008).

118. Hendricks-Wenger, A. *et al.* Histotripsy for the Treatment of Cholangiocarcinoma Liver Tumors: In Vivo Feasibility and Ex Vivo Dosimetry Study. *IEEE transactions on ultrasonics, ferroelectrics, and frequency control* **68**, 2953–2964 (2021).

119. Discher, D. E., Mooney, D. J. & Zandstra, P. W. Growth factors, matrices, and forces combine and control stem cells. *Science (New York, N.Y.)* **324**, 1673 (2009).

120. Gong, J. P., Katsuyama, Y., Kurokawa, T. & Osada, Y. Double-network hydrogels with extremely high mechanical strength. *Advanced Materials* **15**, 1155–1158 (2003).

121. Yang, C. H. *et al.* Strengthening alginate/polyacrylamide hydrogels using various multivalent cations. *ACS Applied Materials and Interfaces* **5**, 10418–10422 (2013).

122. Bt Ibrahim, S. F., Mohd Azam, N. A. N. & Amin, K. A. M. Sodium alginate film: The effect of crosslinker on physical and mechanical properties. *IOP Conference Series: Materials Science and Engineering* **509**, (2019).

123. Jianhai, Y., Chen, Y. M., Zhou, J. & Suo, Z. Strengthening Alginate/Polyacrylamide Hydrogels Using Various Multivalent Cations. (2013) doi:10.1021/am403966x.

124. Dunmire, B., Kucewicz, J. C., Mitchell, S. B., Crum, L. A. & Sekins, K. M. Characterizing an Agar/Gelatin phantom for image guided dosing and feedback control of high-intensity focused ultrasound. *Ultrasound in Medicine and Biology* **39**, 300–311 (2013).

125. Choi, I. & Shield, R. T. Second-order effects in problems for a class of elastic materials. *Zeitschrift für angewandte Mathematik und Physik ZAMP 1981 32:4* **32**, 361–381 (1981).

126. Guntur, S. R. & Choi, M. J. An Improved Tissue-Mimicking Polyacrylamide Hydrogel Phantom for Visualizing Thermal Lesions with High-Intensity Focused Ultrasound. *Ultrasound in Medicine and Biology* **40**, 2680–2691 (2014).

127. Khokhlova, T. D. *et al.* Effect of Stiffness of Large Extravascular Hematomas on Their Susceptibility to Boiling Histotripsy Liquefaction in Vitro. *Ultrasound in Medicine and Biology* **46**, 2007–2016 (2020).

128. Szabo, T. L. Diagnostic Ultrasound Imaging: Inside Out: Second Edition. *Diagnostic Ultrasound Imaging: Inside Out: Second Edition* 1–549 (2004).

129. Roberts, W. W. *et al.* Histotripsy of the prostate using a commercial system in a canine model. *Journal of Urology* **191**, 860–865 (2014).

130. Wang, T. Y., Hall, T. L., Xu, Z., Fowlkes, J. B. & Cain, C. A. Imaging feedback of histotripsy treatments using ultrasound transient elastography. *IEEE International Ultrasonics Symposium, IUS* 2233–2236 (2011) doi:10.1109/ULTSYM.2011.0554.

131. Worthington, A. E., Trachtenberg, J. & Sherar, M. D. Ultrasound properties of human prostate tissue during heating. *Ultrasound in Medicine and Biology* **28**, 1311–1318 (2002).

132. Lin, K. W., Hall, T., McGough, R., Xu, Z. & Cain, C. Synthesis of monopolar ultrasound pulses for therapy: The frequency-compounding transducer. *IEEE Transactions on Ultrasonics, Ferroelectrics, and Frequency Control* **61**, 1123–1136 (2014).

133. Yamanaka, T. *et al.* Boiling histotripsy-induced mechanical ablation modulates tumour microenvironment by promoting immunogenic cell death of cancers. *Annals of Oncology* **30**, v20–v21 (2019).

134. Khokhlova, T. D. *et al.* Dependence of Boiling Histotripsy Treatment Efficiency on HIFU Frequency and Focal Pressure Levels. *Ultrasound in Medicine and Biology* **43**, 1975–1985 (2017).

135. Guan, Y. *et al.* Histotripsy Produced by Hundred-Microsecond-Long Focused Ultrasonic Pulses: A Preliminary Study. *Ultrasound in Medicine and Biology* **42**, 2232–2244 (2016).

136. Geoghegan, R. *et al.* A Tissue-Mimicking Prostate Phantom for 980nm Laser Interstitial Thermal Therapy. *International journal of hyperthermia : the official journal of European Society for Hyperthermic Oncology, North American Hyperthermia Group* **36**, 993 (2019).

137. Schade, G. R., Styn, N. R., Ives, K. A., Hall, T. L. & Roberts, W. W. Prostate histotripsy: Evaluation of prostatic urethral treatment parameters in a canine model. *BJU International* **113**, 498–503 (2014).

138. Maxwell, A. D. *et al.* A tissue phantom for visualization and measurement of ultrasound-induced cavitation damage. *Ultrasound in Medicine and Biology* **36**, 2132–2143 (2010).

139. Choi, M. J., Guntur, S. R., Lee, K. I. L., Paeng, D. G. & Coleman, A. A Tissue Mimicking Polyacrylamide Hydrogel Phantom for Visualizing Thermal Lesions Generated by High Intensity Focused Ultrasound. *Ultrasound in Medicine and Biology* **39**, 439–448 (2013).

140. Bercoff, J. *et al.* ShearWaveTM elastography: A new real time imaging mode for assessing quantitatively soft tissue viscoelasticity. *Proceedings - IEEE Ultrasonics Symposium* 321–324 (2008) doi:10.1109/ULTSYM.2008.0079.

141. Wang, T. Y., Hall, T. L., Xu, Z., Fowlkes, J. B. & Cain, C. A. Imaging feedback of histotripsy treatments using ultrasound shear wave elastography. *IEEE Transactions on Ultrasonics, Ferroelectrics, and Frequency Control* **59**, 1167–1181 (2012).

142. Khokhlova, T. D. *et al.* Dependence of Boiling Histotripsy Treatment Efficiency on HIFU Frequency and Focal Pressure Levels. *Ultrasound in Medicine and Biology* **43**, 1975–1985 (2017).

143. Wilson, C. T. *et al.* Comparative study of the dynamics of laser and acoustically generated bubbles in viscoelastic media. *Physical Review E* **99**, (2019).

144. Hollingsworth, J. M. & Wei, J. T. Economic Impact of Surgical Intervention in the Treatment of Benign Prostatic Hyperplasia. *Rev Urol* **8**, S9–S15 (2006).

145. Roehrborn, C. G. Benign Prostatic Hyperplasia: An Overview. *Rev Urol* **7**, S3–S14 (2005).

146. Launer, B. M., McVary, K. T., Ricke, W. A. & Lloyd, G. L. The rising worldwide impact of benign prostatic hyperplasia. *BJU Int* **127**, 722–728 (2021).

147. Childs, M. A. *et al.* Pathogenesis of Bladder Calculi in the Presence of Urinary Stasis. *J Urol* **189**, 1347–1351 (2013).

148. Khokhlova, V. A. *et al.* Initial Assessment of Boiling Histotripsy for Mechanical Ablation of Ex Vivo Human Prostate Tissue. *Ultrasound in Medicine and Biology* **49**, 62–71 (2023).

149. Hall, T. & Cain, C. A Low Cost Compact 512 Channel Therapeutic Ultrasound System For Transcutaneous Ultrasound Surgery. *AIP Conference Proceedings* **829**, 445–449 (2006).

150. Khokhlova, T. *et al.* Dependence of inertial cavitation induced by high intensity focused ultrasound on transducer F-number and nonlinear waveform distortion. *The Journal of the Acoustical Society of America* **144**, 1160–1169 (2018).

151. Zhou, Y. & Wang, X. Effect of pulse duration and pulse repetition frequency of cavitation histotripsy on erosion at the surface of soft material. *Ultrasonics* **84**, 296–309 (2018).

152. Schuster, T. G., Wei, J. T., Hendlin, K., Jahnke, R. & Roberts, W. W. Histotripsy Treatment of Benign Prostatic Enlargement Using the Vortx Rx System: Initial Human Safety and Efficacy Outcomes. *Urology* **114**, 184–187 (2018).

153. Pahk, K. J., Gélat, P., Sinden, D., Dhar, D. K. & Saffari, N. Numerical and Experimental Study of Mechanisms Involved in Boiling Histotripsy. *Ultrasound in Medicine & Biology* **43**, 2848–2861 (2017).

154. Nanda Kumar, Y. *et al.* Bubble cloud progression in fibrous tissue mimicking hydrogels at different histotripsy sonications. *The Journal of the Acoustical Society of America* **150**, A29–A29 (2021).

155. Vlaisavljevich, E. *et al.* Effects of tissue mechanical properties on susceptibility to histotripsy-induced tissue damage. *Phys. Med. Biol.* **59**, 253 (2013).

156. Vlaisavljevich, E. *et al.* Histotripsy-induced cavitation cloud initiation thresholds in tissues of different mechanical properties. *IEEE Transactions on Ultrasonics, Ferroelectrics, and Frequency Control* **61**, 341–352 (2014).

157. Duryea, A. P. *et al.* Removal of residual cavitation nuclei to enhance histotripsy fractionation of soft tissue. *IEEE Transactions on Ultrasonics, Ferroelectrics, and Frequency Control* **62**, 2068–2078 (2015).

158. Wang, T.-Y., Xu, Z., Hall, T. L., Fowlkes, J. B. & Cain, C. A. An Efficient Treatment Strategy for Histotripsy by Removing Cavitation Memory. *Ultrasound in Medicine & Biology* **38**, 753–766 (2012).

159. Shi, A. *et al.* Integrated Histotripsy and Bubble Coalescence Transducer for Thrombolysis. *Ultrasound in Medicine & Biology* **44**, 2697–2709 (2018).

160. Wang, Y.-N. *et al.* MECHANICAL DECELLULARIZATION OF TISSUE VOLUMES USING BOILING HISTOTRIPSY. *Physics in medicine and biology* **63**, 235023 (2018).

161. Wang, Y.-N., Khokhlova, T., Bailey, M., Hwang, J. H. & Khokhlova, V. Histological and biochemical analysis of mechanical and thermal bioeffects in boiling histotripsy lesions induced by high intensity focused ultrasound. *Ultrasound Med Biol* **39**, 424–438 (2013).

162. Sang, L., Wang, X., Xu, D. & Cai, Y. Accuracy of shear wave elastography for the diagnosis of prostate cancer: A meta-analysis. *Sci Rep* **7**, 1949 (2017).

163. Ji, Y. *et al.* Stiffness of prostate gland measured by transrectal real-time shear wave elastography for detection of prostate cancer: a feasibility study. *Br J Radiol* **92**, 20180970 (2019).

164. Ahmad, S., Cao, R., Varghese, T., Bidaut, L. & Nabi, G. Transrectal quantitative shear wave elastography in the detection and characterisation of prostate cancer. *Surg Endosc* **27**, 3280–3287 (2013).

165. Barr, R. G. *et al.* WFUMB Guidelines and Recommendations on the Clinical Use of Ultrasound Elastography: Part 5. Prostate. *Ultrasound in Medicine & Biology* **43**, 27–48 (2017).

166. Miller, R. M., Zhang, X., Maxwell, A. D., Cain, C. A. & Xu, Z. Bubble-Induced Color Doppler Feedback for Histotripsy Tissue Fractionation. *IEEE Transactions on Ultrasonics, Ferroelectrics, and Frequency Control* **63**, 408–419 (2016).

167. Song, M. *et al.* Quantitative Assessment of Boiling Histotripsy Progression Based on Color Doppler Measurements. *IEEE Transactions on Ultrasonics, Ferroelectrics, and Frequency Control* **69**, 3255–3269 (2022).

168. Thomas, G. P. L., Khokhlova, T. D., Sapozhnikov, O. A. & Khokhlova, V. A. Enhancement of Boiling Histotripsy by Steering the Focus Axially During the Pulse Delivery. *IEEE Transactions on Ultrasonics, Ferroelectrics, and Frequency Control* 1–1 (2023) doi:10.1109/TUFFC.2023.3286759.

169. Vlaisavljevich, E. *et al.* Effects of Ultrasound Frequency and Tissue Stiffness on the Histotripsy Intrinsic Threshold for Cavitation. *Ultrasound in Medicine and Biology* **41**, 1651–1667 (2015).

170. Ponomarchuk, E. *et al.* Pilot Study on Boiling Histotripsy Treatment of Human Leiomyoma Ex Vivo. *Ultrasound in Medicine & Biology* S0301562924002072 (2024) doi:10.1016/j.ultrasmedbio.2024.05.002.

171. Rosnitskiy, P. B. *et al.* Pilot ex vivo study on non-thermal ablation of human prostate adenocarcinoma tissue using boiling histotripsy. *Ultrasonics* **133**, 107029 (2023).

172. Kumar, Y. N. *et al.* A comparative study of histotripsy parameters for the treatment of fibrotic ex-vivo human benign prostatic hyperplasia tissue. *Sci Rep* **14**, 20365 (2024).

173. Xu, Z. *et al.* High Speed Imaging of Bubble Clouds Generated in Pulsed Ultrasound Cavitational Therapy - Histotripsy. *IEEE Transactions on Ultrasonics, Ferroelectrics, and Frequency Control* **54**, 2091–2101 (2007).

174. Effects of acoustic parameters on bubble cloud dynamics in ultrasound tissue erosion (histotripsy) | The Journal of the Acoustical Society of America | AIP Publishing. https://pubs.aip.org/asa/jasa/article/122/1/229/812630/Effects-of-acoustic-parameters-on-bubble-cloud.

175. Pahk, K. J., Gélat, P., Kim, H. & Saffari, N. Bubble dynamics in boiling histotripsy. *Ultrasound in Medicine and Biology* **44**, 2673–2696 (2018).

176. Ambekar, P. A. *et al.* Histotripsy-Induced Bactericidal Activity Correlates to Size of Cavitation Cloud In Vitro. *IEEE Transactions on Ultrasonics, Ferroelectrics, and Frequency Control* **71**, 1868–1878 (2024).

177. A hybrid open-top light-sheet microscope for versatile multi-scale imaging of cleared tissues | Nature Methods. https://www.nature.com/articles/s41592-022-01468-5.

178. Bishop, K. W. *et al.* An end-to-end workflow for nondestructive 3D pathology. *Nat Protoc* **19**, 1122–1148 (2024).

179. BigStitcher: reconstructing high-resolution image datasets of cleared and expanded samples | Nature Methods. https://www.nature.com/articles/s41592-019-0501-0.

180. Schindelin, J. *et al.* Fiji: an open-source platform for biological-image analysis. *Nature Methods* **9**, 676–682 (2012).

181. Shi, A. *et al.* Integrated Histotripsy and Bubble Coalescence Transducer for Rapid Tissue Ablation. *IEEE Trans. Ultrason., Ferroelect., Freq. Contr.* **65**, 1822–1831 (2018).

182. Choi, S. *et al.* Tendon-mimicking anisotropic alginate-based double-network composite hydrogels with enhanced mechanical properties and high impact absorption. *Carbohydrate Polymers* **352**, 123193 (2025).

183. Thanh, D. N. H., Thanh, L. T., Erkan, U., Khamparia, A. & Prasath, V. B. S. Dermoscopic image segmentation method based on convolutional neural networks. *International Journal of Computer Applications in Technology* **66**, 89–99 (2021).

184. Crum, W. R., Camara, O. & Hill, D. L. G. Generalized Overlap Measures for Evaluation and Validation in Medical Image Analysis. *IEEE Transactions on Medical Imaging* **25**, 1451–1461 (2006).

APPENDIX A

Methods: Histotripsy Lesion Quantification by Entropy Analysis (HLQE)

The following text describes a step-by-step approach on how the lesion quantification algorithm was utilized to quantify the tissue damage.

Step 1: Selecting the ROI:

1. An unprocessed image (entire slide scan of a Masson's trichrome stained tissue slice) to be analyzed was loaded into MATLAB, and a region of interest (ROI) X2 was chosen based on the therapy grid size delivered.

Step 2: Entropy filtering:

2. The entropy filter was independently applied to a 25x25 pixel neighborhood across the three red, green and blue channels of the original ROI image. This neighborhood size was chosen to possess sufficient resolution for differentiating lesion vs intact tissue with minimal loss of accuracy.
3. The resulting arrays contained the calculated entropy value in the neighborhood around the corresponding pixel from the ROI across the three channels. The arrays were then multiplied to get the overall entropy map.

Step 3: Binarization:

1. From the entropy map image, a binarization reference frame was chosen to encapsulate regions containing both lesion and intact tissue.

2. A threshold value was calculated from a modified image chosen from the binarization reference, using Otsu's method (graythresh function in MATLAB) to separate the pixels into the two classes. Otsu's method calculates a single intensity threshold for classifying the foreground from the background by minimizing the intra class variance or in other words maximizing the inter-class variance. In our case this threshold was for separating the lesion and intact tissue.
3. The image was then binarized using the imbinarize function with the calculated threshold value from above. The final binary image is a representation of the lesion (black pixels) and intact tissue (white pixels).

Step 4: Calculating the tissue destroyed by sub sampling:

To quantify the % tissue destroyed, a total of 48 randomized circular areas of radii=20 pixels were sampled from within the lesion. This was done to account for the tissue shrinkage that happens with fixation in formaldehyde. The fraction of destroyed tissue, which is a quantitative estimation of the completeness of the treatment was then calculated by summing the black pixels and dividing by the total area within the ROI. The average value across the 48 sub sampled sites were then calculated. The whole process from the selection of a binarization reference to the final tissue fraction calculation was then repeated thrice with different reference frames chosen and the final reported value was an average of the three measurements.

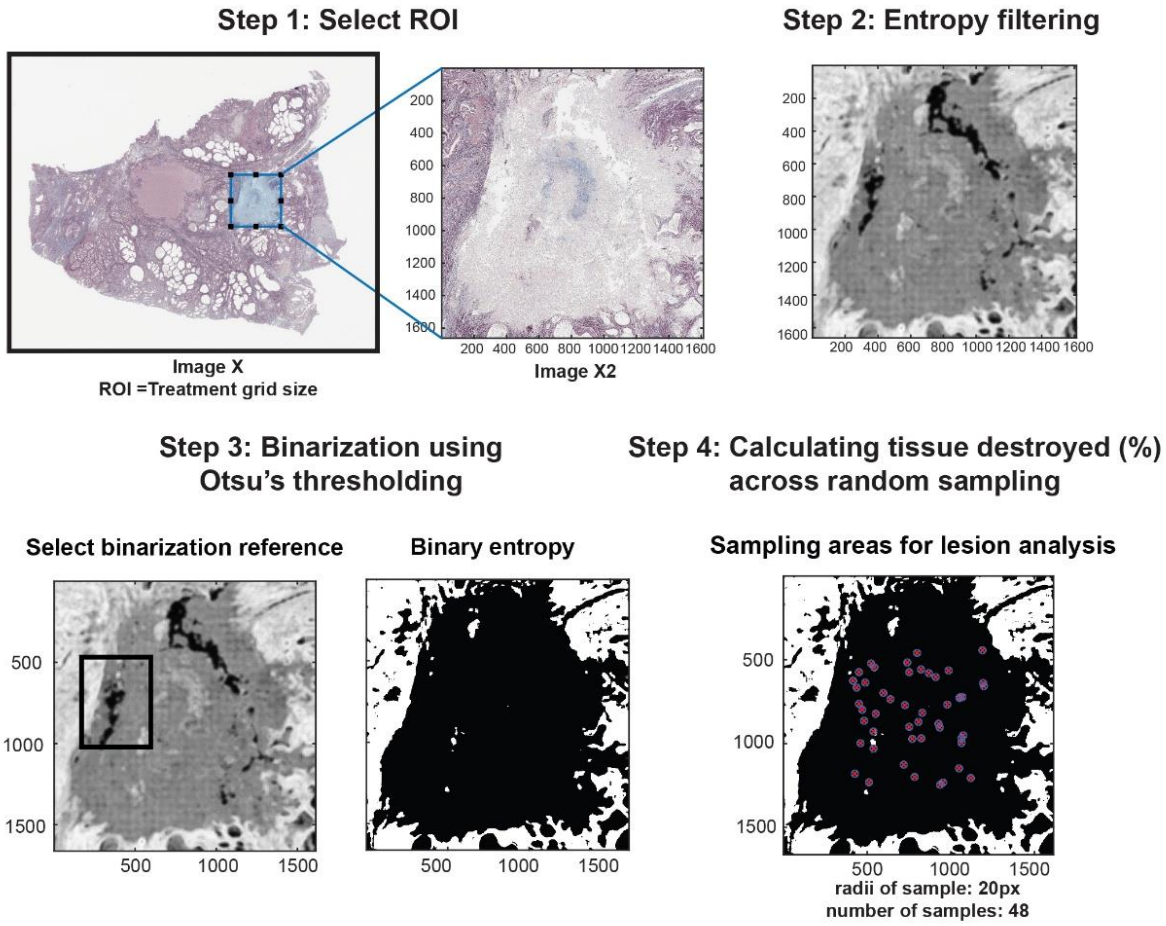

Figure A.1. Workflow depicting the outcome of the various steps in the histology slide processing by HLQE algorithm.

Methods: Performance of the HLQE model against manual segmentation

The performance of the HLQE algorithm was compared against that of manually identified histotripsy lesions (baseline) via histology. For the baseline images, an expert user manually identified the lesion areas and deleted the pixels using an open source software package Fiji[180] to create the lesion map. A total of 10 random Masson's trichrome histological samples containing lesions treated by the different modalities were chosen.

- **Preprocessing of images***:* The images were standardized using an automated tone control tool that set the exposure, clarity and vibrance of the image by analyzing the color histogram in Lightroom (Adobe Inc., San Jose, CA).
- **Histologic analysis – Manual segmentation**: All the processed samples were manually segmented in ImageJ with a freeform tool to identify the lesion area which was manually deleted from the final image. The following criteria were used to determine what is a lesion in the tissue for uniform processing***:*** **(**1) clear homogenization with cellular debris and smooth boundaries with untreated tissue; (2) glands filled with cell debris but with disrupted cuboidal/columnar epithelial lining was still considered a lesion. Post segmentation, the RGB images were converted to grayscale and binarized using Otsu's method in ImageJ to apply the comparison metrics.
- **HLQE processing:** The HLQE algorithm was applied to all the preprocessed samples across the entire image, and binary images were produced as described in the section above.
- **Metrics used for measuring performance**: A series of standard statistical metrics (accuracy, false positive rate, sensitivity, precision, Sorensen Dice coefficient and Jaccard similarity index) based on these studies[183,184] were then used to assess the performance of the HLQE against the ground truth. A 2x2 confusion/error matrix, a concept derived from

machine learning, was used here to classify the pixels of the binary image with its two classes “lesion” and “intact tissue” into the 4 possible outcomes to apply these metrics. True Positive (TP): All intact tissue pixels are correctly identified as ‘1’. False Positive (FP): Lesion pixels identified as ‘1’. True Negative (TN): All lesion pixels are correctly identified as ‘0’. False Negative (FN): Intact tissue pixels identified as ‘0’.

Results: Performance of the HLQE algorithm

We compared the results from the HLQE algorithm against the manually segmented baseline image. The results tabulated in Table A.14 show that the HLQE algorithm performs well across all the metrics measured. With a low false positive rate and a higher score across the remaining metrics, the validity of the HLQE algorithm in accurately quantifying lesions was established. Figure A.2 depicts the original histology image, followed by the superimposed lesion image identified manually segmented (baseline) and by the HLQE algorithm.

Table A.14. Different metrics summarize the performance of the HLQE against manual segmentation (baseline) across n=10 samples.

Accuracy	**False Positive Rate**	**Sensitivity**	**Precision**	**Sorensen Dice Coefficient**	**Jaccard similarity index**
0.85±0.04	0.15±0.09	0.84±0.06	0.82±0.11	0.83±0.07	0.71±0.09

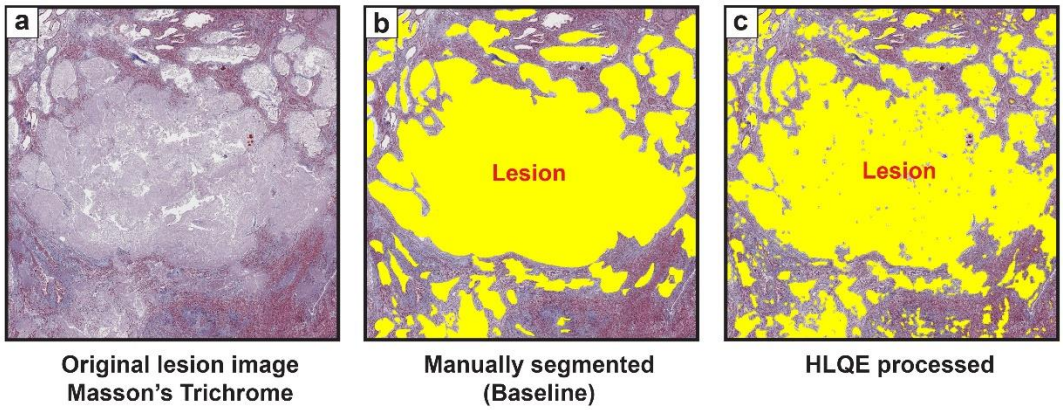

Figure A.2. Performance of the HLQE algorithm in detecting lesions. (a) Original histology image (b) Manually segmented lesion baseline image superimposed onto the histology slice. (c) Lesion detected by the HLQE and superimposed on to the histology slice.

VITA

Yashwanth Nanda Kumar received his B.E. in Biomedical Engineering from Anna University, Chennai, India, in 2012, and his M.S. in Biomedical Engineering from Arizona State University, Tempe, AZ, USA, in 2015. He is currently a Ph.D. candidate in Mechanical Engineering at the University of Washington, Seattle, WA, USA. From 2013 to 2016, he worked as a Research Assistant in the School of Biological and Health Systems Engineering, and from 2016 to 2019, he was a Research Engineer in Advanced Development at MERZ North America. His research interests include focused ultrasound for therapeutic applications, transducer design and development with image guidance, and tissue-mimicking gels.

Mr. Nanda Kumar served as the student representative on the administrative committee for IEEE UFFC from 2022 to 2023, participated in the IUS Symposia Committee in 2023, and is currently on the student board of the International Society of Therapeutic Ultrasound. He is also part of the Acoustical Society of America's Biomedical Acoustics Subcommittee.

Education:

2025 Ph.D. in Mechanical Engineering, University of Washington, Seattle, USA

2015 M.S. in Biomedical Engineering, Arizona State University, Tempe, USA

2013 B.E in Biomedical Engineering, Anna University, India

Work Experience:

2022(Summer)	Internship, Ultrasound Acoustics R&D, Philips Healthcare, Bothell, USA
2016-2019	Biomedical Engineer, Advanced R&D, MERZ North America, USA

Peer-Reviewed Publications:

1. Ambekar, P. A., Wang, Y.-N., Khokhlova, T. D., Thomas, G. P. L., Rosnitskiy, P. B., Contreras, K., Leotta, D. F., Maxwell, A. D., Bruce, M., Pierson, S., Totten, S., **Kumar, Y. N.,** Thiel, J., Chan, K., Liles, W. C., Dellinger, E. P., Adedipe, A., Monsky, W. L., & Matula, T. J. (2024). Histotripsy-Induced Bactericidal Activity Correlates to Size of Cavitation Cloud In Vitro. IEEE Transactions on Ultrasonics, Ferroelectrics, and

Frequency Control, 71(12: Breaking the Resolution Barrier in Ultrasound), 1868–1878. IEEE Transactions on Ultrasonics, Ferroelectrics, and Frequency Control. https://doi.org/10.1109/TUFFC.2024.3476438

2. **Kumar, Y.N.,** Singh, Z., Wang, YN. et al. A comparative study of histotripsy parameters for the treatment of fibrotic ex-vivo human benign prostatic hyperplasia tissue. Sci Rep 14, 20365 (2024).
3. Kanabolo, D. L., Maxwell, A. D., **Kumar, Y. N.,** & Schade, G. R. (2024). Validation of Urostomy Parastomal Herniation Incisional Prevention Strategies. Urology.
4. DL Kanabolo, AD Maxwell, **YN Kumar**, GR Schade, "Assessment of Urostomy Parastomal Herniation Forces Using Incisional Prevention Strategies with an Abdominal Fascia Model" European Urology Open Science, 2023, Vol 54, Pg 66-71.
5. **Nanda Kumar Y**, Singh Z, Wang YN, Schade G, Kreider W, Bruce M, Vlaisavljevich E, Khokhlova T, Maxwell A.D, "Development of Tough Hydrogels to Mimic fibrous Prostate Tissue" UMB June 2022.
6. Mohamed Yacin S., Chirania S., **Nandakumar Y.** (2013) Design and Development of Hypothermia Prevention Jacket for Military Purpose. In: Chakrabarti A., Prakash R. (eds) ICoRD'13. Lecture Notes in Mechanical Engineering. Springer

Conference Abstracts:

1. **Nanda Kumar, Y.,** Contreras, K., Wang, Y. N., Kreider, W., Totten, S., Schade, G. R., & Maxwell, A. D. (2024). Designing a benign prostatic hyperplasia dual-mode cavitation cloud and boiling histotripsy therapy transducer. The Journal of the Acoustical Society of America, 155(3_Supplement), A326-A326.
2. **Nanda Kumar Y,** Kim G, Kuznetsova E, Kreider W, Sapozhnikov O, Hall T, Maxwell AD, "Evaluation of Piezoelectric Transducer Vibration and Mechanical Failure Under High Power Pulsed Output, IEEE SAUS 2024
3. **Nanda Kumar Y,** Singh Z, Wang YN, Kanabolo D, Maxwell AD, Bruce M, Sekar R, Vlaisavljevich E, True L, Schade GR, "A Comparative Study of Histotripsy Parameters for the Treatment of Fibrotic Ex-vivo Human Benign Prostatic Hyperplasia Tissue" IEEE SAUS 2024

4. Kanabolo, D., Maxwell AD, **Kumar YN,** Kuznetsova E, Schade GR, “MP65-03 ASSESSMENT OF UROSTOMY PARASTOMAL HERNIATION FORCES AND PREVENTION STRATEGIES.” Journal of Urology, vol. 209, no. Supplement 4, Apr. 2023.
5. Kanabolo, D., Maxwell AD, **Kumar YN,** Schade GR. "P-003 ASSESSMENT OF UROSTOMY PARASTOMAL HERNIATION FORCES." British Journal of Surgery 110.Supplement_2 (2023): znad080-139.
6. **Nanda Kumar Y,** Singh Z, Wang YN, Maxwell AD, Bruce M, Sekar R, Vlaisavljevich E, True L, Schade GR, “Effects of Histotripsy Parameters and Dose on Ex-vivo Human Benign Prostatic Hyperplasia Tissue”– IEEE International Ultrasonics Symposium 2022
7. **Nanda Kumar Y,** Singh Z, Wang YN, Maxwell AD, Bruce M, Sekar R, Vlaisavljevich E, True L, Schade GR, “Effects of Histotripsy Parameters and Dose on Ex-vivo Human Benign Prostatic Hyperplasia Tissue” – 21st International Symposium on Therapeutic Ultrasound, 2022
8. **Nanda Kumar Y,** Singh Z, Wang YN, Schade G, Kreider W, Bruce M, Vlaisavljevich E, Khokhlova T, Maxwell A.D “Development of Tough Hydrogels to Mimic Fibrous Prostate Tissue” 35th Annual Meeting, Engineering & Urology Society, Page 34
9. Singh Z, **Nanda Kumar Y,** Wang YN, Maxwell AD, Bruce M, Sekar R, Vlaisavljevich E, True L, Schade GR, “Analysis of Ex-vivo Human BPH Tissue Treated by Histotripsy: Dose and Parameter Effects” 35th Annual Meeting, Engineering & Urology Society, Page 35
10. Singh Z, **Nanda Kumar Y,** Wang YN, Maxwell AD, Bruce M, Sekar R, Vlaisavljevich E, True L, Schade GR, “Mp04-02 analysis of ex-vivo human bph tissue treated by histotripsy: dose and parameter effects,” Journal of Urology, vol. 207, no. Supplement 5, page56, May 2022, doi: 10.1097/JU.0000000000002521.02.
11. **Nanda Kumar, Y.,** Singh, Z., Wang, Y. N., Schade, G. R., Kreider, W., Bruce, M., ... & Maxwell, A. (2021). Bubble cloud progression in fibrous tissue mimicking hydrogels at different histotripsy sonications. The Journal of the Acoustical Society of America, 150(4), A29-A29.

12. **Nanda Kumar Y,** Singh Z, Wang YN, Schade G, Kreider W, Bruce M, Vlaisavljevich E, Khokhlova T, Maxwell A.D, "Development of Tough Hydrogels to Mimic fibrous Prostate Tissue" – IEEE International Ultrasonics Symposium 2021.
13. **Nanda Kumar Y**, Singh Z, Wang YN, Schade G, Kreider W, Bruce M, Vlaisavljevich E, Khokhlova T, Maxwell A.D, "Development of Tough Hydrogels to Mimic fibrous Prostate Tissue" -20th International Symposium on Therapeutic Ultrasound, 2021.
14. Singh Z, **Nanda Kumar Y,** Wang YN, Maxwell AD, Bruce M, Sekar R, Vlaisavljevich E, True L, Schade GR," Optimizing Histotripsy Parameter Settings for the Treatment of Benign Prostatic Hyperplasia." – 20th International Symposium on Therapeutic Ultrasound, 2021-4
15. G. Schade, R. Sekar, T. Khokhlova, A. Peek, Y.-N. Wang, S. Totten, W. Kreider, **Y. Kumar,** O. Sapozhnikov, A. Maxwell, V. Khokhlova. Transrectal boiling histotripsy of the prostate: initial pre-clinical results with a prototype device. 7th International Symposium on Focused Ultrasound, Washington, 2020

Patent Application:

1. Tissue Mimicking Hydrogel, Inventors: Yashwanth Nanda Kumar and Adam D. Maxwell (Utility filed 10/12/2023 US20230321327A1, Provisional)